Out-of-equilibrium dynamics in a quantum impurity model

Kemal Bidzhiev

université PARIS-SACLAY

NNT : 2019SACLS352

Thèse de doctorat

Out-of-equilibrium dynamics in a quantum impurity model

Thèse de doctorat de l'Université Paris-Saclay
préparée à l'Université Paris-Sud

Ecole doctorale n°564 Physique en Île-de-France (ED PIF)
Spécialité de doctorat : Physique

Thèse présentée et soutenue à Saclay, le 7 octobre 2019, par

KEMAL BIDZHIEV

Composition du Jury :

Pascal Simon Professeur, Université Paris-Sud	Président
Ulrich Schollwöck Professor, University of Munich (LMU München)	Rapporteur
Doyon Benjamin Reader in Theoretical Physics and Royal Society Leverhulme Trust Senior Research Fellow, King's College, Londres	Rapporteur (absent)
Sam Carr Lecturer in Physics, University of Kent	Examinateur
Serge Florens Directeur de Recherche, Institut Néel (CNRS/ UGA)	Examinateur
Grégoire Misguich Chercheur CEA, Institut de Physique Théorique, CEA - Saclay	Directeur de thèse

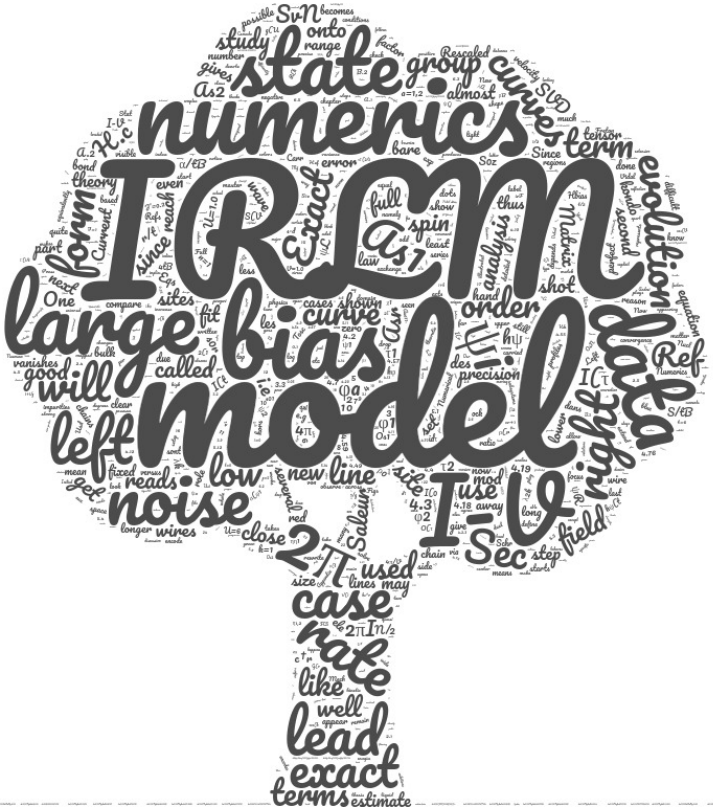
IRLM
model
numerics
state
bias
large
data
noise
left
will
low
case
rate
lead
exact
terms
like
well
used
line
order
curve
term
evolution
group
curves
study
onto
range
Exact
spin
full
thus
shot
Matrix
analysis
Ref
Python
field
Sec
use
new
side
close
called
good
reads
wires
One
sites
fit
precision
step
lines
may
almost
Since
bare
error
theory
form
Current
since
recall
Saleur
estimate

Contents

Résumé en français

En 1978, P. Wiegmann et A. Finkelshtein ont introduit le "Interacting Resonant Level Model" (IRLM) [1], comme un modèle simple pour étudier les propriétés d'une impureté magnétique de type Kondo avec des couplages anisotropes. L'IRLM peut être formulé sous forme de fermions sans spin dans deux fils semi-infinis qui sont couplés à un niveau résonant - aussi appelé point quantique ou impureté - par un petit couplage tunnel et une interaction de Coulomb Fig.1. Ce qui fait de ce problème un modèle à N-corps riche et complexe à étudier est l'interaction densité-densité entre les fermions sur le point quantique et dans les fils. Le sujet central de cette thèse sont les propriétés hors d'équilibre du modèle, en présence d'un courant de particules s'écoulant d'un fil à l'autre via le point quantique. En particulier, nous nous sommes intéressés à la caractérisation des états stationnaires qui apparaissent lorsque les deux conducteurs sont préparés avec des densités de particules différentes [voir Fig.2]. La méthode employée pour les simulations numériques est le time-dependent density matrix renormalization group (tDMRG).

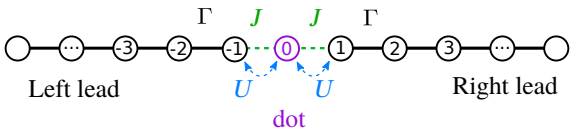

Figure 1: Schéma de l'IRLM. Deux fils sont couplés au site de l'impureté par un terme de saut J et une interaction densité-densité U.

Dans ce travail nous avons étendu les résultats obtenus lors d'études numériques précédentes concernant les propriétés de transport de l'IRLM (voir par exemple [2]), nous avons significativement augmenté la précision des résultats numériques et nous avons fourni des données dans une gamme étendue de valeurs de la tension et de la force des interactions. Nous avons obtenu des résultats tout à fait inattendus concernant la similitude entre l'IRLM et le modèle de sine-Gordon avec bord (BSG). Notre analyse montre que, bien que les deux modèles ne soient pas strictement équivalents en dehors des points dits libre et self-dual, leurs courbes courant-tension et leurs courbes de bruit de grenaille ("shot noise") sont remarquablement similaires dans une large gamme de la valeur U de l'interaction.

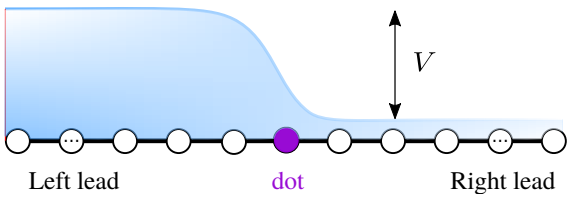

Figure 2: Schéma de l'état initial. Un différence de tension V induit une différence de densité fermionique entre les deux fils.

Pour étudier des quantités hors d'équilibre, comme le courant de particules ou le bruit, il est habituel de préparer un état initial avec un biais de densité entre les deux

fils [voir Fig. 2]. Nous avons choisi état initial $|\psi(t=0)\rangle$ comme état fondamental du Hamiltonien $H_0 = H_{\rm IRLM} + H_{\rm bias}$, où $H_{\rm bias}$ est un Hamiltonien décrivant un chimique (ou tension) non-homogène qui induit différentes densités de particules sur les fils gauche et droit. Ainsi, le potentiel chimique des fermions dans le fil gauche (resp. droit) est égal à $V/2$ (resp. $-V/2$) suffisamment loin du point quantique. Dans tout ce travail nous nous sommes concentrés sur un régime, dit d'échelle, où V et J sont suffisamment petits pour que les simulations du modèle sur réseau puissent être comparées quantitativement à la limite continue du problème (théorie des champs).

A l'instant initial le terme $H_{\rm bias}$ est mis a zéro et le système, isolé, évolue avec $H_{\rm IRLM}$. Il s'agit d'une trempe quantique ("quantum quench") et le système est hors d'équilibre pour $t > 0$. Nous sommes concentrés sur les propriétés de la région stationnaire qui se développe au centre du système. Une évolution typique du courant, en fonction du temps, est représentée sur la Fig. 3. Après un régime transitoire d'une durée $\sim 1/t_B$ le courant atteint une valeur constante, stationnaire. L'échelle d'énergie qui émerge ici, appelée échelle Kondo, se trouve être $t_B = J^{4/3} = J^{\frac{2}{1+1/2}}$ pour le point self-dual ($U = 2$), où la valeur $1/2$ devient dans le cas général un exposant $b(U)$ que l'on retrouve aussi dans le comportement à grand V du courant ($I \sim V^{-b(U)}$). Grace à l'échelle d'énergie t_B ainsi définie, on peut redimensionner le courant et la tension, de sorte que I/t_B devienne une fonction de V/t_B, et les données numériques obtenues pour une valeur de U fixée mais différentes valeurs de J tombent sur une courbe universelle (Fig. 4).

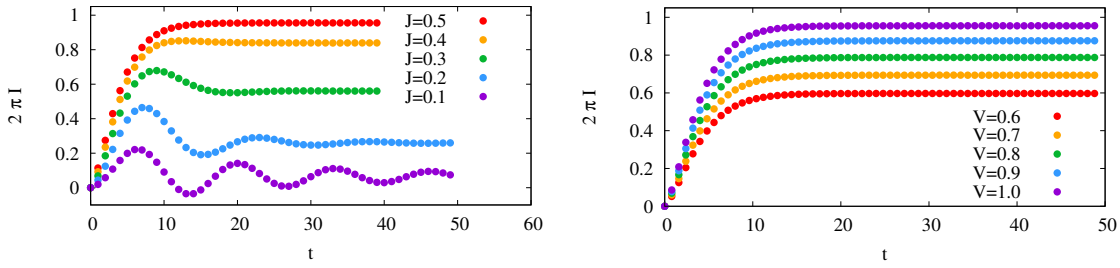

Figure 3: Courant $I(t)$ en fonction du temps et pour différentes valeurs du terme tunnel J (gauche) ou différentes valeurs de la tension V (droite). Résultats pour $U = 2$ obtenus à partir des simulations tDMRG. Dans la limite de grand temps, le courant atteint une valeur stationnaire (voir Fig. 4).

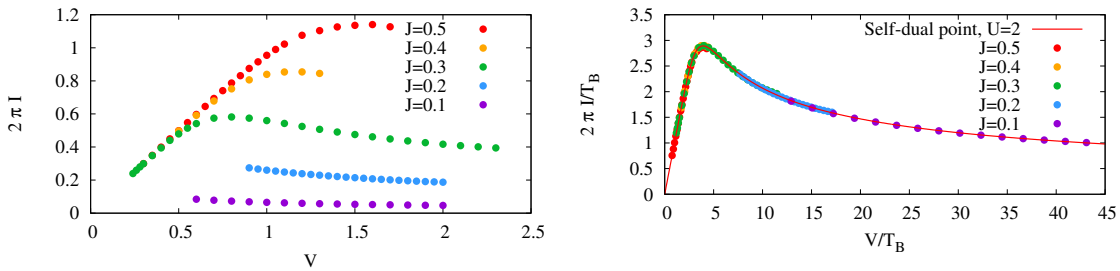

Figure 4: Courant stationnaire nu I (gauche) et dedimensionné (droite), en fonction de la tension V et au point auto-dual $U = 2$ pour différentes valeurs de l'amplitude de saut J. Chaque ensemble de données est dedimensionné par $t_B(J, U)$.

Bien que l'IRLM soit un modèle intégrable [3], il y a relativelent peu de résultats

exacts pour les propriétés hors d'équilibre en dehors du point fermions libres $U = 0$ [4, 5, 6, 7, 8] ou du point auto-dual $U = 2$ [2]. Pour ces deux valeurs particulières de U le modèle peut être résolu hors d'équilibre grace à une équivalence avec le modèle BSG, pour lesquelles les caractéristiques $I - V$ sont connues. Dans cette optique, une question qui se pose naturellement est de savoir dans quelle mesure le courant I_{BSG} pourrait aussi décrire, ne serait qu'approximativement, le courant de l'IRLM en dehors des deux cas $U = 0$ et $U = 2$.

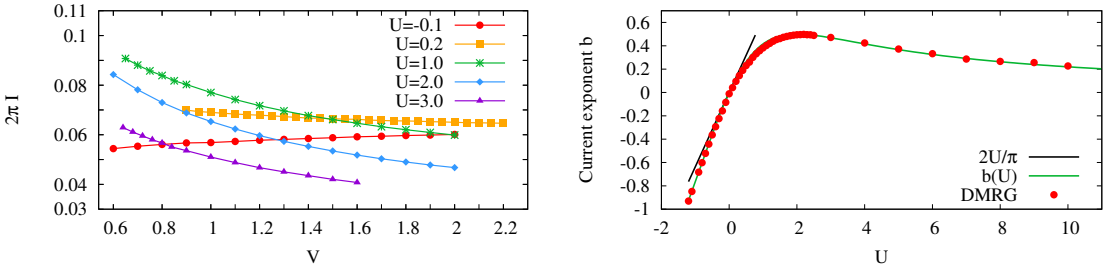

Figure 5: Panneau de gauche: courant stationnaire I en fonction de V, pour quelques valeurs de U. Le courant s'annule dans la limite $J \ll 1$ comme $I \sim V^{-b(U)}$ pour les valeurs positives de l'interaction de Coulomb U. Panneau de droite: exposant $b(U)$ en fonction de la force d'interaction U. La ligne verte continue est le résultat analytique.

Pour obtenir des courbes $I - V$ redimensionnée et les comparer aux courbes BSG, il faut déterminer $t_B(U)$. Pour ce faire, nous avons étudié le régime ultra-violet (UV), où le courant I décroît en loi de puissance $\sim V^{-b(U)}$ pour $U > 0$ [voir Fig. 5]. Grâce à l'analyse du modèle dans la limite continue l'expression exacte de $b(U)$ est connue analytiquement. Le très bon accord entre ce résultat analytique et la valeur de l'exposant extraite de nos simulations numériques souligne la précision des simulations, valide la procédure employée pour estimer le courant stationnaire, et confirme le fait que le modèle se trouve dans un régime suffisament proche du régime d'échelle.

Pour chaque valeur de U nous avons déterminé la constante de couplage $g(U)$ du modèle BSG qui assure que les deux modèles (IRLM et BSG) aient le même exposant de décroissance du courant dans le régime UV. Ensuite, nous avons comparé les courbes $I - V$ des deux modèles. Les résultats de cette analyse sont résumés dans la figure 6. Le fait remarquable et quelque peu inattendu est que pour $U \lesssim 3$ la courbe BSG $I - V$ se trouve une très bonne approximation du courant dans l'IRLM, même lorsque V/t_{B} est d'ordre 1. De façon remarquable le modèle BSG continue de très bien décrire le courant dans l'IRLM entre $U = 0$ et $U = 2$. Bien que les modèles BSG et IRLM semblent différents (Sec. 3.5.2), se pourrait-il que les deux

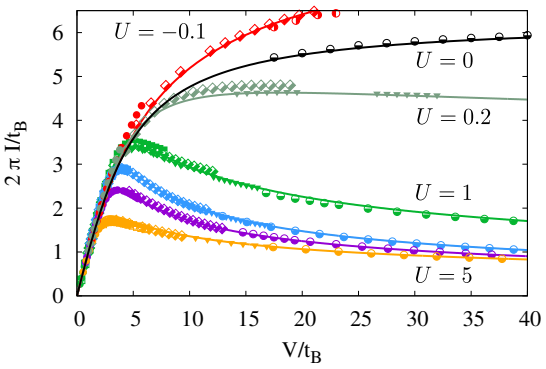

Figure 6: I/t_B actuel rééchelonné en fonction du biais rééchelonné V/t_B pour différentes valeurs de U. Les couleurs étiquettent les valeurs de U.

modèles hors d'équilibre soient en fait la même classe d'universalité ? Pour aborder ce point, nous nous sommes tournés vers une comparaison du bruit de grenaille et du comportement IR du courant des deux modèles, et nous avons pu répondre par la négative à cette question.

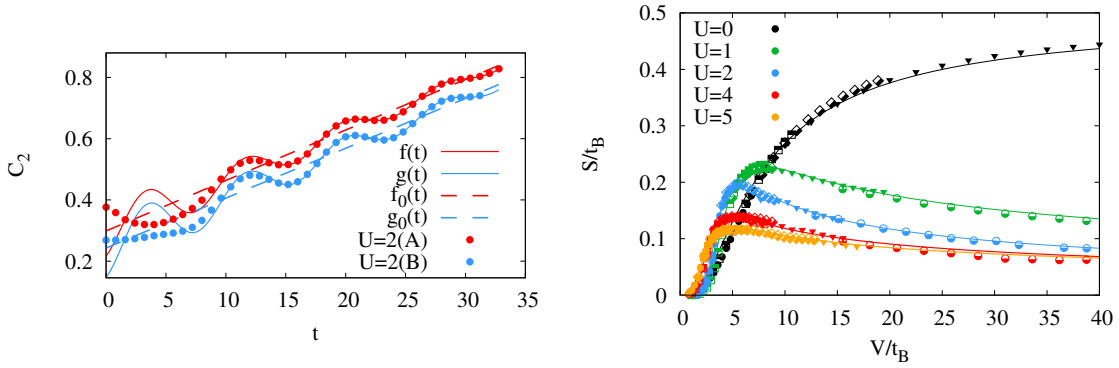

Figure 7: Gauche : évolution temporelle du cumulant $C_2(t)$ de la charge transferée, calculée en tDMRG. Les deux couleurs correspondent à deux états initiaux différents, mais avec la même tension. Bien que les deux états initiaux donnent des résultats différents pour $C_2(t)$, le taux de croissance S est essentiellement le même à temps longs. Droite : bruit redimensionné S/t_B en fonction de de la tension redimensionnée V/t_B, pour différentes valeurs de U. Les lignes complètes correspondent aux résultats exacts pour le bruit dans le modèle BSG.

Le bruit peut être défini comme la dérivée temporelle de la variance de la charge dans le fil (disons) droit. Nous avons donc calculé numériquement le deuxième cumulant C_2 de la charge du fil droit. L'évolution temporelle typique de ce cumulant est présentée dans la Fig. 7. Puisque $C_2(t)$ s'avère croître linéairement avec le temps, une quantité intéressante qui prend une valeur stationnaire à temps long est sa dérivée temporelle, dont ont peut montrer qu'elle correspond au bruit de grenaille, $S = \frac{d}{dt}C_2(t)$, quantité accessible dans certaines expériences de transport mesoscopique.

Nous avons ensuite comparé les courbes $S-V$ des modèles IRLM et BSG pour les valeurs arbitraires de l'interaction U. Les résultats numériques pour la dépendance $S-V$, (redimensionnés à l'aide de t_B), illustrés dans la Fig. 7, montrent que pour cette quantité aussi les résultats pour l'IRLM sont très proches de ceux du modèle BSG (en traits pleins).

Les caractéristiques de transport des modèles BSG et IRLM serait-elles en fait identiques ? Les courbes pour le courant stationnaire sont presque identiques pour différentes interactions U, malgré le fait que les théories ne sont censées être équivalentes qu'aux points $U = 2$ et $U = 0$. Les courbes de bruit $S - V$ pour deux théories sont également en bon accord.

Ensuite, nous avons analysé en détail des propriétés de transport des deux modèles dans le régime infra rouge (IR), c'est-à-dire dans la limite des petites tensions. Le développement à petit V du courant pour l'IRLM a été calculé par Freton et Boulat. [9]. Ils ont obtenu les premiers termes (en puissances V) du courant rétrodiffusé:

$$I_{\rm BS} = \frac{V}{2\pi} - I,$$

c.-à-d. la différence entre le I courant et la valeur $V/2\pi$ du courant en l'absence d'impureté.

Pour l'IRLM, ce courant rétrodiffusé $I_{\rm BS}$ s'annule comme V^3 à faible voltage. En revanche, le terme principal du courant rétrodiffusé dans le modèle BSG a lui un exposant qui varie continuellement avec g : $I_{\rm BS}^{\rm BSG}/T_{\rm BSG} \sim (V/T_{\rm BSG})^{-1+2/g}$. Ainsi, pour un V suffisamment bas, les données numériques de l'IRLM devraient montrer un comportement en V^3 et devraient s'écarter des résultats du modèle BSG si $U \neq 0$ et si $U \neq 2$. Au point d'auto-dualité, les coefficients des termes V^3 et V^5 s'annulent [9]. Les données de la figure 8 illustrent les comportements à faible biais de $I_{\rm BS}$ au point d'auto-dual (panneau inférieur) et à une valeur plus générique de U (panneau supérieur). Nos simulations ont ainsi confirmé que les courants du modèle BSG et de l'IRLM ont des comportements différents dans cette région IR - et que ces propriétés sont en accord avec l'analyse de théorie des champs [10]. Alors que les données basse tension à $U = 1$ suivent la prédiction perturbative de l'IRLM comme il se doit, il est frappant de constater que $I_{\rm BS}$ rejoint alors la courbe BSG pour $V/T_B \gtrsim 0.5$, bien qu'il n'y ait a aucune raison évident pour que qu'il en soit ainsi à voltage intermédiaire. L'IRLM et le BSG se comportent différemment dans l'IR, nous avons donc conclu que ces deux théories sont bien distinctes.

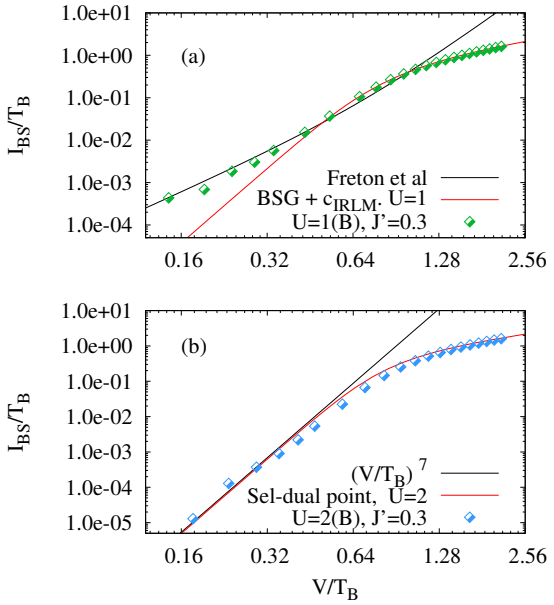

Figure 8: Panneau (a) : Courant rétrodiffusé redimensionné $I_{\rm BS}/T_{\rm B}$B $= V/(2\pi T_{\rm B}) - I/T_{\rm B}$ en fonction de $V/T_{\rm B}$ à $U = 1$. Panneau (b) : même quantité, pour $U = 2$ (point auto-dual).

Pour finir nous avons étudié l'entropie d'intrication bipartite (ou entropie de von Neumann). Cette quantité est définie par

$$S_{vN} = -\sum_i p_i \log p_i,$$

où p_i sont les valeurs propres de la matrice à densité réduite du sous-système considéré. Dans le dernier chapitre de cette thèse nous avons fourni et analysé quelques résultats numériques concernant les entropies d'intrication associées aux partitions gauche-droite du système, dans l'IRLM hors d'équilibre. Nous désignons par $S_{vN}(t, R + \frac{1}{2})$ l'entropie d'intrication de l'ensemble A des sites situés à gauche du site R, comme illustré à la Fig. 9. Fig. 10 illustre comment le profil d'intrication évolue dans le temps. La caractéristique la plus frappante est la croissance rapide de l'entropie d'intrication, qui s'avère linéaire dans le temps pour un R donné à

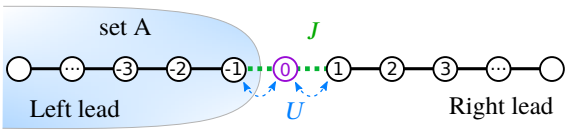

Figure 9: Ici, nous avons choisi le sous-système A pour être l'ensemble de le fil gauche.

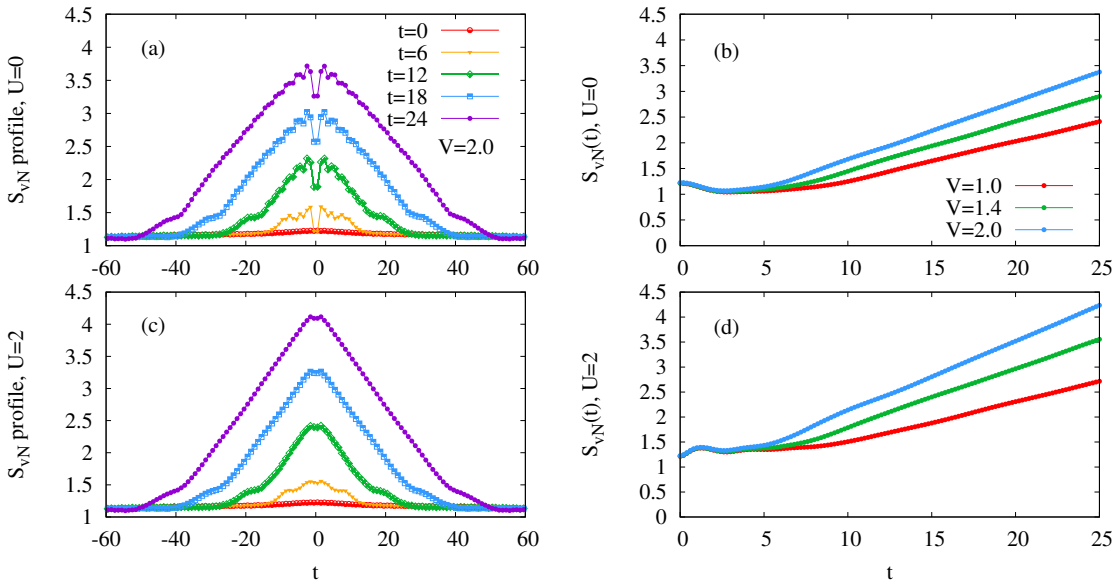

Figure 10: Panneaux (a) et (c) : évolution du profil d'entropie d'intrication $S_{vN}(r,t)$ pour $U = 0$ et pour $U = 2$. Paramètres du modèle : $J = 0.3$, $V = 2.0$, $N = 254$, comme dans la Fig. 2.3.
Panneaux (b) et (d) : évolution de l'entropie d'intrication $S_{vN}(t)$ de la moitié gauche, voir Fig. 5.1. Le taux d'intrication augmente avec la tension. Le modèle en interaction ($U = 2$) est plus intriqué que le cas libre ($U = 0$) pour les mêmes paramètres. Il nécessite donc plus de ressources de calcul pour la simulation.

l'intérieur du "cône de lumière".

Dans de telles situations, une quantité d'intérêt est le *taux* de croissance de l'entropie , défini comme

$$\alpha = \frac{d}{dt} S_{vN}(t).$$

Les simulations numériques montrent que la forme triangulaire des profils d'entropie est une caractéristique robuste, au moins suffisamment éloignée du point quantique. Plus près du point, le profil n'est cependant pas triangulaire, ce qui a été analysé dans Sec. 5.2.

Nous avons extrait des simulations le taux stationnaire de croissance de l'entropie au centre du système, α. Comme pour le courant, nous avons considéré le taux redimensionné α/t_B comme une fonction de la tension redimensionnée V/t_B. Les résultats, tracés dans les Figs. 11, montrent que les données obtenues pour une valeur donnée U mais pour différentes valeurs de J tombent assez bien sur une seule courbe maîtresse. Le résultat exact pour α au point fermions libres (dérivé en Sec. 5.3) converge lentement vers une constante finie, $\alpha/t_B \to 2$, à grand voltage. Une information importante que nous pouvons tirer de la figure 11 est

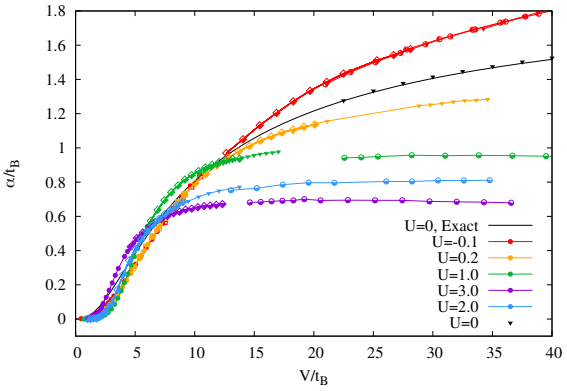

Figure 11: Taux de croissance de d'entropie redimensionné, α/t_B, en fonction de la tension redimensionnée V/t_B, pour plusieurs valeurs de U.

que, en présence d'interactions, α/t_B sature également à une valeur finie pour les grandes valeurs de V/t_B. Cette valeur limite semble être inférieure à 2 lorsque $U > 0$. Pour $U > 0$, alors que le courant décroit vers zéro à grand V/t_B (Fig. 6), le taux d'entropie, lui, reste fini. Cette observation est peu intuitive puisqu'une très faible quantité de charge est transférée par unité de temps d'un fil à l'autre, alors que leur entropie d'intrication continue à croître à un rythme fini. Dans la limite où V/t_B devient infini, l'intrication est générée par l'interaction densité-densité U, sans qu'aucun transfert réel de particules n'ai lieu. Il serait bien sur très intéressant de pouvoir parvenir à meilleur compréhension de l'entropie d'intrication dans cette limite.

Chapter 1

Introduction

The fields of in- and out-of-equilibrium quantum many-body systems are major topics in Physics, and in condensed-matter Physics in particular. Condensed matter has often been at the core of important development in theoretical Physics, like the theory of phase transitions or the renormalization group to name some of the most famous examples. And this continues to be the case. Indeed, relatively recent achievements revealed new deep connections between condensed matter theory and other chapters of physics, for instance, spin chains and supersymmetric gauge theories [11], topological insulators and black holes [12], a holographical description of space-time and tensor networks [13, 14]. These progresses were allowed by the development diverse powerful theoretical techniques, for instance, Bethe ansatz [15, 16], renormalization group [17, 18], bosonization [19, 20, 21], matrix product states and the density matrix renormalization group [22, 23, 24, 25, 26], conformal field theory [27] etc.

Although the equilibrium characteristics of many models are known, this is in general not enough to describe their non-equilibrium behaviors. The latter often remain less explored and much less understood than the equilibrium cases. Much fewer exact results are available [28, 29]. For instance, the question of when and how an isolated interacting quantum system can reach an equilibrium state remains open. To be more specific and closer to the topic of this thesis, we could mention another open problem: under which conditions a model that is integrable in equilibrium can also be solved out-of-equilibrium.

The field of out-of-equilibrium quantum many-body systems has developed rapidly in the last decade [28], from studies about transport properties, entanglement entropy [30], dissipation or the effect of disorder, the issues raised are very diverse, and often fundamental. As an example of a key topic, one can mention quench dynamics and the equilibration after quenches [31, 32, 33]: one prepares an initial state ρ_0, which is the ground state of some Hamiltonian $H_0 = H(s_0)$, and then one abruptly changes one or several parameters of the Hamiltonian $H = H(s)$. The parameters, generally speaking, could be local or global. For spin models, one may alter, for instance, some anisotropy parameter or an external magnetic field. The object of interest is the many-body unitary time evolution under the Hamiltonian $H(s)$ and, in particular, expectation values $\langle I(t)\rangle = \mathrm{Tr}\left(e^{-iHt}\rho_0 e^{iHt} I\right)$.

The equilibrium properties of one-dimensional problems are well understood theoretically for a vast amount of interacting models [34], from lattice spin chains to quantum fields in a continuum. They thus represent an interesting playground to

develop our understanding of out-of-equilibrium phenomena. Within this context, one may consider inhomogeneous quenches, where the initial state is constructed by gluing together two regions – the left and right halves of the system – in different macroscopic states. For instance, a system with an initial particle bias or magnetization bias, as a "domain wall" problem, is a natural quench setup. The dynamic will lead to a spreading of magnetized domains in spin systems or to the propagation of charges in conducting materials. Several types of behavior can take place and the propagation could be, for instance, ballistic or diffusive (see, e.g., Ref.[35]). A new approach, so-called generalized hydrodynamics, was proposed recently in [36, 37] to tackle ballistic transport problems in integrable one-dimensional systems following inhomogeneous quenches.

In the realm of interacting quantum systems, quantum impurities models occupy an important role. In such models an impurity or "dot" is coupled to an environment by a (often weak) link.

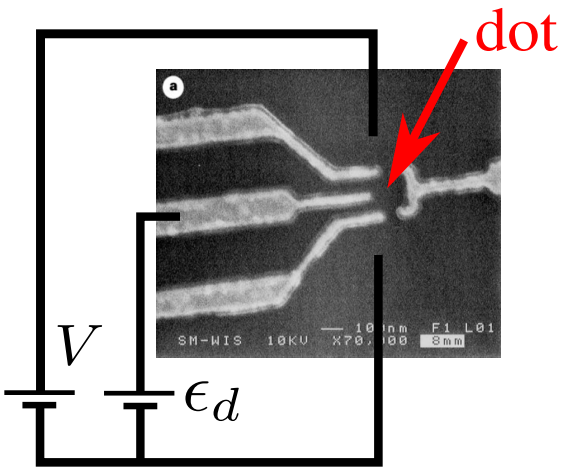

Figure 1.1: Nanodevice of a quantum dot. Scanning electron microscope image showing top view of sample from Ref [38]. The right, upper left and lower left electrodes control source-drain voltage V. The central left electrode is used to control voltage ϵ_0 of the quantum dot.

Here the dot represents a small subsystem with a discrete energy spectrum. The energy differences between the levels of the dot are much larger compared to that of the environment. In this sense the dot is "small". Despite the apparent simplicity of these models, they can capture several important experimental phenomena: from magnetic impurities that lead to the Kondo effect in metals [39], to transport in nanostructures such as point contacts or quantum dots [38]. In the Kondo effect, the quantum impurities are magnetic atoms (like cobalt), doped into a non-magnetic metallic environment (like copper and gold). These magnetic impurities have a strong effect on the resistivity of the material at low temperatures: the resistance increases when lowering the temperature (contrary to what happens in clean metals or in presence of nonmagnetic impurities).

Jun Kondo provided the beginning of an explanation for this phenomena in 1964, using his s-d exchange model. His third order perturbative calculations revealed a logarithmic increase of the resistivity when the temperature is lowered. The scale at which this phenomenon occurs is called the Kondo temperature [39, 40]. Despite the success of the perturbation theory, it predicted an unphysical infinite resistivity at zero temperature. This raised new challenges for non-perturbative techniques to refine this result, and lead a few years later to the development of powerful scaling ideas [41, 42, 43].

The rapid development in nanotechnologies at the end of the '90 allowed to realize the Kondo effect in fabricated quantum devices (see the schematics in Fig. 1.1). The impurity is a nanostructured semiconductor box that can hold a some number of electrons [40]. A voltage ϵ_0 applied to the central gate electrode of the device tunes

the number of trapped electrons on the dot. In cases where an odd number of electrons are confined in the dot, the total angular momentum s is necessarily non-zero (with a minimum value of $s = 1/2$) and the nanodevice somewhat mimics the cobalt-in-copper system. For an even number of electrons, the Kondo effect is however absent.[1]

In 1975 the Kondo problem was numerically solved by K. Wilson [17]. He explained a finite experimental resistivity at zero temperature by constructing an iterative renormalization solution. In 1982 he received the Nobel prize for his work, and his method is now called the "Numerical Renormalization Group" (NRG). With this, the low temperature resistivity divergence and the Kondo problem were tamed. Nevertheless, the lack of exact analytical solution gave rise to development of new methods, since perturbative techniques were not able to explain Wilson's results. To refine the result of Jun Kondo, physicists proposed different models and found similar and related mechanisms in other problems. For instance, Anderson and Yuval established similarities between the "X-ray edge problem" [44] and the Kondo model [41, 42, 43].[2] As another important example, we mention the boundary-Sine Gordon model(BSG) [46], where the non-trivial physics is carried by solitons, while the boundary interactions mimic an impurity. The BSG model is solvable both in and out-ofequilibrium [47, 48] and this will play an important role in the present study.

In the 1978 P. Wiegmann and A. Finkelshtein introduced the "Interacting Resonant Level Model" (IRLM) [1], as a simpler model to study analytically the properties of the Kondo s-d exchange model. In the cases which we are interested in, the IRLM can be formulated as spinless fermions in two semi-infinite leads that are coupled to a resonant level – called quantum dot or impurity – via weak tunneling and Coulomb interaction (more details in Chap. 2).[3] The conducting electrons of the leads scatter on the impurity, and what makes the problem rich and difficult to solve is the local density-density interaction between fermions on the dot and in the lead. The out-of-equilibrium properties of the model is the central subject of this thesis. In particular, we will be interested in characterizing the current-carrying steady states which emerge when the two leads have different particle densities.

Despite the fact that the IRLM is integrable by the Bethe ansatz technique [55] for arbitrary values of the Coulomb interaction, its out-of-equilibrium characteristics are not known exactly, apart for two special points. These are the *free* fermionic and *self-dual* points, where some charge transport properties have been obtained exactly. These quantities include the steady current [56, 2], the current shot noise [4, 57] and the full-counting statistics [58]. The solution [2] is based on a mapping of IRLM onto the BSG model via bosonisation. This has lead in particular to one counterintuitive

[1] The Kondo effect produces a different behavior for real metals, like copper or gold, and for quantum dot devices. In the first case of the bulk metals, the *resistance* increases at low temperatures, but for quantum dots the situation is opposite and the *conductance* grows (i.e. the resistance decreases) when the temperature decreases. The conductance reaches its ultimate value $2e^2/h$ and electrons pass through the dot as if it would be transparent.

[2] If an X-ray "hits" a core electron in a metal and excites it to some unoccupied band, the resulting hole somewhat acts as an impurity for the conducting electrons[45].

[3] One may also find some variations of this model in the literature, like, for instance, the so-called multichannel IRLM, where more than one leads are attached to the impurity site [49, 50] and a version where the impurity is coupled not to free fermion leads but to Luttinger liquids [51, 52, 53, 54].

result: the current vanishes like a power law in the large voltage regime, which means that the differential conductance is negative in this domain. Also, among the exact out-equilibrium results for the IRLM, we want to point the perturbative approach (infra-red, or low-voltage regime) of Ref. [9], where and analysis of ≈ 1500 diagrams was carried out, as well as the ultra-violet (high-voltage regime) expansion [59], which captures the negative differential conductance for low values of the interaction.

As it was mentioned above, an analytical solution of the IRLM out-of-equilibrium for arbitrary values of interaction is not accessible. At this point, numerical techniques come into play, like the numerical renormalization group [50, 60, 61] and the time-dependent density matrix renormalization group [62, 63, 64, 2]. One important advance was the agreement between analytical results and numerics at the self-dual point [2]. It was shown in particular that t-DMRG simulations can probe the lattice formulation of the IRLM in a regime – called *scaling* regime – where the model behaves as its continuum counter part. In this regime, transport properties like the steady current become, after some suitable rescaling, a function of a single combination of the voltage bias and tunneling amplitude to the dot.[4]

In the present work, our objective was first to refine and extend some of the previous numerical studies concerning the transport properties of the IRLM in the scaling regime, increasing the precision of the numerical results, and providing data in some extended range of voltage bias and interacting strengths. In the Chapter 3 we provide a detailed (tDMRG) numerical study of the particle current. We obtain surprising results concerning the similarity between the IRLM and the BSG model. Our analysis shows that, although the two models are not equivalent away from the free and self-dual points, their current-voltage curves are strikingly similar in a large range of interaction strengths. In the Chapter 4 we present new data concerning the shot noise and the *backscattered* current of the IRLM. Quite remarkably we observe that the shot-noise curves for the IRLM and BSG models are also very similar, at least if the interaction strength is not too large. There we confirm numerically some analytical results concerning the effective charge of the quasiparticles in the IRLM at low voltage. This analysis shows that, despite the quantitative similarity between the current and shot noise curves of the IRLM and BSG model, they are in fact not in the same "universality class". Then, in the Chapter 5 we study the entanglement entropy between the two leads, and the rate at which it grows with time. This linear entropy growth is the major difficulty for matrix-product state simulations, since it requires so increase the matrix dimensions exponentially with time. There have been several studies on the entanglement properties of quantum impurity models, but most of these works focused on the ground state [65]. On the other hand our work focuses on the entropy growth in current-carrying states, a quantity for which analytical results are very scarce away from free-fermion situation.

[4] As we will explain, this rescaling involves an energy scale which is equivalent to the Kondo temperature mentioned above.

Chapter 2

The resonant level model and time evolution

2.1 The interacting resonant level model

The s-d exchange model of Kondo could be simplified and solved at specific value of the interaction parameter J_z [66], which is called "Toulouse" limit. The solution is obtained by mapping s-d model onto free fermions model, where electrons simply scatter on the impurity. As a natural generalization of that model, P. Wigman and A. Finkel'shtein introduced the *Interacting resonant level model* (IRLM), where interactions come into play.

The model represents two semi-infinite left and right wires, where spinless fermions propagate throughout lattice sites with amplitude Γ Eq.(2.2)-(2.3). The bulk wires are attached to the impurity through the weak tunneling $J < \Gamma$ and through the interaction on a contact link with strength U [see Fig. 2.1]. Amount of fermions on the impurity, or, simply, particle density is controlled by ε Eq. (2.8) and the Hamiltonian of the IRLM reads:

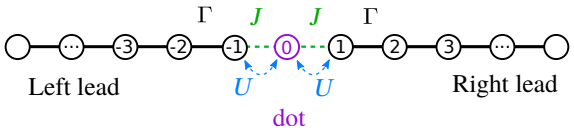

Figure 2.1: Schematics of the IRLM. Two leads are coupled to the dot through weak tunneling J and density-density interaction U.

$$H_{\text{IRLM}} = H_L + H_R + H_d \tag{2.1}$$

$$H_L = -\Gamma \sum_{r=-N/2}^{-2} \left(c_r^\dagger c_{r+1} + \text{H.c}\right) \tag{2.2}$$

$$H_R = -\Gamma \sum_{r=1}^{N/2-1} \left(c_r^\dagger c_{r+1} + \text{H.c}\right) \tag{2.3}$$

$$\begin{aligned} H_d &= -J\left(c_{-1}^\dagger c_0 + c_1^\dagger c_0 + \text{H.c}\right) + \varepsilon c_0^\dagger c_0 + \\ &+ U \sum_{r=\pm 1} \left(c_r^\dagger c_r - \frac{1}{2}\right)\left(c_0^\dagger c_0 - \frac{1}{2}\right). \end{aligned} \tag{2.4}$$

The particle model could be reformulated in terms of spin-1/2 variables, which we actually use in our simulations:

$$H^{(2)}_{\text{IRLM}} = H_L + H_R + H_d \tag{2.5}$$

$$H_L = -\Gamma \sum_{r=-N/2}^{-2} \left(S^+_r S^-_{r+1} + \text{H.c}\right) \tag{2.6}$$

$$H_R = -\Gamma \sum_{r=1}^{N/2-1} \left(S^+_r S^-_{r+1} + \text{H.c}\right) \tag{2.7}$$

$$H_d = -JS^-_0 \left(S^+_{-1} + S^+_1\right) + \text{H.c} + \varepsilon S^z + \\ + U\left(S^z_1 S^z_0 + S^z_{-1} S^z_0\right). \tag{2.8}$$

The U-term is similar to Δ anisotropy in XXZ spin chain, but acts in the vicinity of the dot. The Hamiltonian Eq. (2.5) and physical observables in the present work have only the nearest neighbor terms, and, therefore, Jordan-Wigner strings will not appear in the following context [see Chap. 3, 4 or 5]. In this work we will only consider the case $\varepsilon = 0$, which is symmetric under the simultaneous exchange of the left and right leads and a particle-hole transformation. For this reason, the mean density on the dot itself is fixed to be "resonant" $\langle c^\dagger_r c_r\rangle = \frac{1}{2}$, i.e. ε gate potential on the dot is set to zero.

2.2 Initial state and quench protocols

As it was mentioned in the introduction, the main objects of this study are the out-of-equilibrium transport properties of the model, and the particle current, in particular. To study out-of-equilibrium quantities, like the particle current or its shot noise or other types of energy flow in the system, one can prepare a state with some initial bias in particle density or in temperature [see Fig. 2.2].

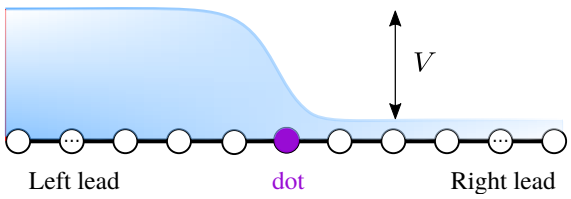

Figure 2.2: Schematics of the initial state. A particle bias, or, equivalently, a voltage, is indicated as V.

We choose the initial state $|\psi(t=0)\rangle$ to be the ground state of $H_0 = H_{\text{IRLM}} + H_{\text{bias}}$, where H_{bias} is an inhomogeneous chemical potential (or voltage) that induces different particles densities in the left and on the right leads

$$H_{\text{bias}} = \frac{V}{2} \sum_{r=-N/2}^{N/2} \tanh(r/w) c^\dagger_r c_r. \tag{2.9}$$

In the left (right) lead the chemical potential is thus equal to $V/2$ ($-V/2$) sufficiently far from the dot. The bias induces different initial densities $\rho = \langle c^\dagger_r c_r\rangle = \frac{1}{2} \pm m_0$ in the bulk of the leads at $t = 0$ (red horizontal line in Fig. 2.3). For an infinite system, $N \to \infty$, the Fermi momenta k^+_F (k^-_F) in the left (right) lead is set by $2\Gamma\cos(k^\pm_F) = \pm V/2$, and these are related to the density difference m_0 through $k^\pm_F = \pi(\pm m_0 + 1/2)$.

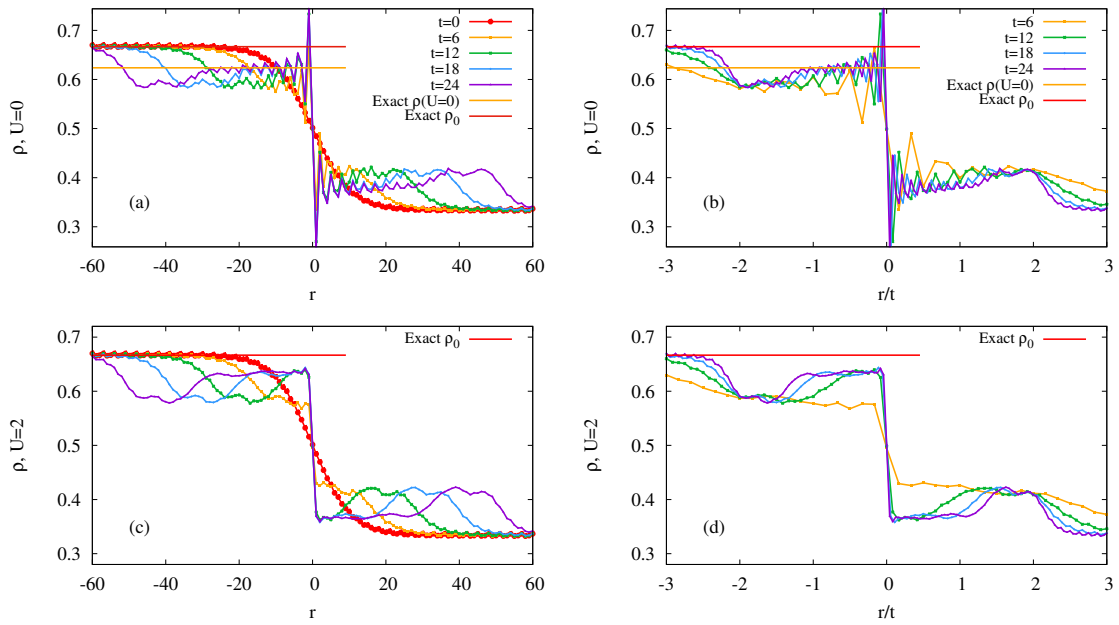

Figure 2.3: Particle density $\rho(r,t)$ at times $t = 0, 6, 12, 18, 24$. Panels (a): $U = 0$, (b): $U = 2$, (c): $U = 0$ in rescaled coordinates r/t, (d): $U = 2$ in rescaled coordinates r/t. The initial density ρ_0 in the bulk of the left lead is indicated by a (red) horizontal line. The orange horizontal line marks the exact bulk stationary magnetization ρ for $U = 0$ [see Eq. 2.10]. Note that some Friedel-like oscillations develop at long times in the vicinity of the dot, and these are much stronger in the non-interacting case. Parameters of the model: $J = 0.3$, $V = 2.0$, $N = 257$.

As done in previous studies [2], the voltage drop in Eq. (2.9) is spatially smeared over $\sim w$ sites in the vicinity of the dot. This has the effect of producing an initial state with smoother density in the vicinity of $r = 0$ and turns out to accelerate the convergence to a steady state. We typically use $w = 10$.

In the present work we use two different quench protocols, dubbed (A) and (B). The two protocols differ by their initial states. In the protocol (A) the initial state is prepared as the ground state of $H_{\rm bias} + H_{\rm IRLM}(U_0, J_0)$ with $U_0 = 0$ (free fermions) and with an homogeneous hopping amplitude $J_0 = \Gamma = 1$ in the whole chain. The interactions are switched on for $t > 0$. The system $H_{\rm IRLM}(U_0, J_0)$ is uniform in this setup, and initial density smoothly changes from the left wire to the right without spatial Friedel-like oscillations in the vicinity of the dot. We mostly use protocol(A) for studying region of relatively small interaction strength $U < 2$.

On the other hand, in the protocol (B) the initial state is the ground state of $H_{\rm bias} + H_{\rm IRLM}(U, J)$. In other words, U and J are not changed at the moment of the quench. For a simple energy reason [see Appendix sec. C], this initial state should be preferred at large U. It also produces a lower amount of entanglement entropy between the wires and the dot Fig. C.2, which means lower bond dimension M in MPS representation and thus allows for longer simulations compared to protocol(A). We use the protocol(B) for large values of the interaction strength $U > 2$ unless specified otherwise.

In the Fig. 2.4 we present an initial particle density $\rho(r) = \langle c_r^\dagger c_r \rangle$ profile as a function of position r for different values of the initial parameters.

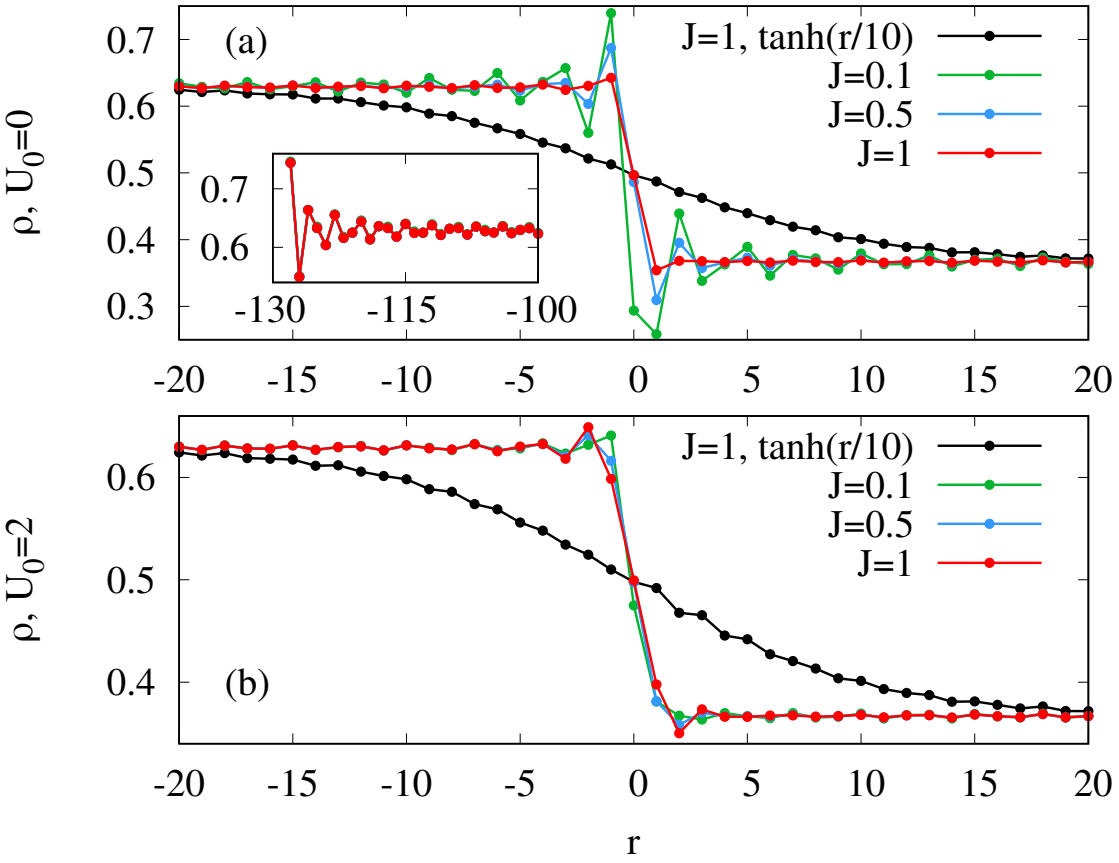

Figure 2.4: Initial density profile $\rho(r)$ as a function of position r for different values of the initial interaction value U_0 with fixed voltage $V = 1.6$. Panel (a): $\rho(U_0 = 0)$. Color line encodes the value of the hopping amplitude J $(0.1, 0.5, 1)$. Friedel-like oscillations develop in the vicinity of the dot and the amplitude of these oscillations increases with decreasing J. In the limit of $J = 0$ the wires are decoupled from the dot and the oscillations are the same as near the edges of the system [see inset (a)]. Panel (b): the same as panel (a) for $U_0 = 2$. Including interactions in the initial state suppresses the Friedel oscillations. Parameters of the model: $V = 1.6$, $N = 257$.

2.3 Particle density

The particle density is defined by $\rho(r,t) = \langle\psi(t)|c_r^\dagger c_r|\psi(t)\rangle$. We can equivalently use a spin language, the density is then simply related to the z component of the magnetization: $S^z(r,t) = \rho(r,t) - \frac{1}{2}$. A typical evolution of the density profile is shown in Fig. 2.3. It shows how the initial profile at $t = 0$ gives rise to two propagating fronts (one to the left and one to the right), forming a "light cone". We also see how some steady region forms in the center. In the rescaled "ballistic" coordinates $\xi = r/t$, the fronts propagate with velocity $v \approx v_F = 2$, where v_F is Fermi velocity [see Fig. 2.3 (c), (d)].

When the time is large enough, two regions with quasi homogeneous densities develop on both sides of the dot. The densities in the steady regions of the lead can be written as $\rho = \frac{1}{2} \pm m$, and the density difference m between both sides of the dot

can be computed exactly in the free fermion case $U = 0$. The result reads:

$$m = \int_{k_F^-}^{k_F^+} \frac{dk}{2\pi} \mathcal{R}(\epsilon(k)) \tag{2.10}$$

where $\mathcal{R}(\epsilon)$ is the reflexion coefficient for an incident particle with energy ϵ (more details and derivation of $\mathcal{R}(\epsilon)$ in Sec. 3.2).

This exact value ρ is in agreement with the magnetization that is measured numerically in the stationary region for $U = 0$ (bottom panel of Fig. 2.3), but slightly different from that observed in the interacting case (top panel of Fig. 2.3), as expected.

2.3.1 Density drop across the dot

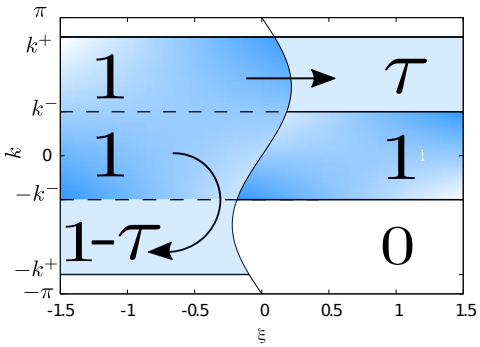

Figure 2.5: Schematics to illustrate the hydrodynamical (or semiclassical) approximation Eqs. (2.11, 2.12). Blue region represents particle density with momentum k at position and time $\xi = r/t$.

We make the approximation that each fermions is a point-like particle which propagate ballistically in leads, at some group velocity $v(k)$. In this semi-classical approximation (called hydrodynamical approximation in Ref. [67]), each particle has a well defined position *and* momentum. For a rigorous discussion and justification of this approximation, we refer for instance to Ref. [68] and references therein. In this approximation, each lead becomes homogeneous in the steady regime and the system is described by some occupation numbers $n(k)^{R/L}$ in both leads. Taking into account the initial momentum distributions and the scattering on the dot, we obtain:

$$n(k)^L = \begin{cases} 0 & \text{if } k_F^+ < k \\ 1 & \text{if } -k_F^- < k < k_F^+ \\ \mathcal{R}(k) & \text{if } -k_F^+ < k < -k_F^- \\ 0 & \text{if } k < -k_F^+ \end{cases} \tag{2.11}$$

$$n(k)^R = \begin{cases} 0 & \text{if } k_F^+ < k \\ \mathcal{T}(k) & \text{if } k_F^- < k < k_F^+ \\ 1 & \text{if } -k_F^- < k < k_F^- \\ 0 & \text{if } k < -k_F^- \end{cases} \tag{2.12}$$

The total density in each lead is then obtained by integrating the distributions above. Using the fact that $k_F^+ + k_F^- = \pi$ and $\mathcal{R}(k) + \mathcal{T}(k) = 1$ we find:

$$\rho^L = \frac{1}{2} + \int_{k_F^-}^{k_F^+} \frac{dk}{2\pi} \mathcal{R}(\epsilon(k)) \tag{2.13}$$

$$\rho^R = \frac{1}{2} - \int_{k_F^-}^{k_F^+} \frac{dk}{2\pi} \mathcal{R}(\epsilon(k)). \tag{2.14}$$

These densities describe the parts of the leads that are sufficiently far from the dot ($|r| \gg 1$), and at times that are sufficiently long ($t \gg r$), so that the growing quasi-steady region has reached r (and $-r$). On a finite system we should additionally require $2Jt \lesssim N/2$ [$2J$ being the fastest group velocity], otherwise some particles will have reach the system boundary [see [69] for a semiclassical treatment of these reflections at the system boundaries].

We thus expect some density drop

$$\rho^L - \rho^R = 2 \int_{k_F^-}^{k_F^+} \frac{dk}{2\pi} \mathcal{R}(\epsilon(k)) \tag{2.15}$$

across the dot. As typical drop is presented in Fig. 2.3 (a). The density for free fermions on the left wire is $\rho_L \approx 0.62$ and on the right wire is $\rho_R \approx 0.37$, which agrees with our result $\rho^L - \rho^R = 2m \approx 0.25$.

Chapter 3

Current

We focus on the out-of-equilibrium steady state which emerges from quench protocol discussed in the previous chapter. The system as a whole is not in a steady state, but we will focus on the properties of the steady region which grows in the center of the system, and where local observables asymptotically become independent of time. In this chapter we will, in particular, focus on the particle current, which quantifies the rate at which the fermions flow from the left lead to the right lead.

3.1 Particle current profile

On a given bond the expectation value of the current operator is

$$I(r,t) = 2J_r \mathrm{Im}\langle\psi(t)|c_r^\dagger c_{r+1}|\psi(t)\rangle, \tag{3.1}$$

where we used $\langle c_n^\dagger c_m\rangle - \langle c_m^\dagger c_n\rangle = 2\mathrm{Im}\langle c_m^\dagger c_n\rangle$ and J_r is the hopping amplitude between the sites located at r and $r+1$. We thus have $J_r = J$ for $r = -1$ and $r = 0$ (hopping to the dot), and $J_r = \Gamma = 1$ otherwise (in the leads). This definition insures the proper charge conservation (or continuity) equation:

$$\frac{d}{dt}\langle\psi(t)|c_r^\dagger c_r|\psi(t)\rangle = I(r-1,t) - I(r,t). \tag{3.2}$$

When no position r is given, $I(t)$ refers to the averaged current on both sites of the dot: $I(t) = \frac{1}{2}\left(I(-1,t) + I(0,t)\right)$.[1]

A typical evolution of the current profile is shown in the panel of Fig. 3.1. As for the density, two fronts propagate with $v \approx \pm 2$ and form a "light-cone". In the center of the system one observes the emergence of a symmetrically growing spatial region where the current asymptotically tends to some constant in space and time. This is where some *steady* value of the current can be defined and will be studied in further. Interestingly, the current in the (left-moving and right-moving) front regions reaches values that are significantly larger than in the steady regions.

3.2 Steady current for non-interacting fermions

[1] In most figures we plot $2\pi I(t)$ to match with previous results in the literature [2]. In this convention the Plank constant is $h = 1$.

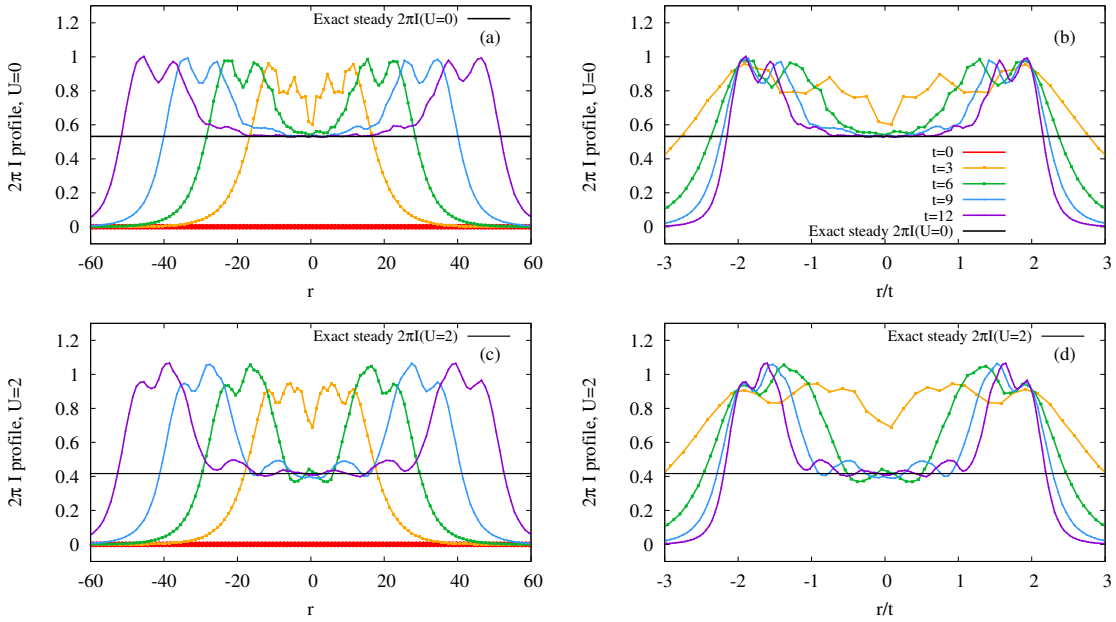

Figure 3.1: Current profile $I(r,t)$ at times $t = 0, 6, 12, 18, 24$. Panels (a) and (b): Current in the non-interacting model ($U = 0$) in linear (a) and rescaled (b) coordinates r/t; (c) and (d): the same for self-dual model ($U = 2$) . The exact steady current I for $U = 0$ is indicated by a black horizontal line in panels (a) and (b). The exact current for self-dual point is presented in panels (b) and (d) (see text), derived in Ref. [2]. Parameters of the model: $J = 0.3$, $V = 2.0$, $N = 257$.

In this section we consider the resonant level model, which is the *noninteracting* limit of the IRLM, with $U = 0$. We will derive the value of the steady current $I(J,V)$ as a function of the hopping amplitude and voltage.

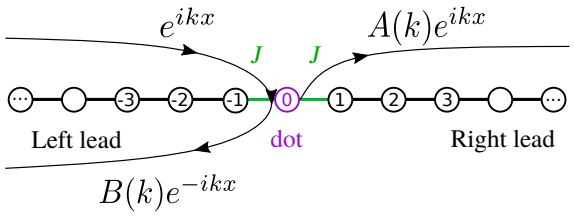

Figure 3.2: Schematic of the stationary solution of Schrödinger Eq. (3.4) of the RLM.

Ballistic particle propagation is a remarkable feature of a free fermionic system. Since the particles do not interact with each other ($U = 0$), it is enough to consider a single particle that is scattered by the dot. The result of a scattering between particle and the quantum dot is a reflection probability, a transmission probability, and a phase shift for the transmitted mode [see Fig. 3.2].

Many out-of-equilibrium characteristics, like the steady particle current, the rate of entanglement entropy growth as well as other observables (e.g. Eq.(2.10)), are fully determined by the probability $\mathcal{T}(\epsilon_k)$ for a given incoming mode k from the left lead to be transmitted (reflected) to the right one [4, 8]:

$$\mathcal{T}(\epsilon_k) = |A(k)|^2 = \frac{1 - \epsilon_k^2/4}{1 + \epsilon_k^2(1 - 2J^2)/(4J^4)}. \tag{3.3}$$

The transmission [or reflection] coefficient $\mathcal{T}(k)$ [or $\mathcal{R}(k) = 1 - \mathcal{T}(k)$] is a function of only two parameters [see Fig. 3.4], - the hopping amplitude J and the single-particle

energy $\epsilon_k = -2\cos(k)$. The formula above contains a crossover energy $t_B \sim J^2$ which separates low and large scales [see Sec. 3.2.2 and 3.3.3]. The Eq. (3.3) will be derived in the next section.

3.2.1 Solution of the single-particle Schrödinger equation

To derive the result of Eq. (3.3), we solve the Schrödinger equation for the system ($N \to \infty$) with one fermion and $H(U=0) = H_L + H_R + H_d$:

$$\begin{aligned} H\,|\psi\rangle &= \epsilon\,|\psi\rangle && (3.4)\\ |\psi\rangle &= \sum_j \psi(j) c_j^\dagger\,|0\rangle && (3.5)\\ H &= -\Gamma \sum_{\text{bulk}} \left(c_r^\dagger c_{r+1} + \text{H.c}\right) && (3.6)\\ &\quad -J\left(c_{-1}^\dagger c_0 + c_1^\dagger c_0 + \text{H.c}\right) \end{aligned}$$

where $\psi(j)$ and ϵ are respectively the unknown wave function and energy, to be determined. In the bulk, where $1 < |j|$, Eq. (3.4) gives the following form

$$\psi(j+1) + \psi(j-1) = -\frac{\epsilon}{\Gamma}\psi(i). \tag{3.7}$$

Textbooks tell that a solution (cf., e.g., Ref. [70]) is a superposition of an incident and a reflected plane waves on the left side and a transmitted plane wave on the right side of the dot with some momentum dependent amplitudes (Fig. 3.2):

$$\psi(j) = \begin{cases} e^{ikj} + B(k)e^{-ikj} & j < 0 \\ A(k)e^{ikj} & j > 0 \end{cases} \tag{3.8}$$

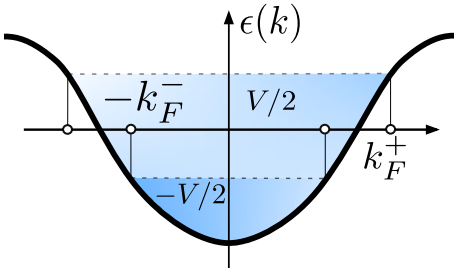

Figure 3.3: Band structure of a free-fermion lead. The blue regions are the Fermi seas of the left ($V/2$) and right ($-V/2$) leads.

This ansatz solves Eq. (3.7) and determines the form of the band (Fig. 3.3). The dispersion relation in the left and right leads has a simple cosine form and reads

$$\epsilon(k) = -2\Gamma\cos(k). \tag{3.9}$$

The bandwidth $W = \max(\epsilon) - \min(\epsilon) = 4\Gamma$ is the largest energy scale in this problem. The Fermi momentum $k_F^\pm$ is defined by a particle density in the leads $\pm V/2$ and is given by $2\Gamma\cos(k_F) = \pm V/2$. In the following, we set the hopping amplitude in the bulk to be $\Gamma = 1$ for simplicity.

The Schrödinger equation in the vicinity of the dot [Eq. (3.7)] determines the scattering coefficients $A(k)$ and $B(k)$. It has the following form:

$$\begin{aligned} \psi(-2) + J\psi(0) &= -\epsilon\psi(-1) && (3.10)\\ J\psi(-1) + J\psi(1) &= -\epsilon\psi(0) && (3.11)\\ J\psi(0) + \psi(2) &= -\epsilon\psi(1) && (3.12) \end{aligned}$$

To solve this, as a first step, we compare Eq. (3.10) with Eq. (3.12) and eliminate $J\psi(0)$:

$$\begin{aligned} \psi(-2)+\epsilon\psi(-1) &= \psi(2)+\epsilon\psi(1) \\ e^{-2ik}+Be^{2ik}-(e^{ik}+e^{-ik})(e^{-ik}+Be^{ik}) &= Ae^{2ik}-(e^{ik}+e^{-ik})Ae^{ik} \\ 1+B &= A, \end{aligned} \tag{3.13}$$

where B is the amplitude coefficient of reflected mode and A that of the transmitted mode. The next step is to substitute the Eq. (3.13) for Eq. (3.11) and then solve Eq. (3.12). The result reads

$$\psi(0) = J\left(1-\frac{2}{\epsilon}Be^{ik}\right) \tag{3.14}$$

$$B = \frac{\epsilon(J^2-1)}{\epsilon+2J^2e^{ik}}. \tag{3.15}$$

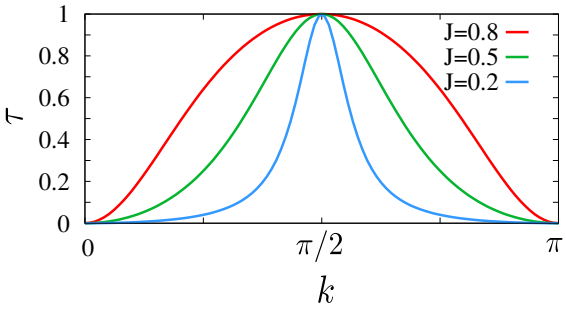

Figure 3.4: Tunneling probability $\mathcal{T}$ as a function of momentum k for different values of hopping amplitude J.

From the equation above one can then simply get Eq. (3.3) as $\mathcal{T}(k) = |1+B(k)|^2$. This result can be checked in two simple limits. In a uniform system with fully connected wires, where $J = 1$, the reflection probability $\mathcal{R}(k) = |B|^2$ vanishes and therefore plane waves simply propagate in the system. Meanwhile, for disconnected wires $J = 0$, particles remain in the left lead , i.e $\mathcal{T}(k) = |A|^2 = 0$.

3.2.2 From the transmission coefficients to the steady current

To obtain the current as a function of the bias in the noninteracting case, we use the semiclassical hydrodynamic description of the noninteracting steady state. It is also here equivalent to the Landauer-Büttiker formula [71, 6, 5, 7]. One obtains the dc current I:

$$I = \int_{k_F^-}^{k_F^+} \frac{dk}{2\pi}\mathcal{T}(\epsilon(k))v(k) \tag{3.16}$$

where the Fermi momenta $k_F^{\pm}$ in both leads are related to the voltage bias through $\epsilon(k_F^{\pm}) = \pm V/2$ (Fig. 3.3) and the group velocity $v(k)$ is, by definition, $v(k) = \frac{\partial\epsilon(k)}{\partial k}$. Changing the integration variable from k to ϵ gives the standard result :

$$I = \int_{-V/2}^{V/2} \frac{d\epsilon}{2\pi}\mathcal{T}(\epsilon). \tag{3.17}$$

For the RLM, using Eq. (3.3), the integral gives:

$$\begin{aligned} 2\pi I &= -V\frac{J^4}{a}+4J^2\frac{(1-J^2)^2}{a^{\frac{3}{2}}}\arctan\left(\frac{\sqrt{a}}{4J^2}V\right) \\ a &= 1-2J^2 \end{aligned} \tag{3.18}$$

where we assumed, $V < 4$ and $J^2 < 1$. This function is plotted in Fig. 3.7 for three different values of J. In the *scaling* limit where $J \ll 1$ we naturally define a new energy scale, so called *Kondo* energy $t_B = J^2$, which separates low IR and high UV energies and, generally speaking, depends on the interaction strength U [see Sec. 3.3.3].

The Eq. (3.18) simplifies to

$$\frac{2\pi I}{t_B} = 4 \arctan\left(\frac{V}{4t_B}\right), \tag{3.19}$$

in agreement with Ref. [2, 4].

The Kondo problem originates from scattering conducting electrons on a spin impurity, which leads to the Kondo effect – an increase of resistivity with decreasing temperature. Although the fermions of the IRLM are spinless and the dot only has some charge degree of freedom, the model captures some important aspects of the impurity Physics and shares many concepts with the Kondo model. Moreover the IRLM is directly related to some limit of the "s-d exchange" Kondo model [1], and the RLM (at which $U = 0$) corresponds to the, so-called, "Toulouse"[66] point [42, 43, 55, 72]. Also, the noninteracting RLM has been used to fit the experimental magnetic isotherms as a function of magnetic field in some Kondo systems, for which it gives a reasonably good fit [73].

The scale t_B defined above is often called a Kondo energy. It is the scale which separates a regime of small kinetic energy ϵ_k where the incoming fermions are perfectly transmitted from another regime of large ϵ_k (but still small compared to the bandwidth) where they are completely reflected. This is somewhat analogous to the Kondo temperature in Kondo problems, below which the magnetic impurity is "screened" by the conduction electrons and becomes invisible in transport measurements [39].

3.2.3 Time evolution of the current and approach to the steady-state

In this paragraph we discuss the way the current in the center of the system approaches its steady value, after some damped oscillations. Some typical time evolutions of the current are shown in Fig. 3.5 (a) for different values of the bias V, and in Fig. 3.6 for different values of the hopping J to the dot.

Generically, the current oscillates and, after long enough time, it reaches a steady value. This is most easily seen at low J. In most cases the *decay time* is proportional to the new inverse of the energy scale of the problem, t_B. In the non-interacting problem ($U = 0$) this scale is $t_B = J^2$ [see Eq. (3.19)]. The oscillations which appear in the transient regime have a well-defined period T_{osc}. It was argued in Ref. [63] that this period is simply given by the bias: $T_{\text{osc}} = 4\pi/V$. Note that the expression $I(t)$ of the current at finite time and $U = 0$ can be found in the appendix of Ref. [74]. In part because of these oscillations, it is not possible to extract reliably the steady current from finite-time simulations if V is too low, and this remains true in presence of interactions. In practice we therefore focus of values of V or order 1.

To extract the steady value from Figs. 3.5 (a) and 3.6 [see Fig. 3.10, 3.12], we fit the bare data with a function $f(t) = I + A\exp(-t/t_{\text{damping}})\cos(Vt/2 + \phi)$, where $I, A, t_{\text{damping}}, \phi$ are unknown fitting parameters. The same type of fitting function

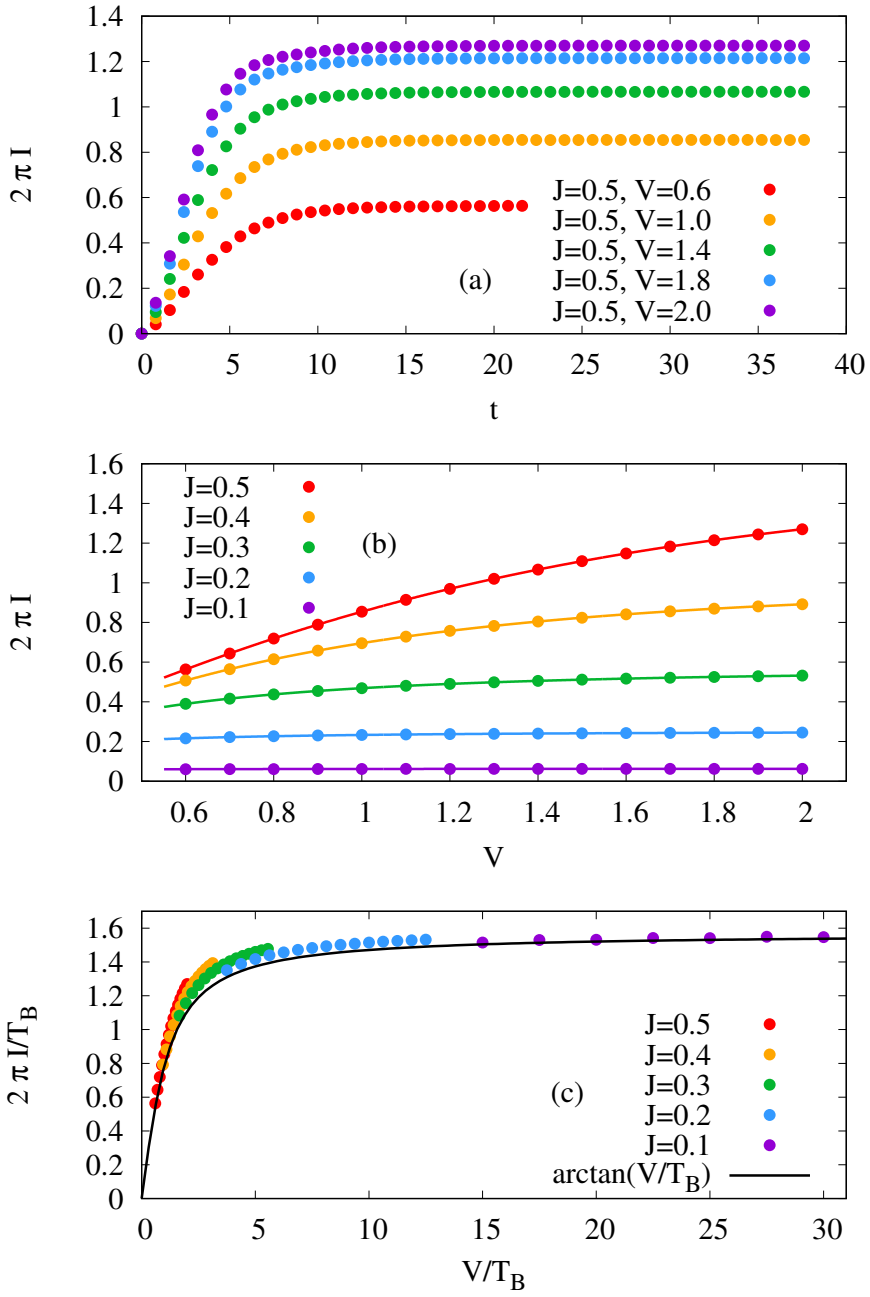

Figure 3.5: Panel (a): current as a function of time for fixed hopping J. Color points represent the DMRG data for different values of the bias V, namely red - 0.6, orange - 1, green - 1.4, blue - 1.8 and violet - 2. After some time the current reaches a stationary value that depends on V. Panel (b): steady current as a function of the bare bias $0.6 \leq V \leq 2$ for different values of the hopping J. Panel (c): the rescaled steady current vs rescaled voltage. Bare data of the panel (b) are rescaled by function $t_B = 4J^2$ and it collapses to a single master curve Eq. (3.18). For details see Fig. 3.7.

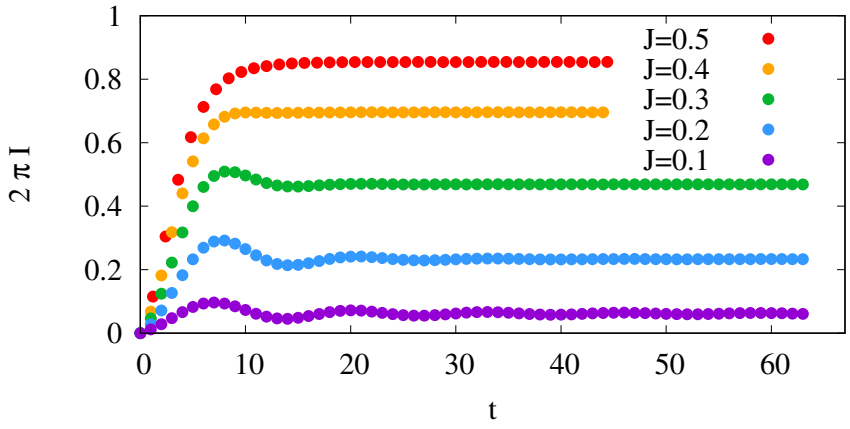

Figure 3.6: Current I at free fermion point ($U = 0$) as a function of time for different values of hopping amplitude J. A period of damped oscillation determined by the voltage $T_{\rm osc} = 4\pi/V$, a relaxation time $t_{damping} \approx \mathcal{O}(J^2)$, and converges to Eq. (3.19) when $t \to \infty$.

will be used when analyzing the numerical data obtained in presence of interaction ($U \neq 0$).

3.2.4 I-V characteristics and finite-J corrections

The results of the fitting procedure described in the previous paragraph are plotted in the Fig. 3.5(b), as a function of V and for several values of J. We see that for large values of the hopping ($J \approx 0.5$), the current monotonically grows with the bias V. The solid colored lines represent the analytical result of Eq (3.18), while the dots represent the DMRG data. The agreement is perfect at this scale, which is a nontrivial check of the DMRG results, and a nontrivial check of the procedure used to estimate the steady current from finite-time simulations.

As a next step we *rescale* each I-V data point of the Fig. 3.5(b) by its a factor $t_B = J^2$. This has the effect of moving the curves along the main diagonal until they match. The result is presented in Fig. 3.5(c) and Fig. 3.7. As we expect, the rescaled DMRG data perfectly agrees with Eq. (3.18) and slightly deviates from the analytical curve Eq. (3.19) due to finite J corrections. This deviations vanishes with decreasing J. In most of this study we will be interested in the regime where J is small enough, and where such corrections are negligible.

We know from Eq. (3.19) that the current is linear in bias for low values of V: $I \sim \frac{V}{2\pi}$. The conductance therefore goes to a constant, $G = \partial I/\partial V|_{V=0} = 1/(2\pi)$. Getting the steady current at low V is difficult from real time numerics, but since I/t_B is a function of V/t_B, the regime where $G \simeq 1/(2\pi)$ can be approach by choosing a larger J, hence a larger t_B [see for instance $J = 0.5$ in Fig. 3.5(c)]. On the other hand, taking J small amounts to explore a regime where the rescaled bias V/t_B is large. This is realized with $J = 0.1$ in Fig. 3.5(c)

3.2.5 IR and UV

The domain of low rescaled bias V/t_B is called the *infrared regime* (IR). In this regime J and t_B are relatively large and comparable with a fraction of the bandwidth

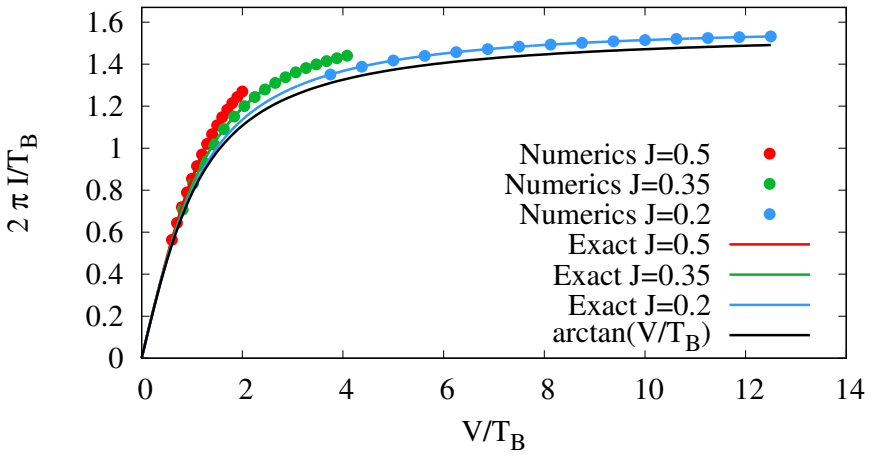

Figure 3.7: Rescaled steady current as a function of the rescaled voltage in the free case ($U = 0$), using $t_B = J^2$. The symbols represent the DMRG data for three different values of J, and the full lines are respectively the exact result (Eq. 3.18) for $J = 0.5$ (red), for $J = 0.35$ (green), for $J = 0.2$ (blue), and the limit when J is small (Eq. 3.19, black). The DMRG data are in perfect agreement with the exact results, but since chosen J are not very small one observes some deviations from Eq. (3.19).

($W = 4$). The dot and the two wires are strongly *hybridized*, and the current is a linear function of the bias in this regime, with transmission probability close to 1. Even thought the hopping to the dot is done via a weak bond ($J < \Gamma = 1$), the fermions go from one lead to the other with almost perfect transmission. On the other hand, the large rescaled bias (V/t_B) regime is called the *ulraviolet regime* (UV). The hopping amplitude J and the Kondo temperature t_B are small, the wires are almost decoupled and therefore the transmission probability $\mathcal{T} \to 0$.

3.3 The continuum limit of the IRLM

As mentioned in the introduction, we focus on the regime where the free fermion bandwidth $W = 4\Gamma = 4$ is larger than all the other energies in the problem, namely J and V.[2]

In this regime the microscopic details of the leads (like the band structure) are irrelevant, except for the Fermi velocity ($v_F = 2\Gamma = 2$), and their gapless low-energy excitations are described in the continuum limit in terms of simple scale-invariant Hamiltonians. Linearizing the dispersion relation in the vicinity of the two Fermi points gives left- and right-moving relativistic fermions:

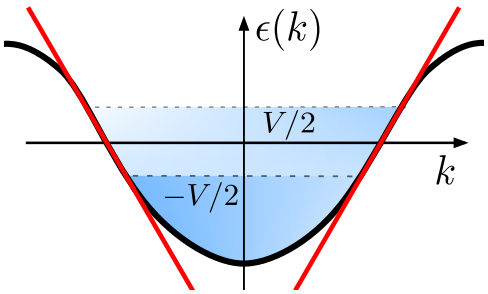

Figure 3.8: Band structure on the lattice and linear dispersion in the vicinity of the Fermi points.

$$H_A^c = iv_F \int_{-\infty}^{0} dr \left[\psi_L^\dagger(r)\partial_r\psi_L(r) - \psi_R^\dagger(r)\partial_r\psi_R(r)\right] \tag{3.20}$$

$$H_B^c = iv_F \int_{0}^{\infty} dr \left[\psi_L^\dagger(r)\partial_r\psi_L(r) - \psi_R^\dagger(r)\partial_r\psi_R(r)\right]. \tag{3.21}$$

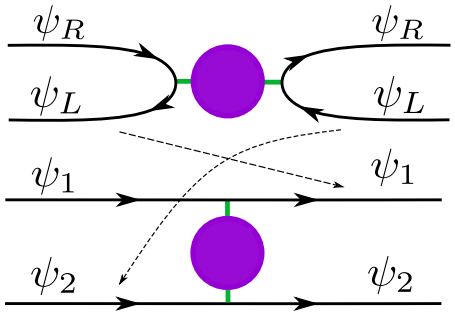

Figure 3.9: Unfolding schematics. In the upper panel we have the left lead connected to the right lead via hopping terms (green line) to the dot (purple). In both leads fermions can move to the left (ψ_L) or to the right (ψ_R). The lower panel is the unfolded representation of the same problem, with right-movers only (ψ_1 and ψ_2).

H_A^c describes the continuum limit of the left lead ($r < 0$), H_B^c describes that of the right lead ($r > 0$), and ψ_L and ψ_R are the left- and right-moving fermion annihilation operators. The coupling to the dot then takes the form

$$\begin{aligned} H_d^c = & -J_c\left(\psi_L(0) + \psi_R(0)\right) d^\dagger + \text{H.c.} \\ & + U_c\left(:\psi_L(0)^\dagger\psi_L(0): + :\psi_R(0)^\dagger\psi_R(0):\right) \\ & \times \left(d^\dagger d - \frac{1}{2}\right), \end{aligned} \tag{3.22}$$

where d is the fermion operator associated to the dot, U_c is the interaction strength [see Sec. 3.3.4], the normal ordering is defined as $:A := A - \langle A\rangle$. The analysis of this model then usually proceeds by "unfolding" the two semi-infinite leads, giving two infinite right moving Fermi wires.

Left movers in the left wire can be interpreted as right movers in the right wire due to the shared boundary conditions, as in Fig. 3.9:

$$\psi_1 = \theta(-x)\psi_R(x < 0) + \theta(x)\psi_L(x < 0)$$
$$\psi_2 = \theta(-x)\psi_L(x > 0) + \theta(x)\psi_R(x > 0)$$

With this, the unfolded Hamiltonian with two right moving Fermi wires [75] reads:

[2] In practice we take $\Gamma = 1$ and restrict our numerical simulations to $V \lesssim 2$ and $J \lesssim 0.5$. Finite-J corrections start to be visible for $J = 0.5$ and small U[see Fig. 3.7].

$$H_{\rm L} = -iv_F \sum_a \int \psi_a^\dagger \partial_x \psi_a \tag{3.23}$$

$$\begin{aligned} H_d^c &= -J_c \left(\psi_1(0) + \psi_2(0)\right) d^\dagger + \text{H.c.} \\ &\quad + U_c \left(: \psi_1(0)^\dagger \psi_1(0) : + : \psi_2(0)^\dagger \psi_2(0) :\right) \\ &\quad \times \left(d^\dagger d - \frac{1}{2}\right). \end{aligned} \tag{3.24}$$

We then introduce new *odd* and *even* fermionic fields

$$\begin{aligned} \psi_- &= \frac{\psi_1 - \psi_2}{\sqrt{2}} \\ \psi_+ &= \frac{\psi_1 + \psi_2}{\sqrt{2}}. \end{aligned} \tag{3.25}$$

One finds that the odd field ψ_- decouples from the dot, i.e. no hopping, and one obtains:

$$H_{\rm L} = -iv_F \sum_{a=\pm} \int \psi_a^\dagger \partial_x \psi_a \tag{3.26}$$

$$\begin{aligned} H_d^c &= -J_c \sqrt{2} \psi_+ d^\dagger + \text{H.c.} \\ &\quad + U_c \left(: \psi_+(0)^\dagger \psi_+(0) : + : \psi_-(0)^\dagger \psi_-(0) :\right) \\ &\quad \times \left(d^\dagger d - \frac{1}{2}\right). \end{aligned} \tag{3.27}$$

3.3.1 Bosonization

As usually done in the field of one-dimensional interacting fermion problems [34], we introduce bosonic fields $\phi_1(x)$ and $\phi_2(x)$, such that the fermions are represented as

$$\psi_\pm(x) = \frac{\eta_{1,2}}{\sqrt{2\pi}} e^{i\sqrt{4\pi}\phi_{1,2}(x)}. \tag{3.28}$$

We represent the impurity degree of freedom by spin 1/2 operators:

$$S^z = d^\dagger d - \frac{1}{2}, \qquad d^\dagger = \eta S^+, \qquad d = \eta S^-. \tag{3.29}$$

Here η and $\eta_{1,2}$ are Klein factors, which enforce the anticommutation relations of the different species of Fermions ($\psi_\pm$ and d).

In terms of the bosonic fields the full Hamiltonian takes the form

$$\begin{aligned} H_{\rm IRLM} = \frac{v_F}{2} \sum_{a=1,2} \int dx \left(\partial_x \phi_a\right)^2 + \frac{J_c}{\sqrt{\pi}} \left(\eta \eta_1 S^+ e^{i\sqrt{4\pi}\phi_1(0)} + H.c\right) \\ + \frac{U_c}{\sqrt{\pi}} S^z \left(\partial_x \phi_1(0) + \partial_x \phi_2(0)\right) \end{aligned} \tag{3.30}$$

In the following of this section we will take $v_F = 1$ for simplicity.

3.3.2 Elimination of the interaction term

Now we apply a unitary transformation $\mathcal{U}$ to eliminate the boundary interaction [76, 77, 78] term proportional to U:

$$\mathcal{U} = \exp\left(i\alpha S^z \left[\phi_1(0) + \phi_2(0)\right]\right). \tag{3.31}$$

The operator $\mathcal{U}$ depends only on the spin operator S^z and the bosonic fields $\phi_{1,2}$, with α an unknown coefficient to be determined. We will act now on every single term of H to see how this transformation works.

First, we act on the kinetic part and to do so we use Baker–Campbell–Hausdorff (BCH) formula:

$$e^{-i\alpha B} A e^{i\alpha B} = A + i\alpha[A, B] + \frac{(i\alpha)^2}{2}[[A, B], B] + ... \tag{3.32}$$

then the transformation reads

$$\mathcal{U}^\dagger H_{\text{kin}} \mathcal{U} = \tag{3.33}$$

$$e^{-iS^z\alpha(\phi_1(0)+\phi_2(0))} \left(\frac{1}{2}\sum_{a=1,2}\int dx\,(\partial_x\phi_a)^2\right) e^{iS^z\alpha(\phi_1(0)+\phi_2(0))} =$$

$$\sum_{a=1,2}\int dx\,(\partial_x\phi_a)^2 + i\frac{\alpha}{2}S^z\sum_{a,b=1,2}\int dx\Big[(\partial_x\phi_a)^2, \phi_b(0)\Big] + ... =$$

$$H_{\text{kin}} - \alpha\frac{1}{2}S^z\sum_{a=1,2}\partial_x\phi_a(0), \tag{3.34}$$

where we used the following commutation relations for the bosonic fields

$$\Big[\partial_x\phi_a, \phi_b\Big] = \frac{i}{2}\delta_{ab}\delta(x-y). \tag{3.35}$$

Field operator $\phi(x)$ commutes with $\delta(x)$-function and therefore all higher term of the transformation Eq. (3.34) are zero. As a next step, we transform the interaction term H_U:

$$\begin{aligned}\mathcal{U}^\dagger H_U \mathcal{U} &= e^{-iS^z\alpha(\phi_1(0)+\phi_2(0))}\left(\frac{U_c}{\sqrt{\pi}}S^z\sum_{a=1,2}\partial_x\phi_a(0)\right)e^{iS^z\alpha(\phi_1(0)+\phi_2(0))} \\ &= \frac{U_c}{\sqrt{\pi}}S^z\sum_{a=1,2}\partial_x\phi_a(0) - \frac{\alpha U_c}{8\sqrt{\pi}}\delta(0).\end{aligned} \tag{3.36}$$

The second term of the transformed Hamiltonian H_U acquires an infinite constant, which can be dropped.

The higher terms of Eq. (3.36) vanish, since constants (here delta-function) commute with field operators. Thus, the unitary transformation $\mathcal{U}$ leaves H_U unchanged (up to the dropped term). Now, one can notice that the transformed kinetic and the density interaction Eq.(3.34),(3.36) terms have a similar form, therefore it is possible to eliminate the term proportional to U_c with a proper choice of α, i.e.:

$$\left(\alpha - \frac{U_c}{\sqrt{\pi}}\right)S^z\sum_a\partial_x\phi = 0, \tag{3.37}$$

$$\alpha = \frac{U_c}{\sqrt{\pi}}. \tag{3.38}$$

A similar trick was applied in [72]

Now we transform the hopping term H_J:

$$\mathcal{U}^\dagger H_J \mathcal{U} = e^{-iS^z\alpha(\phi_1(0)+\phi_2(0))}\ \frac{J_c}{\sqrt{\pi}}\left(\eta\eta_1 S^+ e^{i\sqrt{4\pi}\phi_1(0)}\right)\ e^{iS^z\alpha(\phi_1(0)+\phi_2(0))} \tag{3.39}$$

The unitary operator $\mathcal{U}$ leaves the bosonic fields $\phi_1(0)$ unchanged and only spin operators $S^\pm$ do not commute with $\mathcal{U}$:

$$\begin{aligned}\mathcal{U}^\dagger S^+ \mathcal{U} &= S^+ + i\alpha\left(\phi_1+\phi_2\right)[S^+,S^z] + \\ &\quad \frac{\left(i\alpha\left(\phi_1+\phi_2\right)\right)^2}{2!}[[S^+,S^z],S^z] + ...\end{aligned} \tag{3.40}$$

To simplify this expression, we use the standard spin commutators :

$$[S^+,S^z] = -S^+, \quad [S^-,S^z] = S^-, \tag{3.41}$$

With the above, we get

$$\begin{aligned}\mathcal{U}^\dagger S^+ \mathcal{U} &= S^+ e^{-i\alpha(\phi_1(0)+\phi_2(0))} \\ \mathcal{U}^\dagger S^- \mathcal{U} &= S^- e^{i\alpha(\phi_1(0)+\phi_2(0))}\end{aligned} \tag{3.42}$$

and thus we obtain

$$\mathcal{U}^\dagger H_J \mathcal{U} = \frac{J}{\sqrt{\pi}}\eta\eta_1 S^+ e^{i(\sqrt{4\pi}-\alpha)\phi_1(0)-i\alpha\phi_2(0)} + H.c \tag{3.43}$$

The unitary transformation allows to rewrite the IRLM in the continuum as [79, 1]

$$H_{\text{IRLM}} = \frac{1}{2}\sum_{a=1,2}\int dx\,(\partial_x\phi_a)^2 + \frac{J}{\sqrt{\pi}}\eta\eta_1 S^+ e^{i(\sqrt{4\pi}-\alpha)\phi_1(0)-i\alpha\phi_2(0)} + H.c \tag{3.44}$$

Finally, we rewrite Klein factors to be $\kappa_+ \equiv \eta\eta_1$ and define new bosonic fields $\phi_\pm = \frac{1}{\beta}\left[(\sqrt{4\pi}-\alpha)\phi_{1,2} \mp \alpha\phi_{2,1}\right]$, where $\beta^2 = \frac{2}{\pi}(\alpha\sqrt{\pi}-\pi)^2+2\pi$. Hamiltonian obtains a following form

$$H^{(1)}_{\text{IRLM}} = \sum_{a=\pm} H_0(\phi_a) + \frac{J_c}{\sqrt{\pi}}\kappa_+\left[e^{i\beta\phi_+(0)}S_+ + \text{H.c}\right] \tag{3.45}$$

where $H_0(\phi_a) = \frac{1}{2}\int dx(\partial_x\phi_a)^2$ is the free boson Hamiltonian. The self-dual case is $U_{sd} = \pi$ corresponding to $\beta = \sqrt{2\pi}$, where , while the non-interacting case is $U_c = 0$ and therefore $\beta = \sqrt{4\pi}$.

The Hamiltonian above is a bosonised version of anisotropic Kondo model (AKM) [1, 80]. In the AKM formulation, the second term is the operator responsible for the tunneling between the two chiral wires. It only acts in $r = 0$ and can be viewed as a boundary perturbation. One important characteristic of the IRLM, which determines the important energy scale and which appears in all the transport properties, is the anomalous dimension g of the above boundary perturbation.

3.3.3 Scaling dimension of the boundary term

To obtain the scaling dimension of an operator, we can look at its two-point function. In the case of vertex operators:

$$\langle e^{i\beta\phi(x)}e^{-i\beta\phi(y)}\rangle = \langle e^{i\beta(\phi(x)-\phi(y)}\rangle e^{-\frac{\beta^2}{4\pi}\ln|x-y|} = |x-y|^{-\frac{\beta^2}{4\pi}} = |x-y|^{-2g}, \tag{3.46}$$

where $g \equiv \beta^2/8\pi$ is a positive non-integer value that controls decay as a function of distance. The correlation functions of the IRLM in bosonic terms has form

$$\langle e^{i\beta_1\phi_1(x)}e^{i\beta_2\phi_2(x)}e^{-i\beta_2\phi_2(y)}e^{-i\beta_1\phi_1(y)}\rangle = |x-y|^{-\sum_{j=1,2}\beta_j^2/4\pi}, \tag{3.47}$$

$$\beta_1 = \sqrt{4\pi} - K\alpha, \quad \beta_2 = -K\alpha. \tag{3.48}$$

In the last line we have used the coefficients of $\phi_1(0)$ and $\phi_2(0)$ appearing in Eq. (3.44). Finally we find that the anomalous scaling has a form

$$g = \frac{1}{2} - \alpha + \alpha^2 = \frac{1}{4} + \left(\frac{1}{2} - \frac{U_c}{2\pi}\right)^2 \tag{3.49}$$

Since the tunneling to the dot is a relevant interaction, a Kondo energy scale t_B appears when the leads are connected to the dot, and most quantities are expected to follow some single-parameter scaling with t_B. At energies that are small compared to the crossover scale t_B, the dot is hybridized with the leads, and the system effectively appears as a single chain (so called "healing"), whereas the wires appear to be almost disconnected at energies much larger than t_B. As for the interaction U, it corresponds to a marginal operator and therefore changes continuously the critical properties of the model. Although this is well established for equilibrium properties, it is less obvious that T_B also rules the out-of-equilibrium properties. Such behavior is nevertheless verified for the current I, which, for a given U, takes the form $I/t_B = f(V/t_B)$ [2]. The role played by t_B in the dynamics of the IRLM has also been investigated in the absence of any bias ($V = 0$), in a local quench setup when the leads are abruptly connected to the dot at $t = 0$ [81, 82].

The energy t_B is known to scale as (e.g. Ref [78])

$$t_B \sim J^{\frac{1}{1-g}}, \tag{3.50}$$

where g is the scaling dimension of the operator which, in the continuum description, describes the tunneling from the leads to the dot. For free fermions we have $U_c = 0$ and Eq (3.49) therefore gives $g = 1/2$. It means that Kondo temperature t_B is indeed $\sim J^2$ in that case, as found by a direct calculation of the steady current (Sec. 3.2).

3.3.4 Duality

The IRLM possesses a certain duality, which is encoded in the Eq. (3.49). The interaction strength in continuum U_c could be interpreted as a scattering phase

factor [83] and it has a simple relation with the interaction U on the lattice (see the supplemental material of Ref. [9]):

$$U_c = \begin{cases} 4\arctan(U/2), & U < 2 \\ 4\arctan(2/U), & U > 2. \end{cases} \tag{3.51}$$

Notice, the scaling dimension g of the Eq. (3.49) is unchanged under

$$U_c \rightarrow U_c' = 2\pi - U_c \tag{3.52}$$

or

$$U \rightarrow U' = \frac{4}{U} \tag{3.53}$$

In our case U_c varies between 0 and $U_c = 2\pi$. $U_c = 0$ corresponds to free fermions on the lattice ($U = 0$) while $U_c = 2\pi$ corresponds to $U \to \infty$ on the lattice. The anomalous dimension g is a quadratic function in U_c and in the region $U_c < \pi$ it give the same values as for $U_c > \pi$. So the infinite interacting $U \to \infty$ case is expected be dual to the free $U = 0$ problem [83].

The most remarkable point is $U_c = \pi$, the so called *self-dual* point. For this particular value $g = 1/4$ (and for free case $g = 1/2$) the IRLM could be mapped to the Boundary sine-Gordon (BSG) model, where the boundary plays a role of the impurity. The BSG was solved out-of-equilibrium by Bethe ansatz this solution allowed to construct non-equilibrium transport properties, like $I-V$ characteristics [84, 56]. Both models exhibit the same behavior at large voltage, where the current vanishes as a power law, $I \sim V^{-b}$. The exponent b is related to the dimension g of the boundary perturbation:

$$b = 1 - 2g. \tag{3.54}$$

Using Eq. (3.49) we obtain this exponent using the interaction parameter U_c of the IRLM,

$$b = 1 - 2g = \frac{U_c}{2\pi}\left(2 - \frac{U_c}{\pi}\right). \tag{3.55}$$

At the self-dual point b reaches the maximum and the BSG solution predicts $b = 1/2$. We emphasize that the current has the same vanishing behavior for both models. This fact plays an important role in mapping IRLM onto BSG. The Eq. (3.55) allows to reformulate the Kondo temperature in terms of the current exponent

$$t_B(J, U) = J^{\frac{1}{1-g(U)}} = J^{\frac{2}{1+b}} \tag{3.56}$$

Thus the energy scale t_B controls the in- and out-of-equilibrium behavior of the IRLM, at least at the two points where it is equivalent to the BSG.

3.4 Self-dual point

In this section we discuss a special point of the IRLM, where some out-of-equilibrium properties – not only the mean value of the steady current but also the full counting statistics [see Sec. 3.5.3] – have been computed exactly [2]. This point corresponds to $U = 2$ (in the scaling regime), and we show that the numerical simulations carried out at this point are in excellent agreement with the analytical results.

3.4.1 Analytical result for the current

The analytical results of Ref. [2] were obtained in the continuum limit at $U = 2$ ($U_c = \pi$), where the model has some self-duality property and can be mapped onto the BSG model [see Sec. 3.3]. As it was mentioned before, the BSG model is integrable and could be solved by Bethe ansatz. In addition to the $I-V$ characteristics, the *full counting statistics* $\langle e^{i\chi\hat{Q}}\rangle$ (FCS) and therefore the *noise* and all higher charge $\hat{Q}$ cumulants are known for this model. The current I is the (time derivative of the) transfered charge, and could be obtained by simple derivation of the FCS function $I = \frac{1}{i}\partial F/\partial\chi$, see 3.5.3. The FCS as well as the current of this model are generalized hyper-geometric functions [85] of the form ${}_pF_q(a,b;z)$ and could be represented as a two infinite series in the vicinity of 0 and ∞. The current has the following form [2, 56]:

$$I(V) = \begin{cases} V\sum\limits_{n\geq 0} \dfrac{(-1)^n}{4\sqrt{\pi}} \dfrac{(4n)!}{n!\Gamma\left(3n+\frac{3}{2}\right)} \bar{V}^{6n}, & V < e^{\Delta} \\ V\sum\limits_{n>0} \dfrac{(-1)^{n+1}}{4\sqrt{\pi}} \dfrac{\Gamma(1+\frac{n}{4})}{n!\Gamma\left(\frac{3}{2}-\frac{3n}{4}\right)} \bar{V}^{\frac{3n}{2}}, & V > e^{\Delta} \end{cases} \tag{3.57}$$

where $e^{\Delta} = \frac{\sqrt{3}}{4^{2/3}} \approx 0.7$ and $\bar{V} = \frac{\Gamma(1/6)}{4\sqrt{\pi}\Gamma(2/3)} \frac{V}{t_B}$ is the rescaled voltage. The parameter Δ defines a convergence radius of the series. In the above formula, the Kondo scale of the IRLM (and therefore of the BSG model) at the self-dual point is given by $t_B \sim J^{4/3}$.

For comparison, recall that (see 3.2.2) the rescaled current for free $U = 0$ case is $2\pi I/t_B = \arctan(V/t_B)$, and is a function of the rescaled voltage. Similarly, the self-dual current Eq. (3.57) depends only on a single parameter V/t_B, where t_B now scales as $t_B \sim J^{4/3}$.

Thanks to numerical simulations, it has been shown that the lattice model at $U \simeq 2.0$ has a continuum limit which is close to the self-dual point, where the exponent g Eq. (3.49) reaches a minimum [2]. It was later realized [9] that the self-dual point in fact *exactly* corresponds to $U = 2$ in the lattice model. We have then confirmed this result [10].

In the limit of large (rescaled) bias V/t_B, the rescaled steady current behaves as a power law: $I \sim V^{-b}$ with $b = 1-2g$ [2]. For the self-dual point $U = 2$ the current has a form:

$$\frac{I}{t_B}|_{V/t_B\to\infty} \sim \left(\frac{V}{t_B}\right)^{-1/2}, \tag{3.58}$$

which is the first term in the series expansion Eq. (3.57) for $V > e^{\Delta}$. This behavior will be checked numerically in details in the next section (Sec. 3.4.2).

3.4.2 Numerics for the current

A typical current evolution in time at the self-dual point ($U = 2$) is plotted in Fig. 3.10. Despite a simple pattern of damped oscillations, there is no analytical solution for current time evolution for general U, besides free-fermionic case at small J limit [74]. The frequency of the current oscillations appears to be proportional to the bias $\omega = V/2$, but the other transient parameters of the time evolution,

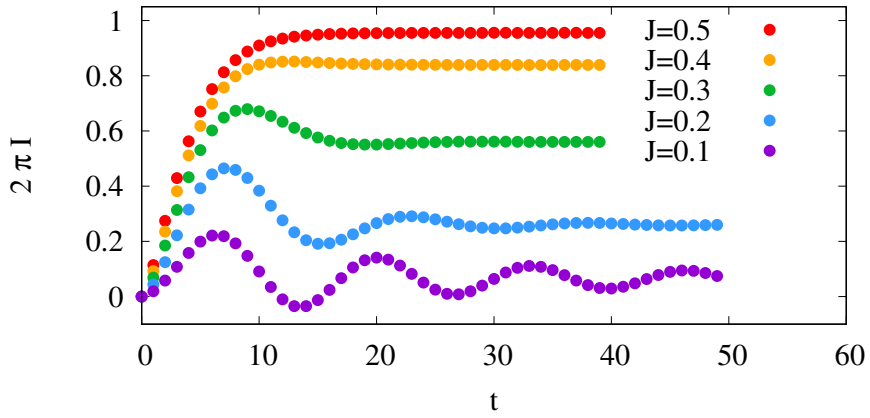

Figure 3.10: Current $I(t)$ as a function of the hopping J for $V = 1$ at the self-dual point $U = 2$, obtained from tDMRG simulations. After some damped oscillations the current reaches its steady value. The frequency of the oscillations depend only on the value of the bias: $\omega = V/2$ [see Sec 3.2.3].

such as a the damping time and an amplitude, remain unknown. The damping rate $\delta = 1/t_{\text{damp}}$ appears to be a monotonous function of the hopping amplitude J. The rate δ is large for large values of J, and in these cases the current reaches its steady value relatively fast, and the oscillations are hardly visible. On the contrary, in the small J regime δ is small and the oscillations become important. This is the UV regime where one can numerically determine the tunneling operator exponent g, which plays a central role in the next chapters.

As can be seen in Fig. 3.10 and Fig. 3.11, in the IR (large J) the relaxation

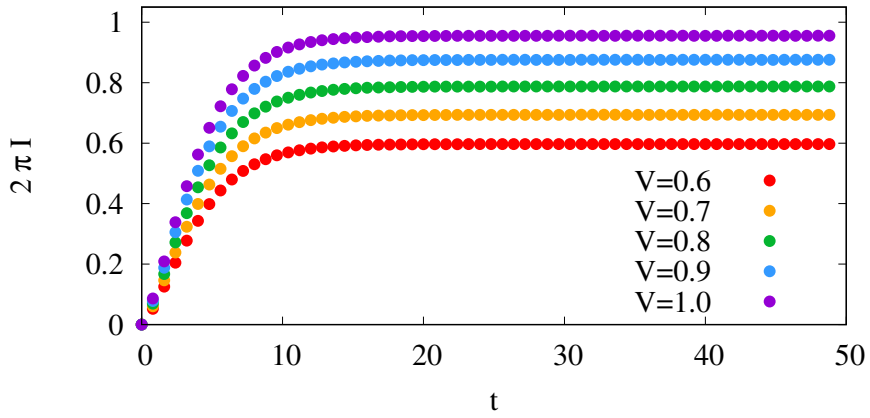

Figure 3.11: Time evolution of the current I at the self-dual point $U = 2$ for different values of the voltage V and fixed $J = 0.5$. The current has a familiar linear dependence on V in IR regime, as for $U = 0$ [see Sec. 3.2.3].

time t_{damping} is small, and the current oscillations no longer bother the analysis. Shorter times are therefore enough to estimate the current steady values. We use a fitting function with damped oscillations $f(t) = I + A\exp(-\delta t)\cos(tV/2 + \phi)$ with a large decay rate δ. One can fit the IR (large J) data with just a constant function $f_0(t) = I$, which gives the same result as $f(t)$. The fitting results of I are presented in the Fig. 3.13. For large J, the current is linear in V at small bias.

The different data for J from $J = 0.5$ to $J = 0.3$ coincide here. We expect that the current for $J = 0.1$ and $J = 0.2$ also should be linear in the vicinity of the $V \approx 0$. Unfortunately, one needs long simulation times (and also a large system size) to access the steady state when J (and thus t_B) is small. Since the frequency is proportional to bias V, the oscillation period is $T_{\text{osc}} = 4\pi/V$. For $J = 0.1$ or $J = 0.2$ and bare voltage $V < 0.6$ this time is beyond the time reached by our simulations (Fig.3.12).

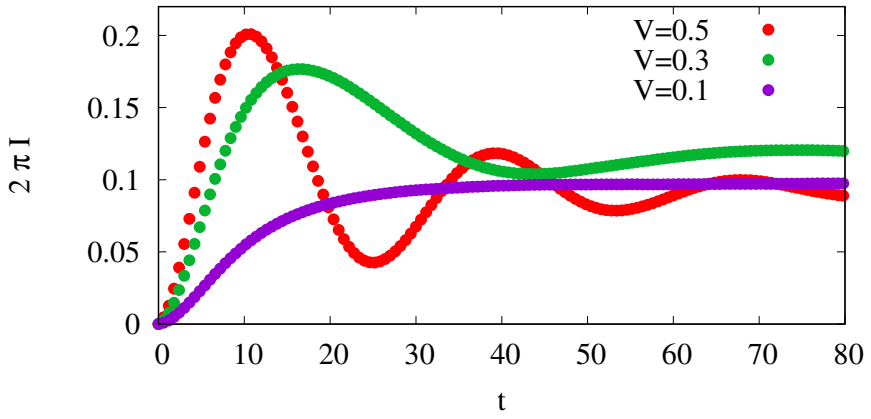

Figure 3.12: Time evolution of the current I at the self-dual point $U = 2$ for different values of the voltage V and fixed $J = 0.1$. The current oscillates in UV regime with a period $T_{\text{osc}} = 4\pi/V$. The period T_{osc} is greater than the numerical simulation time for low bare voltage. To avoid this problem we restrict the bare voltage to be $0.6 \lesssim V \lesssim 1.6$ in our calculations.

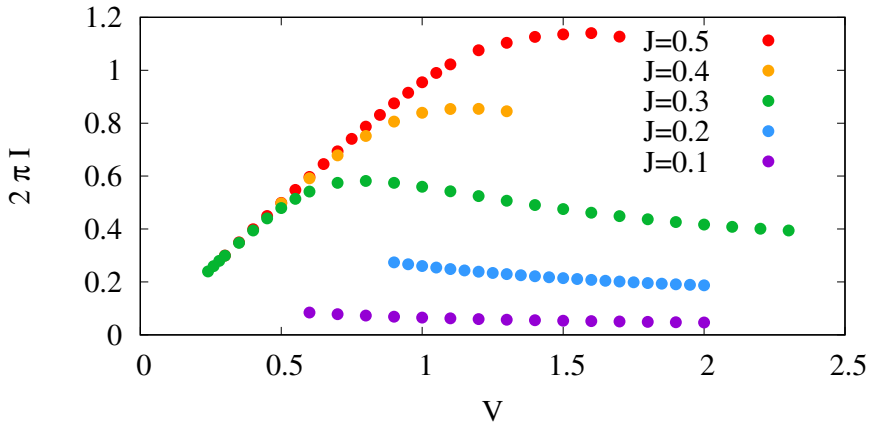

Figure 3.13: Current I as a function of the bias V at the self-dual point $U = 2$ for different values of the hopping amplitude J. The current has a familiar linear dependence on V in IR regime, as for $U = 0$ [see Sec. 3.2.3]. On the other hand, the UV regime shows a non-trivial behavior $I \sim V^{-1/2}$. These data are also plotted in Fig. 3.14 in rescaled form.

The Kondo temperature for the self-dual point t_B[3]$= J^{4/3} = J^{\frac{2}{1+1/2}}$, where the value $1/2$ is the current exponent b ($I \sim V^{-1/2}$). With the above t_B one can

[3]We adopt the convention where the numerical prefactor in the definition of t_B is set to 1.

define a rescaled current I/t_B and rescaled bias V/t_B. Each data set of Fig. 3.13 is rescaled by its own t_B and presented in Fig. 3.14. We reach almost a perfect

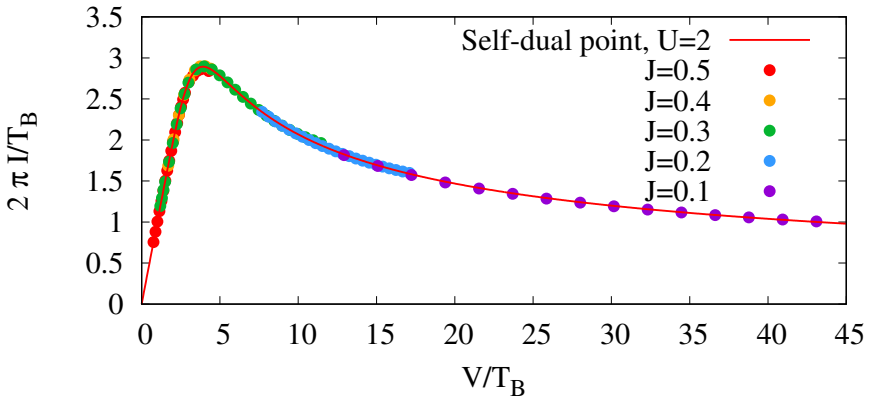

Figure 3.14: Rescaled current I/t_B as a function of the rescaled voltage V/t_B, where $t_B = J^{\frac{2}{1+0.5}} = J^{4/3}$. The colored points label the hopping J whereas the red solid line represents the exact solution Eq. (3.57) for the self-dual point.

collapse onto a single master curve, which is given by Eq. (3.57). This indicates that, with the present parameters, the lattice model is indeed close to the scaling regime, characterized by a single energy scale t_B. For $U = 2.0$ the collapse has already been observed by Boulat *et al.* [2], but thanks to longer simulations and larger systems, the present data have some higher precision and we could extend the $I - V$ curves to larger values of V/t_B [8, 10].

3.5 $I - V$ for arbitrary U

Although the IRLM is integrable [3], there are few exact results for the non-equilibrium transport properties away from the non-interacting fermions $U = 0$ [4, 5, 6, 7, 8] and the self-dual point $U = 2$ [2]. As we explained already, these two points could be solved by mapping the IRLM onto the boundary sine-Gordon (BSG), where $I - V$ characteristics is know. In this vein, the question naturally arises: to which extend the current I_{BSG} could also describe, at least approximately, the current of the IRLM *away* from the two cases above? In this section we attempt to answer this question.

3.5.1 Steady current in the UV

We study the $I - V$ characteristics for small hopping J and for different values of the interaction. As it is done in Sec. 3.2.3, we fit the bare time evolution data with a function $f(t) = I + A\exp(-t/t_{\mathrm{damp}})\cos(Vt/2+\phi)$ in order to estimate the steady value I. The results of the fits are presented in Fig. 3.15.

The steady current I indeed decays as a power law $\sim V^{-b(U)}$ for a positive values of the density-density interaction U. One may notice that the exponent b decreases as one reduces U from $U = 2$ to $U = 1$, and it almost vanishes at $U = 0.2$. At $U = 0$ the steady current stays constant at large voltage. Contrariwise, the steady current monotonously grows like $\sim V^{+b(U)}$ when $U < 0$. The free-fermionic case plays a border role in the IRLM, between positive interaction $U > 0$ and negative $U < 0$

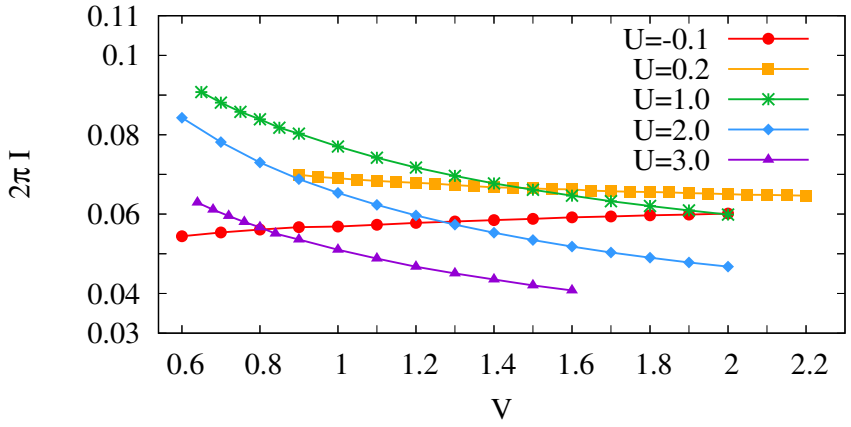

Figure 3.15: Stationary current I as a function of V for $J = 0.1$, for a few selected values of U. The current vanishes as $I \sim V^{-b(U)}$ for positive values of the Coulomb interaction U. The values $b(U)$ are displayed in Fig. 3.17.

one. As it was shown in Sec. 3.2.3, the current saturates to a constant in the UV limit and no longer depends on the voltage V, i.e. $I \sim V^0$. The aforesaid current behavior in the UV could be summarized as follows:

$$\lim_{\frac{V}{t_B}\to\infty} \frac{I}{t_B} = \begin{cases} \infty & U < 0 \\ \text{const} & U = 0 \\ 0 & U > 0 \end{cases}$$

To find the quantitative dependence between the exponent b and U, we extract $b(U)$ from the numerical data. In practice we can consider two ways to extract b from the $I-V$ data. The first method is to fit $I(V)$ to a power-law function $f_0(V) = A_0 V^{-b}$, A_0 and b being the fit parameters. The second method is to fit the current I in a log-log scale with a linear function $f(x) = -bx + k$ (with $x = \log V$ and $f \sim \log I$). The second approach is more preferable, it uses the least squares method which gives more accurate and stable results compare to a non-linear fit. The log-log method is also preferable because it gives a similar weight to the low- and high-bias data points.

We use a log-log scale in Fig. 3.16 to visualize the power-law behavior of the current $I \sim V^{-b(U)}$ at sufficiently large V/t_B, *i.e* small J. The slope of the curve in log-log scale allows to determine the exponent $b(U)$. For a given U, this offers a simple way to extract g and b from the simulations, and then to define $t_B = J^{\frac{2}{1+b}}$ as a function of J and U.

The anomalous dimension of the boundary perturbation $g(U)$ establishes a relation between the current exponent b and the strength U of density-density interaction [9]. Thanks to the analysis of the model in the continuum (Sec. 3.3), we know from Eqs. (3.51) and (3.55) that the exponent b can be put in the form

$$\begin{aligned} b(U) &= \frac{1}{2} - 2\left(\frac{1}{2} - \frac{4}{2\pi}\arctan\left[U/2\right]\right)^2 \\ &= \frac{1}{2} - \frac{2}{\pi^2}\left(\arctan\left[\frac{1}{2}\left(\frac{U}{2} - \frac{2}{U}\right)\right]\right)^2 \\ &= 1 - 2g(U) \end{aligned} \tag{3.59}$$

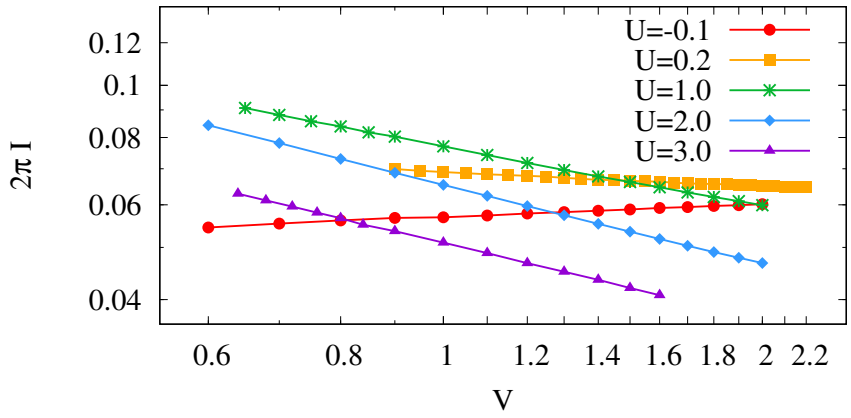

Figure 3.16: Stationary current I as a function of V for $J = 0.1$, for a few selected values of U in log-log coordinates. A log-log scale is used to show the power law behavior of the current at large V/t_B ($I \sim V^{-b}$), and to extract the associated exponent $b(U)$. The values $b(U)$ extracted by these fits are displayed in Fig. 3.17.

This equation again reflects the duality between large and small U, as Eq. (3.53). Some remarkable dual points are $U = 0$ and its twin $U \to \infty$, where $b = 0$. It is worth to mention that duality breaks down in negative domain, there is no U^* such that $b(U) = b(U^*)$ for $U < 0$.

Our study provides the first detailed numerical check of Eq. (3.59). Previously it had only be checked in the vicinity of non-interacting case [86]. For small values of U the exponent b describing the current suppression at large bias has been computed using some functional renormalization group method [86] or with some self-consistent conserving approximation [74].

We fit the current data in log-log coordinates to extract b, and compare the analytical prediction Eq. (3.59). The results of these fits are shown in Fig. 3.17.[4]

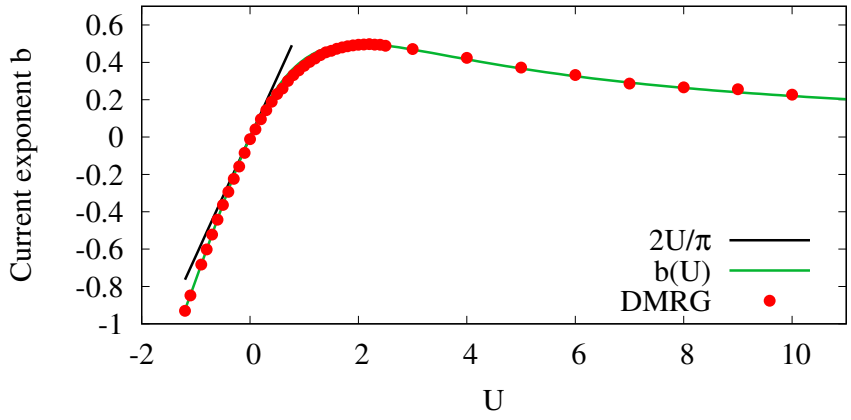

Figure 3.17: Exponent $b(U)$ as a function of the interaction strength U, obtained by fitting the steady current I to $I \sim V^{-b}$, at large V/t_B (see Fig. 3.16). The full (black) line is $b = 2U/\pi$, the result of small-U expansion [86, 74] and green line is Eq. (3.59).

[4]The value $J = 0.1$ appears to offer a good compromise to estimate b in our simulations. Indeed,

Using our convention for the lattice model, the perturbative result of [86] reads $b = 2U/\pi + \mathcal{O}(U^2)$. Our results appear to be slightly below this first order expansion in U. The exponent $b(U)$ should reach a maximum value $b = \frac{1}{2}$ (equivalent to $g = \frac{1}{4}$) at the self-dual point. The maximum value we obtain is $b = 0.494$, which gives an estimate on our precision on this quantity. It is found to be slightly below 0.5. This shows that the precision is quite high, but it also indicates that our procedure slightly underestimates the exponent. This effect is presumably due to the fact that the calculations are performed using a finite J (0.1) and finite bare voltage V (up to $\simeq 2$).

3.5.2 Boundary sine-Gordon model versus IRLM

Without entering into details we give a brief description of the sine-Gordon model with a boundary interaction.

The IRLM [79] admits two field theoretic formulations which are close to, but in general not identical with, the BSG model. Both formulations are obtained using bosonization [see Sec. 3.3]. Their difference originates in the fact that one can first make linear combinations of the fermions in each lead then bosonize, or first bosonize, then make linear combinations of the resulting bosons. The first reformulation leads to an anisotropic Kondo Hamiltonian. As it is done in Sec. 3.3.1, we bosonize the even and odd fermions $\psi_\pm = \frac{\eta_{1,2}}{\sqrt{2\pi}} e^{i\sqrt{4\pi}\phi_{1,2}}$ and then perform the unitary transformation $\mathcal{U} = e^{i\alpha S^z(\phi_1+\phi_2)(0)}$ to eliminate the density-density interaction U_c. In terms of the new bosonic fields $\phi_\pm = \frac{1}{\beta}\left[(\sqrt{4\pi}-\alpha)\phi_{1,2} \mp \alpha\phi_{2,1}\right]$, the Hamiltonian takes the following form

$$H^{(1)}_{\mathrm{IRLM}} = \sum_{a=\pm} H_0(\phi_a) + \frac{J_c}{\sqrt{\pi}}\kappa_+ \left[e^{i\beta\phi_+(0)}S_+ + \mathrm{H.c}\right] \tag{3.60}$$

where $H_0(\phi_a) = \frac{1}{2}\int dx(\partial_x\phi_a)^2$ is the free boson Hamiltonian. The self-dual case is $U_{sd} = \pi$ corresponding to $\beta = \sqrt{2\pi}$, where $\beta^2 = \frac{2}{\pi}(U_c - \pi)^2 + 2\pi$, while the non-interacting case is $U_c = 0$, as well as $U_c = 2\pi$, and therefore $\beta = \sqrt{4\pi}$. Finally, the amplitude J_c is related with amplitudes in the initial field theoretic formulation following [79].

The second reformulation "mixes" the Kondo and the BSG Hamiltonians. After bosonising chiral fermions $\psi_{1,2} = \frac{\eta_{1,2}}{\sqrt{2\pi}} e^{i\sqrt{4\pi}\varphi_{1,2}}$, one forms even and odd bosonic combinations $\phi_1 = \frac{1}{\sqrt{2}}(\varphi_1 + \varphi_2)$ and $\phi_2 = \frac{1}{\sqrt{2}}(\varphi_1 - \varphi_2)$. The Hamiltonian is then transformed under $\mathcal{U} = e^{i\sqrt{2}\alpha S^z\phi_1(0)}$, it yields to a following form

$$H^{(2)}_{\mathrm{IRLM}} = \sum_{a=\pm} H_0(\phi_a) + \frac{\gamma}{\sqrt{2\pi}}\left[V_1(0)O_2(0)S_+ + \mathrm{H.c}\right] \tag{3.61}$$

where $V_{\pm 1} = e^{\pm i\beta_1\phi_1}$, $O_2 = \kappa_1 V_2 + \kappa_2 V_{-2}$, $V_{\pm 2} = e^{\pm i\sqrt{2\pi}\phi_2}$, $\kappa_a = \eta\eta_a$. We have set $\beta_1 = \sqrt{2\pi} - \alpha\sqrt{2}$, so $\beta^2 = \beta_1^2 + 2\pi$. Note that there is a special value of the interaction term $U_{sd} = \pi$ where a remarkable simplification occurs. The exponent of the vertex operator $V_{\pm 1}$ vanishes ($\alpha = \sqrt{\pi}$) and therefore the even bosonic field ϕ_1 decouples from the impurity.

---

we need a small J to be in the scaling regime, but the time to reach the steady regime (which increases when J decreases) should also not become too large compared to L/v_F.

We now turn to the BSG model

$$H_{\rm BSG} = H_0(\phi_2) + \gamma' \cos\beta\phi_2(0) \tag{3.62}$$

with Hamiltonian chosen in such a way that the tunneling term has the same dimension $g \equiv \frac{\beta^2}{8\pi}$ as in the IRLM, and $\gamma' \propto \gamma$. The voltage in the BSG, as well as in the IRLM, can be introduced by $e^{\pm i\beta\phi_2} \to e^{\pm i(\beta\phi_2 + Vt)}$. The difference between (3.61) and (3.62) is obvious: the second Hamiltonian involves only two vertex operators, and does not contain any spin. For more details see Ref. [10, 87, 88]

3.5.3 Full counting statistics in the BSG model

We start by defining the *full counting statistics* [89, 58]. The generating function Z of the charge cumulants is:

$$Z(\chi, t) \;\; = \;\; \left\langle e^{i\chi\hat{Q}(t)} e^{-i\chi\hat{Q}(0)} \right\rangle, \tag{3.63}$$

where χ is a "counting" parameter, and $\hat{Q}(t)$ is the operator measuring the total charge in the (say) right lead at time t. To study transport in the present quantum impurity setup, it is convenient to define another function:

$$F(\chi) \;\; = \lim_{t\to\infty} \;\; \frac{1}{t} \ln Z(\chi, t). \tag{3.64}$$

From this, one can in particular get the mean steady current, $I = \frac{1}{i}\partial F/\partial\chi$. Anticipating on Chap. 4, one can also get the current *noise* (or *shot noise*) S, which is proportional to the rate at which the second cumulant of the transfered charge grows with t:

$$S = -\frac{\partial^2 F}{\partial \chi^2}. \tag{3.65}$$

The results for the BSG model out-of-equilibrium take the form of an exact analytical expression for $F(\chi)$ [84, 56]. After some simple manipulations to allow for a change of the wire geometry (adapted for a description of the IRLM), the result can be written as large-V expansion

$$F^{\rm BSG}(\chi) = \frac{Vg}{\pi} \sum_{n=1}^{\infty} \frac{a_n(g)}{n} \left(\frac{V}{T_{\rm BSG}}\right)^{2n(g-1)} \left(e^{i\chi n/2} - 1\right), \tag{3.66}$$

or, as low-bias expansion

$$F^{\rm BSG}(\chi) = \frac{V}{2\pi} i\chi + \frac{V}{\pi} \sum_{n=1}^{\infty} \frac{a_n(1/g)}{n} \times$$
$$\times \left(\frac{V}{T_{\rm BSG}}\right)^{2n(-1+1/g)} \left(e^{-i\chi n/2g} - 1\right). \tag{3.67}$$

Here $g = \frac{\beta^2}{8\pi}$ and the coefficients $a_n(g)$ are given by

$$a_n(g) = (-1)^{n+1} \frac{\Gamma(3/2)\Gamma(ng)}{\Gamma(n)\Gamma(n(g-1)+3/2)} \tag{3.68}$$

and $T_{\rm BSG} \propto (\gamma')^{1/1-g}$. Notice that these expansions exhibit a duality $g \to 1/g$ [90], up to a redefinition of the counting field χ. From these functions one can obtain expressions for the mean current $I(V)$ in the form of some series, as given the next section [Eqs. (3.69), (3.70)].

3.5.4 The BSG 'template'

Using Eqs. (3.67) and (3.66) we find two series expansion for the current for the BSG model:

$$I^{\mathrm{BSG}} = \frac{Vg}{2\pi}\sum_{n=1}^{\infty} a_n(g)\left(\frac{V}{T_{\mathrm{BSG}}}\right)^{2n(g-1)} \tag{3.69}$$

at large V (the UV regime) and

$$I^{\mathrm{BSG}} = \frac{V}{2\pi} - \frac{V}{2\pi g}\sum_{n=1}^{\infty} a_n(1/g)\left(\frac{V}{T_{\mathrm{BSG}}}\right)^{2n(-1+1/g)}. \tag{3.70}$$

at small V (the IR regime). It will be convenient in what follows to use a scaling form

$$I^{\mathrm{BSG}} = T_{\mathrm{BSG}}\,\vartheta(V/T_{\mathrm{BSG}}) \tag{3.71}$$

where, e.g. at large x, the function ϑ is defined by

$$\vartheta(x) = \frac{xg}{2\pi}\sum_{n=1}^{\infty} a_n(g)x^{2n(g-1)}. \tag{3.72}$$

In the particular, for $g = 1/2$ the series can easily be summed to give

$$2\pi I^{\mathrm{BSG}}(g=1/2) = \frac{T_{\mathrm{BSG}}}{2}\arctan\frac{2V}{T_{\mathrm{BSG}}} \tag{3.73}$$

This matches the known result for the RLM [8] (IRLM at $U = 0$)

$$2\pi I^{\mathrm{RLM}}(U=0) = 4t_B\arctan\frac{V}{4t_B} \tag{3.74}$$

after the identification $t_B = \frac{T_{\mathrm{BSG}}}{8}$. Meanwhile, recall that if the perturbation in BSG is normalized precisely as $2\gamma\frac{\cos\beta\phi}{\sqrt{2\pi}}$ (so $\gamma' = \sqrt{\frac{2}{\pi}}\gamma$) we have the relation

$$T_{\mathrm{BSG}} = c_{\mathrm{BSG}}\gamma^{1/1-g} \tag{3.75}$$

with

$$c_{\mathrm{BSG}} = \frac{2}{g}\left(\frac{\sqrt{2}\sin\pi g\Gamma(1-g)}{\sqrt{\pi}}\right)^{1/1-g}. \tag{3.76}$$

So when $g = \frac{1}{2}$, $T_{\mathrm{BSG}} = 8\gamma^2$, and $t_B = \gamma^2$.

We now propose to compare the numerically measured I-V curves of the IRLM in the scaling limit with the analytical expressions for the BSG current. In order to do this, we need to fix the parameter g of the BSG model so that both the BSG model and the IRLM have a power law decay of the current in the UV with the same exponent. In Sec. 3.5.6 we will then compare the IV curves globally, from low to high bias voltage.

The exponent b of the IRLM is known exactly as a function of U [9], as explained in Sec. 3.3. In order to get the same large-bias exponent in the IRLM and in the BSG model, the parameter g of the BSG model has to become a function of U (or U_c): $2g = 1 - b$ with b given by Eq. (3.55).

We are then left with the parameter T_{BSG} that we determine simply by a best fitting procedure. Note that, since the mapping on BSG is a priori not supposed to work exactly , there is no reason to use equation (3.76). We know by dimensional analysis that $T_{\mathrm{BSG}} \propto \gamma^{1/1-g}$, but it is interesting to see what a dependency of the prefactor on g looks like, compared with (3.76).

3.5.5 Large bias and c_{IRLM}

Since the dimensionless prefactor c_{BSG} [Eq. (3.76)] appearing in the definition of the energy scale T_{BSG} is *a priori* not a universal quantity, it is natural to redefine it for the IRLM in order to analyze non-equilibrium characteristics of two models. In the Eq. (3.69) we set the prefactor of T_{BSG} to be a *free* parameter and numerically adjust (fit) it so that the analytical curve for a given g coincides with the tDMRG data at large bias (large V and/or small J):

$$T_{\mathrm{B}} = c_{\mathrm{IRLM}} J^{1/(1-g)}, \tag{3.77}$$

where J appears with the same *exponent* as γ in T_{BSG} [Eq. (3.75)]. A related discussion on the prefactor of $J^{1/(1-g)}$ in the definition of t_B can be found in a recent work by Camacho, Schmitteckert and Carr [78].

In our case we adjust data numerically (fit) so that the analytical curve for a given g coincides with the tDMRG data at large bias:

$$I^{\mathrm{IRLM}}_{\mathrm{numerics}} \simeq T_{\mathrm{B}}\, \vartheta\left(\frac{V}{T_{\mathrm{B}}}\right) \quad \text{when } V/T_{\mathrm{B}} \gg 1 \tag{3.78}$$

[with ϑ defined in Eq. (3.72)]. To be explicit, we rescale the numerics with the scale defined Eq. (3.77), and adjust c_{IRLM}

The result of this procedure is a function $c_{\mathrm{IRLM}}(b)$, displayed in the top panel of Fig. 3.18, or equivalently $c_{\mathrm{IRLM}}(U)$, plotted in bottom panel of Fig. 3.18. For comparison we also plotted c_{BSG} given in Eq. (3.76).

In case of the free-fermion problem, i.e. $g = 1/2$ and $b = 0$, the two models are equivalent and the theoretical value of crossover parameters is $c_{\mathrm{BSG}} = 8 = c_{\mathrm{IRLM}}$, in a good agreement with tDMRG data. Since the IRLM at $U_c = \pi$ maps exactly onto the BSG model [2], we expect to have $c_{\mathrm{IRLM}} = c_{\mathrm{BSG}}$ at this point too. The numerics give $c_{\mathrm{IRLM}} \approx 4.66$ while the exact result is $c_{\mathrm{BSG}} = 8 \cdot \Gamma(3/4)^{4/3}/\pi^{2/3} \approx 4.89$. This 5% discrepancy is might be due to finite J effect, *i.e.* deviation from the scaling regime.

In Fig. 3.18 we also marked the value of c_{IRLM} at the self-dual point which was found by Boulat *et al.* [2]. Their estimate for T_{B} at this point is $2.7c_0(J)^{1/(1-g)} \approx 4.65$ (with $g = 1/4$ and $c_0 = \frac{4\sqrt{\pi}\Gamma(2/3)}{\Gamma(1/6)}$). This value is in a good agreement with our data but differs by about 5% from the exact value. Away from the free-fermion point and away from the self-dual point, the curves for c_{IRLM} and c_{BSG} are significantly different. c_{IRLM} monotonically decreases with increasing U but c_{BSG} grows past the self-dual point at $U = 2$. As already mentioned, the prefactors c_{IRLM} or c_{BSG} are not expected to be universal quantities, so the fact that $c_{\mathrm{IRLM}} \neq c_{\mathrm{BSG}}$ is not surprising at all. We will now go further and investigate if the expression of Eq. (3.78) could also be used, at least approximately, for *finite* V/T_{B}.

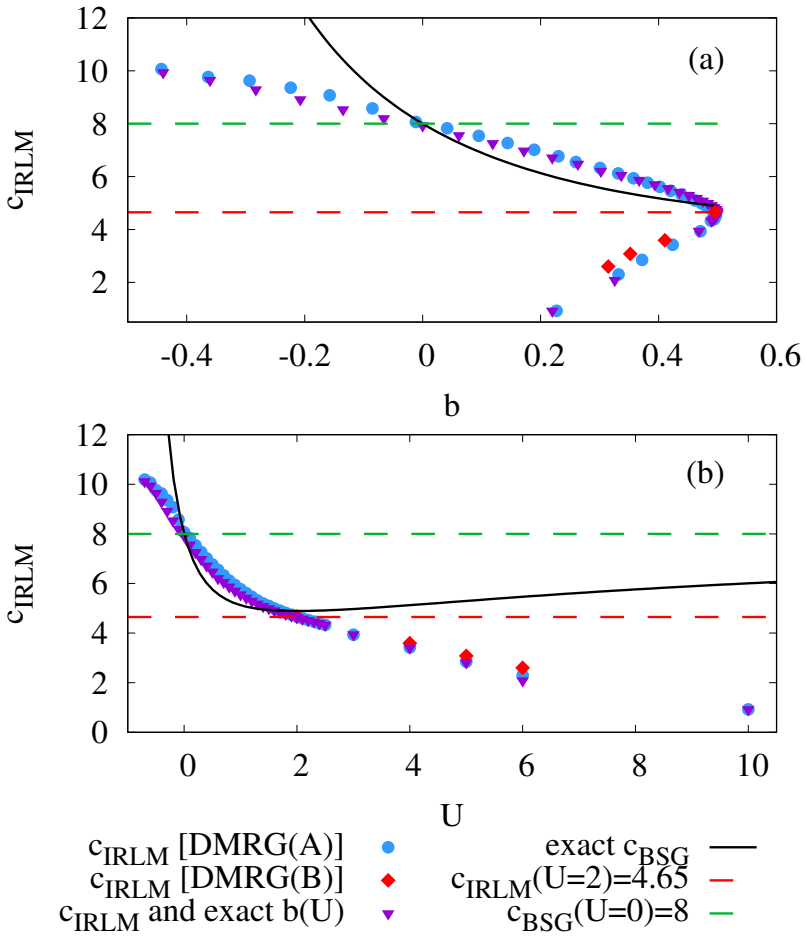

Figure 3.18: Panel (a): coefficient c_{IRLM} as a function of b. Blue dots and red diamonds: the exponent $b(U)$ and the coefficient $c_{\mathrm{IRLM}}(b)$ are obtained from the tDMRG numerics only for protocols A and B. Purple triangles: the exponent $b(U)$ is taken from Eq. (3.59), (3.51), and $c_{\mathrm{IRLM}}(b)$ was extracted from the tDMRG data. Black line: $c_{\mathrm{BSG}}(b)$ given by Eq. (3.76). Red line: $2.7\frac{4\sqrt{\pi}\Gamma(2/3)}{\Gamma(1/6)} \approx 4.65$ (see [2]) which corresponds to $U = 2$ (self-dual point). Green line: $c_{\mathrm{BSG}}(b = 0) = 8$ at $U = 0$. Panel (b): same but with U on the horizontal axis.

3.5.6 Finite bias

Once the large-bias part of the current curve of the IRLM is adjusted to match that of the BSG (through c_{IRLM}, as discussed above), we can see if the agreement persists at lower bias. The results of this analysis are displayed in Figs. 3.19 and 3.20.

We observe a relatively good collapse, on a single master curve, of the data sets corresponding to different J (for a given U). This indicates that the lattice model is indeed close to the scaling regime, characterized by a single energy scale t_B. For $U = 2.0$ this has already been observed by Boulat *et al.* [2], but thanks to longer simulations and larger systems, the present data have some higher precision and we could extend the $I-V$ curves to larger values of V/t_B (beyond 100) and for several values of U from -0.1 to 3.

The fact that the current *decreases* with V at large bias for $U > 0$, called negative differential conductance, is a remarkable phenomenon due to the interaction (for $U \leq 0$ the current is monotonically increasing), and has already been discussed

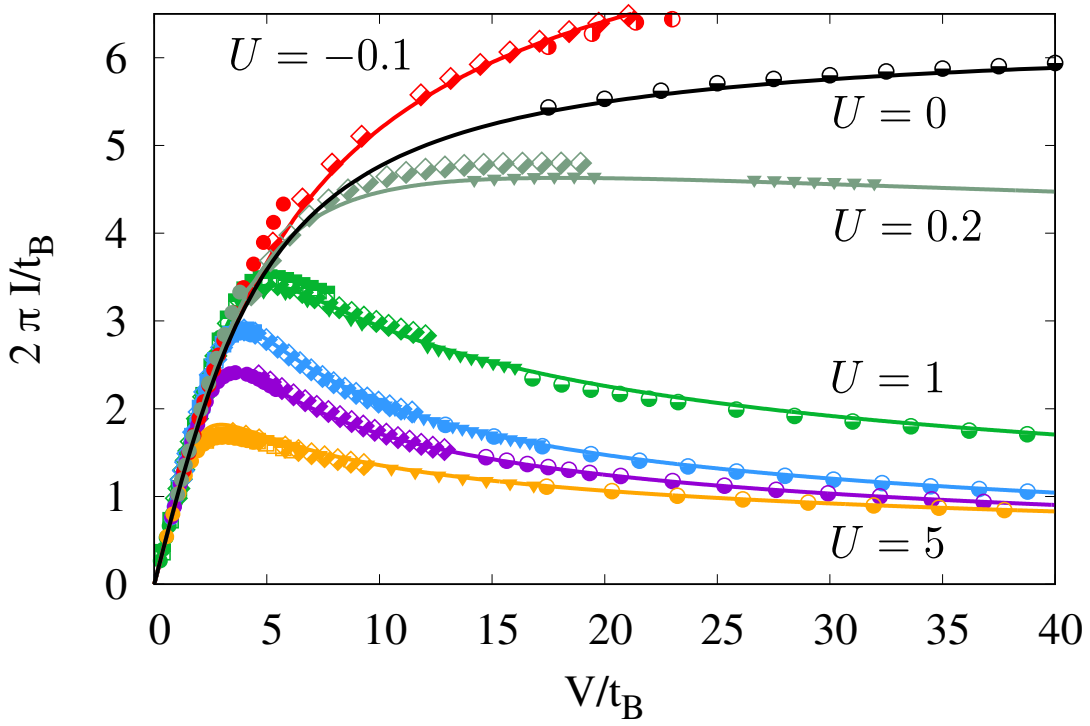

Figure 3.19: Rescaled current I/t_B as a function of the rescaled bias V/t_B, for different values of U. The colors label the values of U, while the symbol shapes encode J (see the legend of Fig. 3.20 for details). From top to bottom $U = -0.1$, 0, 0.2, 1, 2, 3 and 5 For a given U, the results obtained for different values of J approximately collapse onto a single curve, as expected in the scaling regime. The magenta line is the theoretical result for the self-dual point [2]. The numerical data for $U = 2.0$ appear to be in very good agreement with this theoretical curve. The black line is the exact result for $U = 0$ (Eq. 3.19). The Kondo temperature is defined as $t_B = J^{1/(1-g(U))}$ where the exponent $g(U)$ is determined from the behavior of I at large V/t_B (see text and Fig. 3.17).

in [2].

The remarkable and somewhat unexpected fact is that for $U \lesssim 3$ the BSG function Eqs. (3.72)-(3.78) is a very good approximation of the IRLM current, even when V/t_B is of order 1. While the agreement is excellent at the self-dual point (as it should, and as already noted in Refs. [2, 8, 91]) the BSG function continues to describe well the IRLM current *away* from $U = 0$ and $U = 2$. In fact, for $U \lesssim 3$, the deviation between BSG and IRLM is of the same order of magnitude as the numerical precision.[5] For $U > 3$ we start to observe some small discrepancy between the numerical data and the BSG curves, close to the maximum of the current curve, when V/t_B is close to 1 (data not shown, we refer the reader to Ref. [10]). The precise magnitude of this discrepancy is however difficult to estimate since it is in this part of the I-V curve the data sets associated with different values of J do not overlap perfectly. Also, as can be seen in the insets of Fig. 3.21, the data points tend to get closer to the BSG curve when J is decreased. So, the actual difference

[5]The latter precision can be estimated by looking at the approximate collapse of data obtained for different values of J (but same V/t_B). The spread indicates to which extend the lattice model is close to the scaling limit. See also Appendix B.

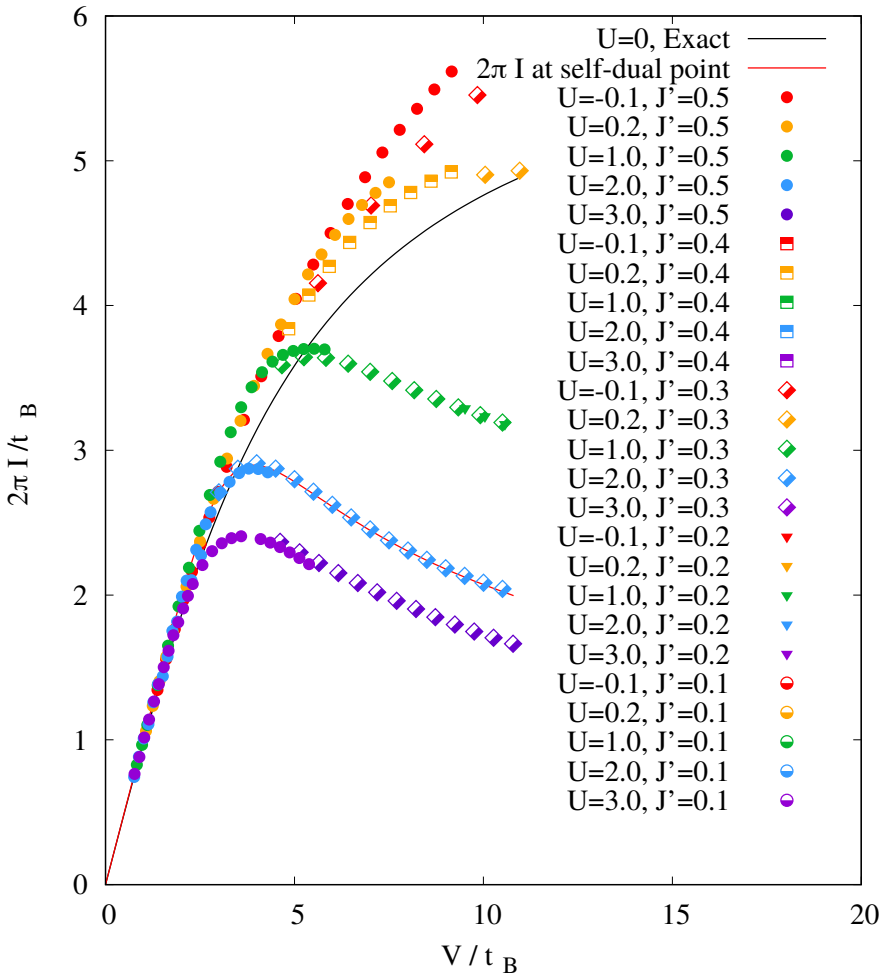

Figure 3.20: Same as Fig. 3.19 (rescaled current I/t_B as a function of the rescaled bias V/t_B), with a zoom on the low bias region. The colors label the values of U, while the symbol shapes encode J (see the legend).

between the IRLM in the scaling regime and the BSG model might be smaller than what Fig. 3.21 indicates.

As commented earlier, it is clear that one can expect a certain amount of similarity between the currents in the BSG and the IRLM. Thanks to our matching of the exponents and the t_B scale (Sec. 3.5.5), the leading terms must agree by construction. On the other hand - as illustrated in Fig. 3.22 which shows (dotted or dashed lines) the leading term, or the sum of the first 2 or 10 terms in this expansion - it is clear that the leading term only is not enough to reproduce the IRLM data close to the maximum of the current. The agreement between the I-V curves for the two models in this region remains mysterious. What probably happens is that the first few terms in the UV expansion are very close to each other.

Although the BSG and IRLM model look different (Sec. 3.5.2), could it be that the two models out-of-equilibrium are in fact the same universality class? To address this point we turn to a comparison of the IR behavior of the two model, and we will answer negatively to this question.

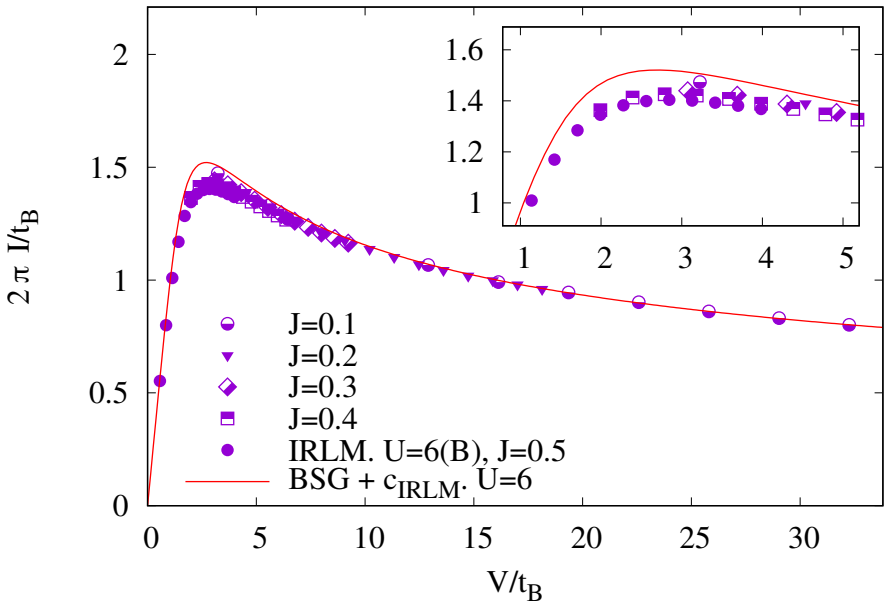

Figure 3.21: Rescaled I-V curves for $U = 6$ measured using the protocol (A). The symbol shapes encode J. As expected the agreement between the IRLM numerics and the BSG is excellent for $U = 2$ (self-dual point, Fig.3.19), but it is also very good for $U = 1, 3, 5, 6$ where the models are *a priori not* equivalent. In the inset we see, that data points tend to get be closer to the BSG curve when J is decreased. So the small discrepancy could originate from finite J effects, as in the free $U = 0$ case Fig.3.7 .

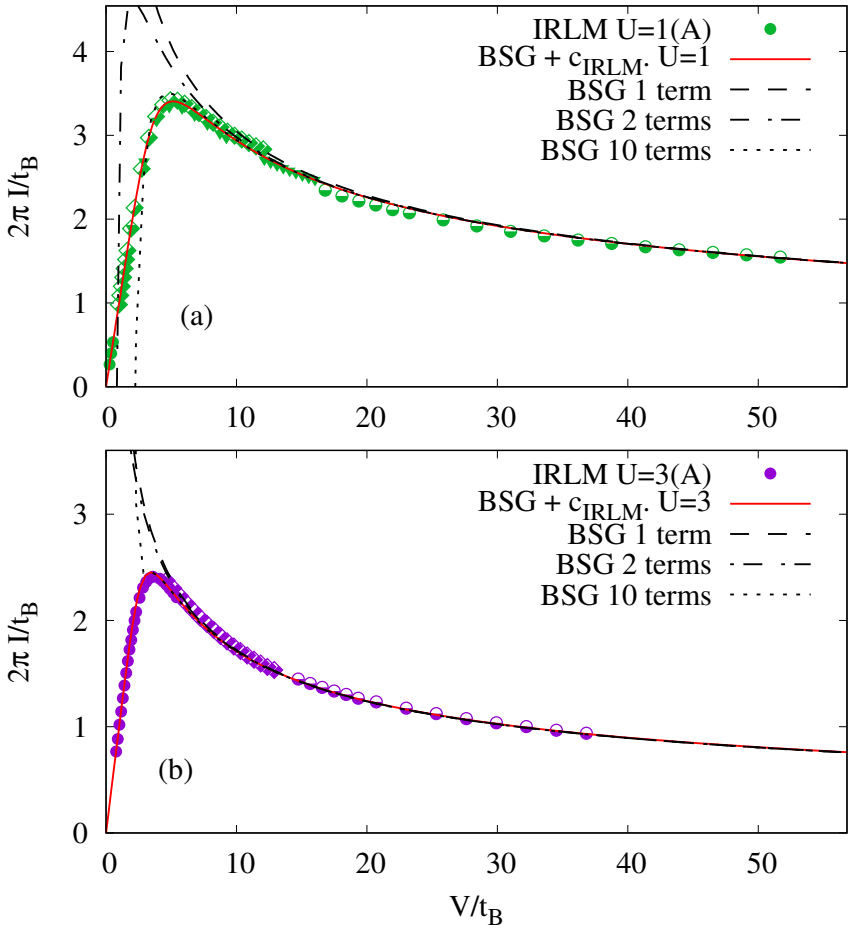

Figure 3.22: Rescaled I-V curves for the quench protocol (A) compared to different truncation orders in the large bias expansion of the function ϑ [Eq. (3.72)] (black dashed and dotted lines). It appears that one or two terms in the expansion is not enough to capture the behavior of the IRLM down to the crossover regime where V/T_B is of order one. On the other hand, with 10 terms the truncated expansion matches the IRLM data relatively well from the UV down to the maximum of the current curve.

Chapter 4

Shot noise and backscattered current

In the previous chapter we found a striking agreement between the transport characteristics of two distinct models, namely the IRLM and the BSG model. Surprisingly, the tDMRG numerics for the rescaled current in the IRLM are well described by $I-V$ curves of the BSG model for a large range of bias V and interaction strength U, which was not expected away from the two points where the two models can be exactly mapped onto each other.

In the present chapter we pursue the analysis to shed light on this agreement. A natural quantity to explore further the charge transport properties is the current noise S.[1] This analysis will reveal that the two models behave differently in the IR regime.

4.1 Second charge cumulant, current noise and current fluctuations

As we will see, the current noise can be defined as the time derivative of the variance of the charge in the (say) right lead, or as the zero-frequency limit of the current-current correlation function.

We consider the second cumulant C_2 of the charge in one lead. It is defined by

$$C_2(t) = \langle\psi(t)|\,\hat{Q}^2\,|\psi(t)\rangle - \langle\psi(t)|\,\hat{Q}\,|\psi(t)\rangle^2 \tag{4.1}$$

where $\hat{Q} = \sum_{r=1}^{N/2} c_r^\dagger c_r$ is the operator measuring the total charge in the right lead.[2] A typical time evolution of this cumulant is presented in Fig. 4.1. Since $C_2(t)$ grows linearly with time, a quantity of interest is the rate

$$S = \frac{d}{dt}C_2(t), \tag{4.2}$$

which goes to a constant in the steady regime. The long time limit of S is a measure of the current *noise* [71].

[1] Do not confuse with an entanglement entropy S_{vN}.

[2] We set the "electric" charge e of each fermion to $e = 1$.

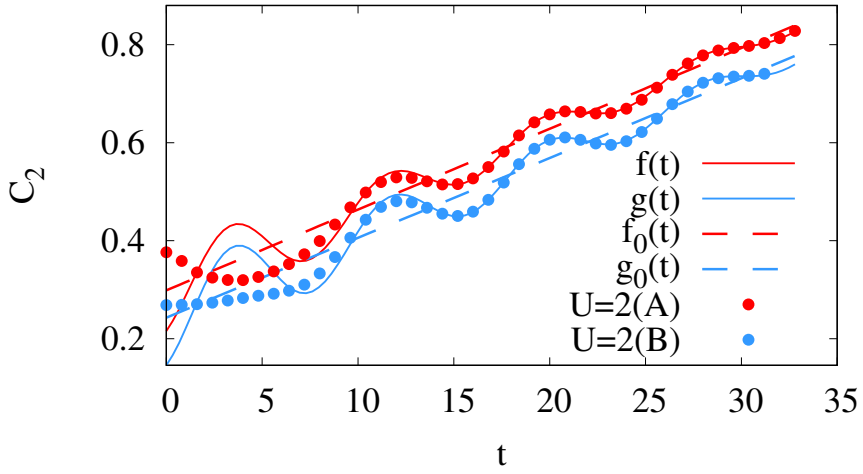

Figure 4.1: Time evolution of the second charge cumulant C_2, computed using tDMRG. The red circles represent C_2 for the IRLM with the protocol A, and the blue circles represent the results for protocol B. Parameters of the model: $U = 2$ (self-dual point), $J = 0.2$ and $V = 1.6$. The data can be interpreted as a linear growth superposed with (slowly damped) oscillations. The fitting functions are $f(t) = 0.3 + 0.0165t + 0.09\cos(0.764t + 3.6)\exp(-0.06t)$ and $g(t) = 0.24 + 0.0163t + 0.11\cos(0.765t + 3.5)\exp(-0.05t)$. The dashed lines represent $f_0(t)$ and $g_0(t)$, the fitting functions associated to the protocols A and B. The exact value of $\frac{d}{dt}C_2$ for the IRLM at the self-dual point is 0.0165 [see Sec. 4.3]. While the two initial states (protocols A and B) give different results for $C_2(t)$, the rate of growth is essentially the same at sufficiently long times.

Alternatively, the noise can be defined as the zero-frequency limit

$$S = \int_{-\infty}^{\infty} \langle \Delta\hat{I}(0)\Delta\hat{I}(\tau)\rangle d\tau$$

of the current-current correlation function, where we have defined $\Delta\hat{I}(t) = \hat{I}(t) - \langle\hat{I}(t)\rangle$. It should be noted that, in experiments, the shot noise is actually measured through these time-dependent fluctuations of the current [see for instance [92]].

To establish the relation between the rate of the second charge cumulant [Eq. (4.2)] and the zero-frequency limit of the current-current correlation, one starts by writing the charge in right lead as an integral of the current

$$\hat{Q}(t) = \hat{Q}_0 + \int_0^t \hat{I}(\tau)d\tau. \tag{4.3}$$

where $\hat{Q}_0$ is the charge operator at time $t = 0$. The expectation value $\langle\hat{Q}_0\rangle$ contains an information about the initial wave function $|\psi(t = 0)\rangle$, which depends on the initial parameters, like the hopping to the impurity J_0 and the density-density interaction strength U_0.

If we denote by $\mathrm{var}[\hat{X}]$ the variance $\langle\hat{X}^2\rangle - \langle\hat{X}\rangle^2$ of an operator $\hat{X}$, we have

$$\begin{aligned} C_2(t) &= \mathrm{var}[\hat{Q}(t)] = \mathrm{var}\left[\hat{Q}_0 + \int_0^t \hat{I}(\tau)d\tau\right] \\ &= \mathrm{var}\left[\hat{Q}(0) + \int_0^t \Delta\hat{I}(\tau)d\tau\right]. \end{aligned} \tag{4.4}$$

Expanding Eq. (4.4) we get

$$\begin{aligned} C_2(t) &= \mathrm{var}[\hat{Q}(0)] + \int_0^t \int_0^t \langle \Delta\hat{I}(\tau)\Delta\hat{I}(\tau')\rangle d\tau d\tau' \\ &\quad + \int_0^t \langle \Delta\hat{I}(\tau)\hat{Q}(0)\rangle + \int_0^t \langle \hat{Q}(0)\Delta\hat{I}(\tau)\rangle. \end{aligned} \tag{4.5}$$

We then make the assumption that the correlator $\langle \hat{Q}(0)\hat{\Delta}I(\tau)\rangle$ decays sufficiently quickly with τ, such that the last line in the equation above is small compared to t when $t \to \infty$. We further assume that $\langle \Delta\hat{I}(\tau)\Delta\hat{I}(\tau')\rangle$ decays sufficiently quickly with the time difference $|\tau - \tau'|$. In the limit $t \to \infty$, the double integral will be dominated by τ and τ' of the order of $\mathcal{O}(t)$, and $|\tau - \tau'| \ll t$. At sufficient large times the system is in a (quasi) steady state and two-time correlations only depend on the time difference $\tau - \tau'$. It follows that the double integral can be approximated by $t\int_{-t}^{t}\langle \Delta\hat{I}(0)\Delta\hat{I}(\tau)\rangle d\tau$, or even by $t\int_{-\infty}^{\infty}\langle \Delta\hat{I}(0)\Delta\hat{I}(\tau)\rangle d\tau$. We finally get

$$C_2(t) \underset{t\to\infty}{\simeq} t\int_{-\infty}^{\infty}\langle \Delta\hat{I}(0)\Delta\hat{I}(\tau)\rangle d\tau \tag{4.6}$$

and

$$S \simeq \int_{-\infty}^{\infty}\langle \Delta\hat{I}(0)\Delta\hat{I}(\tau)\rangle d\tau. \tag{4.7}$$

In the following sections the current noise S will be studied numerically using its relation with $C_2(t)$, and its dependence on the bias will be compared with that of the BSG model.

4.2 Numerical calculations of the noise

The current noise has already been investigated numerically using tDMRG for the RLM ($U = 0$) [4] as well as at the self-dual point [93, 94]. In Refs. [4, 93] S was formulated in terms of the zero-frequency limit of the current-current correlations. In Refs. [94, 95], using a modified time-evolution with an explicit counting field χ, the cumulant generating function F was estimated numerically and the noise was extracted as the coefficient of the χ^2 term. More recently, a functional renormalization group approach [96] was used to compute the noise in the IRLM [97],[3] especially in the regime of small U.

Instead, here we compute the current noise numerically using the relation between S and the fluctuations of the charge, as described by Eq. (4.2). At any time, $C_2(t)$ is obtained by summing all the connected density-density correlations $G(r, r')$ in the right lead:

$$C_2(t) = \sum_{r,r'\geq 1} G(r, r') \tag{4.8}$$

$$\begin{aligned} G(r, r') &= \langle\psi(t)|c_r^\dagger c_r c_{r'}^\dagger c_{r'}|\psi(t)\rangle \\ &\quad -\langle\psi(t)|c_r^\dagger c_r|\psi(t)\rangle\langle\psi(t)|c_{r'}^\dagger c_{r'}|\psi(t)\rangle. \end{aligned} \tag{4.9}$$

[3]The functional renormalization group approach has also been employed to study other aspects of the out-of-equilibrium physics of the IRLM [see for instance Refs. [86, 98, 99]].

We fit the bare data for $C_2(t)$ with the function

$$f(t) = f_0 + St + A\cos(Vt/2 + \phi)\exp(-\delta t).$$

The time window for the fit has to be larger than the transient time needed to reach a (quasi) steady regime, i.e. we need to reach a regime where $C_2(t)$ shows a clear linear growth (as illustrated in Fig. 4.1). In practice, with the parameters J and V we considered, we typically have to fit the data starting from $t \gtrsim 10$. The noise S is then obtained as the coefficient of the linear growth of $C_2(t)$. Some bare results for $S(V, J)$ (at $U = 0$) are displayed in Fig. 4.2.

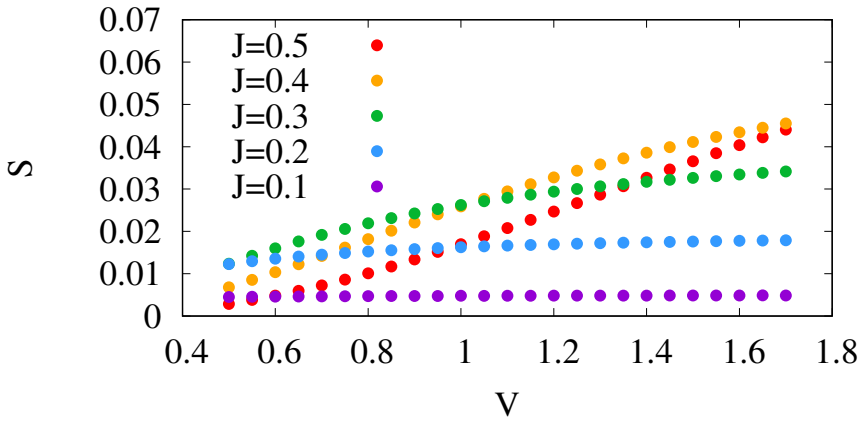

Figure 4.2: Shot noise S as a function of bare bias V for $U = 0$ and different values of J. S is obtained as the rate at which $C_2(t)$ grows with time. The low-bias regime is hard to access since the period $T = 4\pi/V$ of the oscillations (visible in Fig. 4.1) become large at small V, and can exceed the simulation time.

4.3 Noise in the free and self-dual cases

On the analytical side, one can get the current noise S as the second derivative of function F [Eq. (3.64)] describing the full counting statistics, and which is the generating function for all the charge cumulants:

$$S(V) = -\frac{\partial^2 F}{\partial \chi^2}_{|\chi=0}. \tag{4.10}$$

For the IRLM the function F is known exactly at the free and self-dual points, where the model maps onto the BSG model. There, one can use Eqs. (3.66) and (3.67). In the UV regime (large V/T_B) the result reads:

$$S(V) = \frac{Vg}{4\pi}\sum_{n=1}^{\infty} n a_n(g)\left(\frac{V}{T_{\mathrm{BSG}}}\right)^{2n(g-1)}. \tag{4.11}$$

The expression above describes exactly the IRLM for two values of the anomalous dimension g: $g = 1/2$ for the free fermion model and $g = 1/4$ for the self-dual case. This implies that, at large V (but still in the scaling regime), $S|_{U=0} \sim V^0$ and $S|_{U=2} \sim V^{-1/2}$. Comparing with Eq. (3.19) ($U = 0$) and Eq. (3.57) (self-dual), we

see that the noise behaves in the same manner as the current in the large V regime. The noise can also be expressed as low-V expansion:

$$S(V) = \frac{V}{4\pi g^2} \sum_{n=1}^{\infty} n a_n(1/g) \left(\frac{V}{T_{\mathrm{BSG}}} \right)^{2n(-1+1/g)} . \tag{4.12}$$

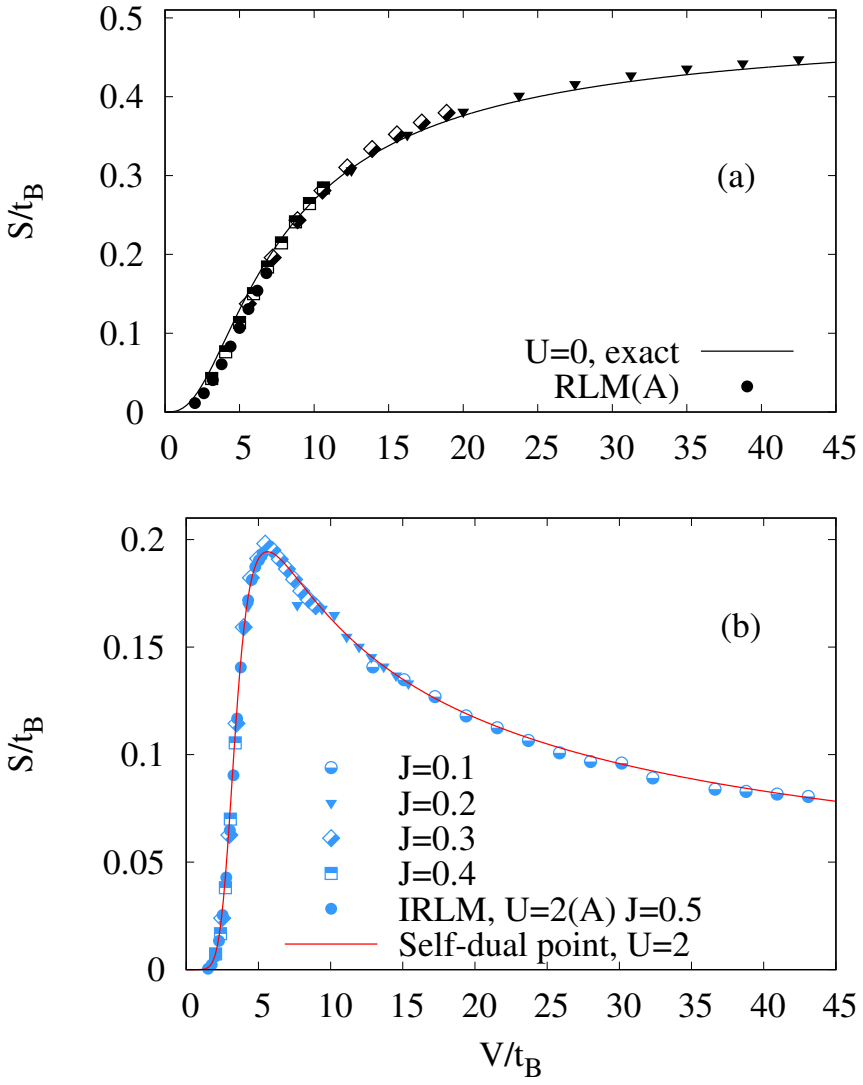

Figure 4.3: Rescaled current noise S/t_B versus V/t_B for $U = 0$(a) and $U = 2$(b). The symbol shape encodes J. The full line for $U = 0$ corresponds to Eq. (4.14). For $U = 2$ the full lines correspond to Eq. (4.12) with $g = 1/4$. Data obtained with the protocol A. These plots are constructed without any adjustable parameters: c_{IRLM} is determined from the large-bias analysis of the current [Fig. 3.18] (and for $U = 2$ the Kondo temperature prefactor c_{IRLM} agrees with its analytical prediction [see Sec. 3.5.5]).

In the free case the exact expression for the transmission probability $\mathcal{T}(\epsilon)$ [Eq. (3.3)] has been obtained by solving the the Schrödinger for the single-particle problem, and this $\mathcal{T}(\epsilon)$ has been used to calculate the current [see Sec. 3.2]. In fact it is easy

to see that $\mathcal{T}(\epsilon)$ also determines the current noise. Consider a single incoming mode and independent scattering events, where each fermion has a probability $\mathcal{T}$ to be transmitted and $1-\mathcal{T}$ to be reflected. For each incoming particle the transmitted charge is e with probability $\mathcal{T}$ and 0 with probability $1-\mathcal{T}$. As for the *square* of the transmitted charge, it is e^2 with probability $\mathcal{T}$ and 0 with probability $1-\mathcal{T}$. We get that the variance of the transmitted charge is $\mathcal{T}e^2-(\mathcal{T}e)^2 = e^2\mathcal{T}(1-\mathcal{T})$ per incoming particle. Integrating over all the incoming modes, labeled by their energy ϵ, this argument gives an expression for the noise of the Landauer-Büttiker type (with $e=1$):

$$\begin{aligned} S(V) &= \int_{-V/2}^{V/2} \frac{d\epsilon}{2\pi} \mathcal{T}(\epsilon)\left(1-\mathcal{T}(\epsilon)\right) \\ &= \int_{-V/2}^{V/2} \frac{d\epsilon}{2\pi} \mathcal{T}(\epsilon)\mathcal{R}(\epsilon) \end{aligned} \tag{4.13}$$

Using the explicit expression of $\mathcal{T}(\epsilon)$ [Eq. (3.3)], in the scaling limit $J \to 0$ one obtains a simple expression for the current noise:

$$\frac{S(V)}{t_B} = \frac{1}{\pi}\left[\arctan\left(\frac{V}{4t_B}\right) - \frac{V/4t_B}{1+(V/4t_B)^2}\right], \tag{4.14}$$

where $t_B = J^2$. The same result could be obtained by re-summing the series of Eq. (4.11) or (4.12) with $g=1/2$ and $T_B = 8J^2$. Importantly, this formula shows that, in the scaling regime, S/t_B is a function of the rescaled bias, V/t_B. Our numerics will show that this is also true away from the two exactly solvable points.

The numerical results, rescaled using t_B, are displayed in Fig. 4.3 for $U=0$ and $U=2$. The data are in good agreement with the exact formula (shown as full lines). Importantly we also observe a relatively good collapse of the rescaled curves obtained for different values of J. As we already observed with the current, this confirms that the simulations are carried out here in a regime which is sufficiently close to the scaling limit, even though some small corrections to scaling can be seen (the collapse is not perfect).

4.4 Noise for arbitrary U

In the Sec. 3.5 we found that $I-V$ curves of the IRLM and the BSG model are surprisingly similar. What is remarkable is the fact that the $I-V$ curves are almost identical after only two adjustments, namely UV exponent b of the steady current ($I \sim V^{-b}$) and energy scale prefactor c_{IRLM}. One can a priori not expect that these two parameters are enough to fix the whole non-equilibrium characteristics, for instance the current *and* shot-noise curves. For this reason we will now compare the $S-V$ curves of the two models for arbitrary values of the interaction U, once the constant c_{IRLM} has been fixed from the *current* data in the UV. In the following there is therefore no adjustable parameter left, since $g(U)$ (or equivalently $b(U)$) is given by Eq. (3.59) and c_{IRLM} has been obtained in Fig. 3.18. The results are displayed in Figs. 4.4 and 4.5.

As for free fermion and self-dual cases, we find a good collapse of the rescaled tDMRG data obtained for hopping amplitudes J from 0.3 to 0.5 (Fig. 4.4). The

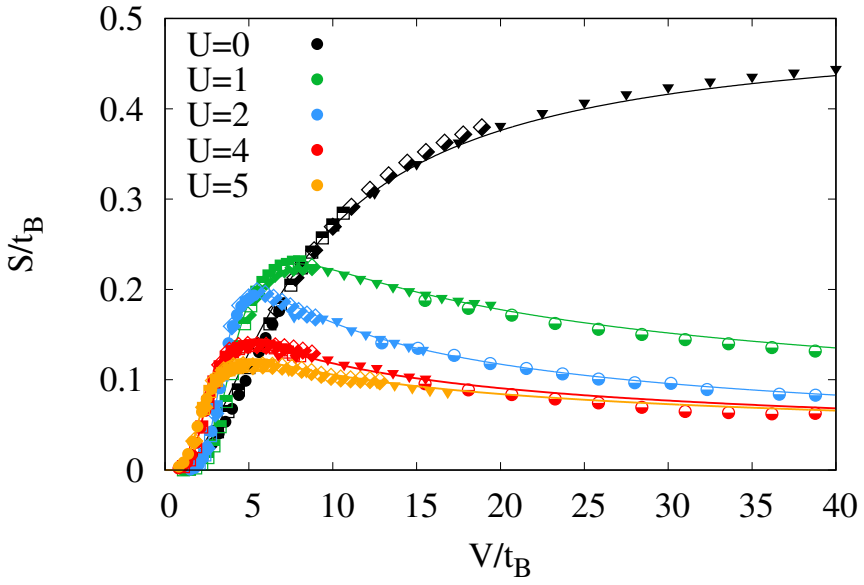

Figure 4.4: Rescaled charge second cumulant rate S/t_B versus V/t_B for $U = 0, 1, 2, 4$ and 5. The symbol shape encodes J[see the legend of Fig. 3.20]. The full line for $U = 0$ corresponds to Eq. (4.14) For other values of U the full lines correspond to BSG $S - V$ curves Eqs. (4.12)-(4.11). Data for $U \leq 2$ obtained with the protocol A and for $U > 2$, respectively, with the protocol B. These plots are constructed *without* any adjustable parameters: to obtain $t_B = J^{\frac{2}{1+b}}$, $b(U)$ is taken from Eqs. (3.59) and the adjustment factor c_{IRLM} of the analytical BSG curves is determined from the large bias analysis of the current.

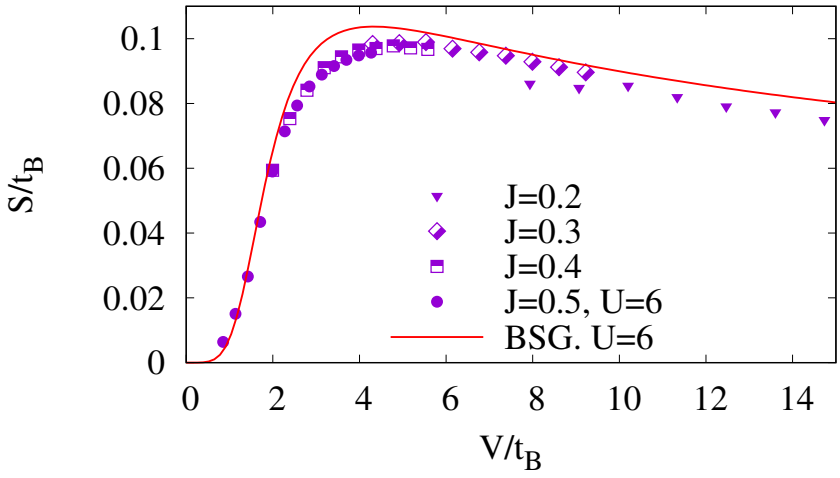

Figure 4.5: Rescaled noise S as a function of the rescaled voltage V for the large value of interaction $U = 6$ and several values of J. This case shows some discrepancy between the BSG model result (full line) and numerics for the IRLM.

rescaled data collapse relatively well onto a single curve, which is an indication that the tDMRG numerics are sufficiently precise and that the parameters J and V we use put the model close enough to its scaling limit. We nevertheless have a lower

numerical precision at large U and large V/t_B, which is particularly clear in Fig. 4.5 where the collapse is far from perfect.

To analyze these data, we compare the shot noise S/t_B of the IRLM with that of the BSG (full lines in Figs. 4.4 - 4.5). We stress again that there is no new adjustable parameter, since for each U and J we use the scale t_B (and $c_{\rm IRLM}$) determined from the analysis of the current. As already mentioned, at $U = 2$ (bottom panel in Fig. 4.3) the data are in excellent agreement with the theoretical prediction for the BSG [Eqs. (4.11) and (4.12)], as it should. But quite remarkably, the agreement remains good away from the two points where the models are known to be exactly equivalent, from $U = 0$ up to $U \lesssim 3$ or 4. At large V the shot noise slowly reaches a constant in the free case : $\lim_{V/t_B\to\infty} S^{U=0} = e^2/2 = 1/2$ in our units where the elementary charge is set to $e = 1$. We note that a small perturbation in U leads to a strong change in the UV, since the current noise decays to zero in the UV for $U > 0$.

In the BSG model the current and the shot noise decay with the same exponent b in the UV. The observed agreement between the noise of the IRLM and that of the BSG model implies that it should also be the case for the IRLM. The fact that the current and the shot noise decay with the same exponent in the UV has already been noticed in [97] for small (perturbative) U, but we observed it here to hold at large U too.

For very large values of U, above $\simeq 3$ or 4, some difference between the current noise of the IRLM and that of the BSG model starts to appear. As an example, we present data for $U = 6$ in Fig. 4.5, to focus on the discrepancy between the two models. The $S - V$ curve of the BSG gives a good approximation to that of the IRLM for low rescaled voltage but it starts to differ in the crossover domain $V/t_B \simeq 2 \cdots 6$. Also, it could be that aforementioned finite-J effects contributes to mismatch between $S - V$ curves of the BSG and the IRLM.

Are the BSG and the IRLM transport characteristics like $I-V$ or $S-V$ the same or not? The steady current curves are almost identical for different interaction U, despite the fact that the theories are expected to be equivalent *only* at the self-dual $U = 2$ and free $U = 0$ points. As we just discussed, the noise $S - V$ curves for two theories are also in a good agreement, and the difference starts to be visible only for large values $U \gtrsim 3 \sim 4$ of the interaction.

At this stage we cannot yet definitely answer this question. Now we turn to the next step, which is a detailed comparison of the transport properties of the two models in the IR, that is in the limit of small voltage.

4.5 Small voltage and backscattered current

Although we found that the $I - V$ and $S - V$ curves of the two models seem to agree in a large range of voltage and interaction strength U, at least within our numerical accuracy, we will show below that some clear difference can be observed if one carries out a detailed camparison of their IR behavior.

In fact, the low-bias expansion of the steady current in the IRLM has been computed exactly up to order $\mathcal{O}(V^6)$ by Freton and Boulat [9]. They computed the backscattered current:

$$I_{\rm BS} = \frac{V}{2\pi} - I, \tag{4.15}$$

i.e. the difference between the current I and the value $V/2\pi$ of the current in absence of impurity. Their result reads [4]:

$$\frac{I_{\rm BS}}{T_B} = \frac{XV^3}{48g^2T_B^3}\Bigg[1+\frac{3\kappa_4 * 3V^2\left(X^2-10X+5\right)}{40gT_B^2} + \frac{3V^2\left(X^2+1\right)}{40g^2T_B^2}\Bigg] + \mathcal{O}\left(\left(\frac{V}{T_B}\right)^7\right), \tag{4.16}$$

where $X = 4g-1$. The coefficients κ_{2n} are couplings appearing in the IR expansion of a dual description of the anisotropic Kondo Hamiltonian of Eq. (3.45) [9, 47, 100, 101] and they reads

$$\kappa_{2n} = \frac{(g/\pi)^{n-1}}{(n-\frac{1}{2})n!}\frac{\Gamma\left(\frac{2n-1}{2(1-g)}\right)}{\Gamma\left(\frac{g(2n-1)}{2(1-g)}\right)}\left[\frac{\Gamma\left(\frac{g}{2(1-g)}\right)}{\Gamma\left(\frac{1}{2(1-g)}\right)}\right]^{2n-1}. \tag{4.17}$$

This shows that for the IRLM the backscattered current $I_{\rm BS}$ vanishes as V^3 at low bias. On the other hand, the backscattered current in the BSG model can be read of Eq. (3.70), and its leading term has an exponent which varies continuously with g: $I_{\rm BS}^{\rm BSG}/T_{\rm BSG} \sim (V/T_{\rm BSG})^{-1+2/g}$. So, for sufficiently low V the numerical data for the IRLM should show a V^3 behavior and should depart from the BSG results if $U \neq 0$ and if $U \neq 2$. At the self-dual point the coefficient of the V^3 and V^5 terms vanish and the leading term in $I_{\rm BS}$ becomes $\mathcal{O}(V^7)$ [9], in agreement with the BSG result at $g = 1/4$. All these features can be understood with an IR perturbative analysis similar to the one sketched in section V of Ref. [10]. The data plotted in Fig. 4.6 illustrate the low-bias behaviors of $I_{\rm BS}$ at the self-dual point (bottom panel), and at a more generic value of U (upper panel). We see that, in fact, the currents in the BSG and IRLM have different analytical behaviors in this region - and that these properties are in agreement with the field theoretic analysis [10]. While the low-bias data at $U = 1$ follow the perturbative prediction for the IRLM as it should, it is striking that $I_{\rm BS}$ then joins the BSG curve for $V/T_B \gtrsim 0.5$, although there is a priori no reason why it should do so at such intermediate bias.

4.5.1 Charge of the carriers

In the free case the quasiparticles that tunnel through the dot are simply the fermions themselves, and their charge is $e = 1$. But, in presence of interactions, more complex collective many-body excitations should be considered, one may ask what is the charge of the quasiparticles responsible for the charge transport. The information from the mean current and from the noise can be combined to get some information about the charge of the quasiparticles. Consider for simplicity a single mode coming to the dot, associated to quasiparticles with some (unknown) charge q. This charge may *a priori* depend on the system parameters, like U and voltage. In a simplified picture of independent particles, the mean current is $\langle I\rangle = c\mathcal{T}q$, where c is some

[4] For the Freton-Boulat expansion to match the exact formula at the free-Fermion point, we had to change the sign of the third term in their formula.

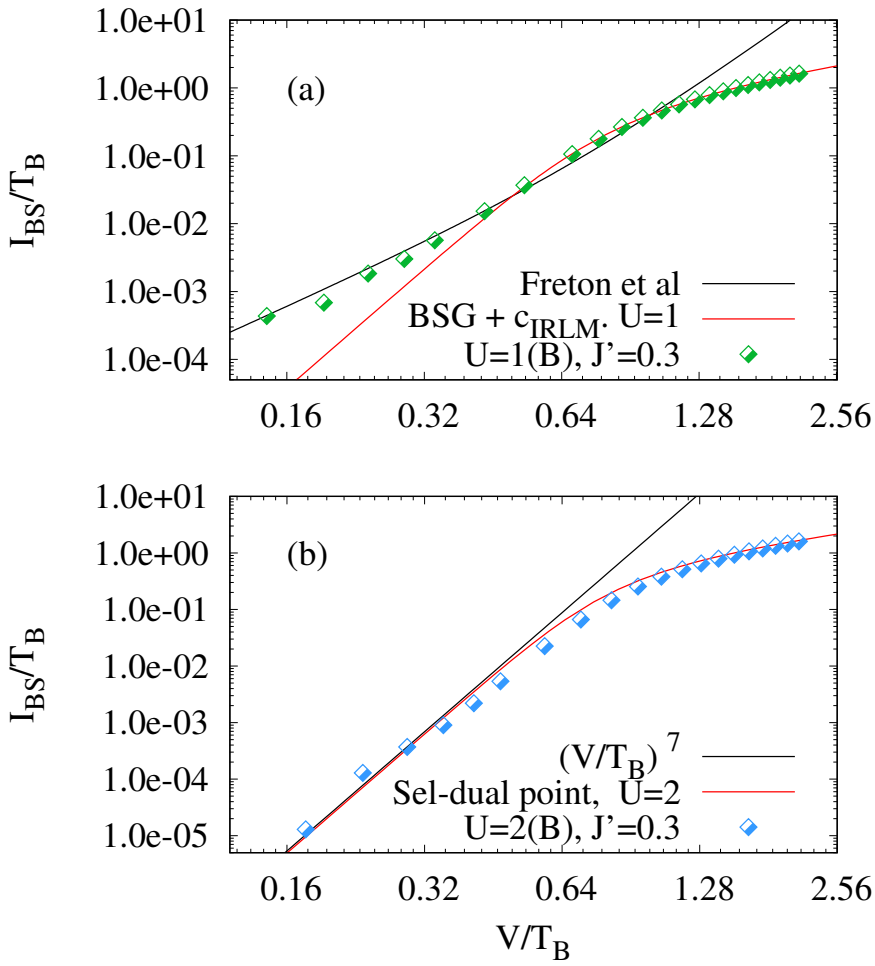

Figure 4.6: Panel (a): Rescaled backscattered current $I_{\rm BS}/T_{\rm B} = V/(2\pi T_{\rm B}) - I/T_{\rm B}$ as a function of $V/T_{\rm B}$ at $U = 1$. Panel (b): same for $U = 2$ (self-dual point). For $U = 2$, $I_{\rm BS}$ vanishes as V^7 at low V, as expected from the equivalence with the BSG at the self-dual point. For $U = 1$, the data are consistent with V^3, as expected for the IRLM away from the self-dual point [9]. Data obtained using the protocol B.

unknown constant describing the rate at which quasiparticles reach the dot, and $\mathcal{T}$ is their (also unknown) transmission probability. We also get the mean of the square of the current, $\langle I^2\rangle = c\mathcal{T}q^2$, and the current noise (variance of the current) $S = c\mathcal{T}q^2(1-\mathcal{T})$. As for the backscattered current, is equal to: $\langle I_{\rm BS}\rangle = c(1-\mathcal{T})q$. The mean current is not enough to determine q, but one may consider the following ratios, called Fano factors: $S/I_{\rm BS} = \mathcal{T}q$ or $S/I = (1-\mathcal{T})q$. We see that, in the limit where $\mathcal{T}$ is close to one (as in the IR regime), the effective charge q is given by the so-called backscattering Fano factor, $S/I_{\rm BS} \simeq q_{\rm IR}$. On the other hand, in a regime where $\mathcal{T}$ is close to zero, as realized in the UV for $U > 0$, the charge is given by $\lim_{V/T_B\to\infty} S/I \simeq q_{\rm UV}$.

Using the exact results for the current and the noise in the BSG model, one can find the charge of the carriers in the IR limit by looking at the backscattering Fano factor. The result is a continuously varying function of the parameter g:

$$q_{\rm IR}^{\rm BSG} = \frac{e}{2g}. \tag{4.18}$$

As we will see, the situation is different for the IRLM.

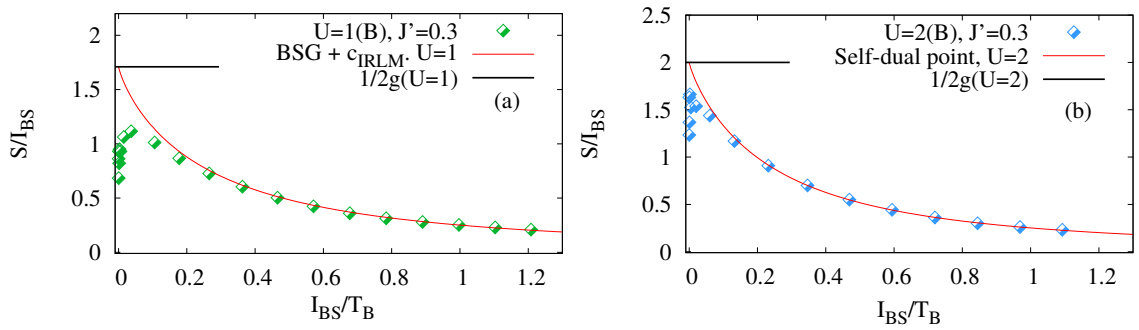

Figure 4.7: $S/I_{\rm BS}$ versus rescaled bias V/T_B for $U = 1$(a) and 2(b). This ratio is also known as the backscattering Fano factor. Here we used an MPS truncation parameter $\delta = 10^{-10}$ and a total simulation time $T = 90$ to increase a precision of numerics in the small V regime.

We checked numerically that for the IRLM we get the correct charge e at large voltage. Since both S and $I_{\rm BS}$ become very small at low bias (almost perfect transmission), it is difficult to achieve a good numerical precision for these two quantities and for their ratio (backscattering Fano factor). The Fano factor $S/I_{\rm BS}$ is plotted in Fig. 4.7 for $U = 1$ (upper panel) and $U = 2$ (lower panel). Since errors (due to finite-time simulations) are the largest at low bias, one may discard the lowest-bias data points. In that case, the Fano factor extrapolates to some value close to $\frac{e}{2g} = 2e$ [see Fig. 4.8] at the exactly solvable point $g = \frac{1}{4}$ ($U = 2$), in agreement with the arguments given in Sec V of Ref. [10]. It should be noted that a very similar result has been obtained in Ref. [93]. The data for the other values of the interaction are, unfortunately, harder to analyze, but they are compatible with a charge e for all other values of the interaction (as expected from the field theoretic discussion [10]). At $U = 1$ for instance (top panel of Fig. 4.7), the low-bias limit of the Fano factor is indeed close to 1 (that is e) if we again allow ourselves to discard the two points at low $I_{\rm BS}$, where we know – by comparison with the $U = 2$ case – that the error should be the largest.

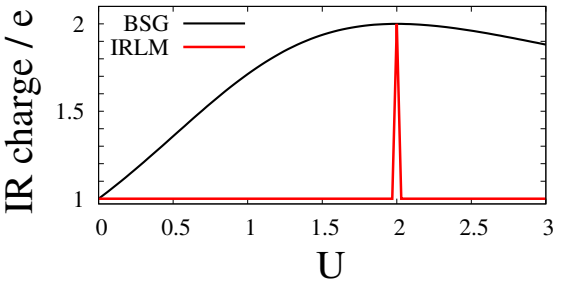

Figure 4.8: Charge of quasiparticles dominating transport in the deep IR for the IRLM and BSG model. The charge for the IRLM differs from e only at the self-dual point where it becomes equal to $2e$, whereas the charge for the BSG model is a nontrivial function of the interaction parameter U [Eq. (4.18)].

Chapter 5

Entanglement entropy

In the previous chapters, we performed extensive state-of-the-art computer simulations of the dynamics with tDMRG, which is based on a MPS description of the wave functions (see Chap.A). We obtained accurate results concerning the current-voltage and noise-voltage curves of the IRLM in a wide range parameter of the model (voltage bias, interaction strength, tunneling amplitude to the dot, etc.). While the current and the noise are essentially a local observable and a two-point correlations, it is also interesting to study some non-local quantity which is the bipartite (von Neumann) *entanglement* entropy.

The entanglement entropy of a subsystem reads

$$S_{vN} = -\sum_i p_i \log p_i, \tag{5.1}$$

where the p_i are the eigenvalues of the reduced density matrix of the subsystem. In the present chapter we provide some numerical results studies concerning entanglement entropies associated to left-right partitions of the system, in the IRLM out-of-equilibrium. We will in particular analyze its space dependence (how it varies with the position of the left-right cut) and as well as its time dependence. These results have been published in [8].

5.1 Entanglement entropy

We denote by $S_{vN}(t, R+\frac{1}{2})$ the entanglement entropy of the set A of sites located to the left of site R, that is $A = \{-N/2, \ldots, R\}$, as depicted in Fig. 5.1. When no position is specified, $S_{vN}(t)$ refers to the entanglement entropy $S_{vN}(t, -\frac{1}{2})$ of the entire left (or right) lead. Fig. 5.2 illustrates how the entanglement profile evolves in time. The most striking feature is the rapid growth of the entanglement entropy, which turns out to be linear in time for a given R inside the "light cone", see Fig. 5.2. This linear growth of the entropy is well known in the situations where some steady current is flowing through a quantum impurity (or defect). One can in particular mention the analogous case of a weak

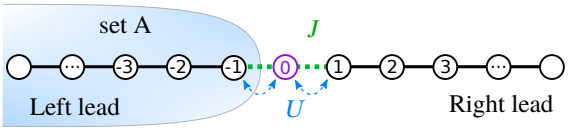

Figure 5.1: Here we chose subsystem A to be the whole left lead.

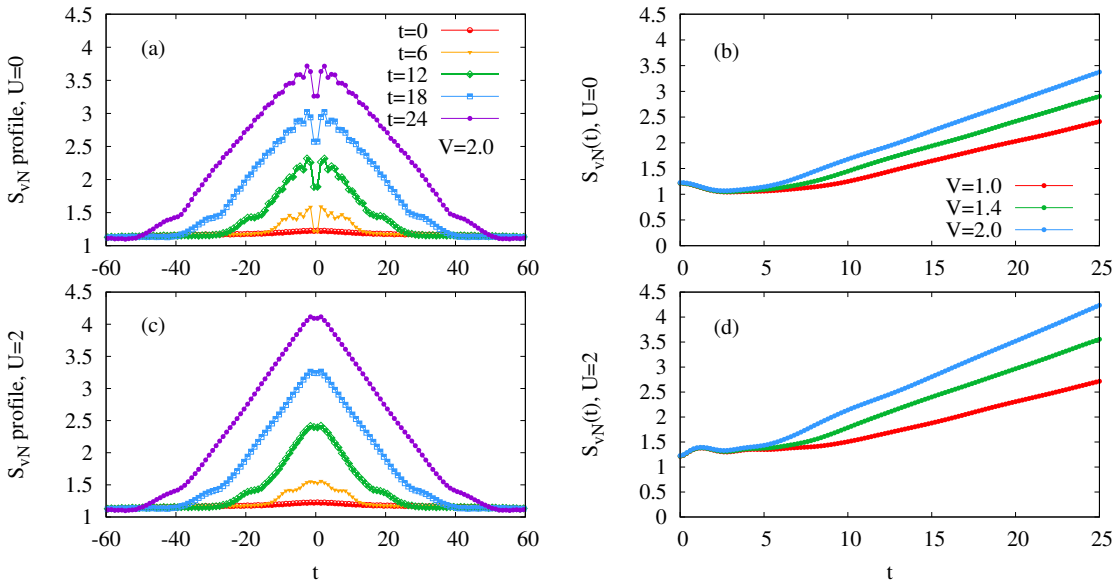

Figure 5.2: Panels (a) and (c): evolution of the entanglement entropy $S_{vN}(r,t)$ profile for $U = 0$ and for $U = 2$. Parameters of the model: $J = 0.3$, $V = 2.0$, $N = 254$, as in the Fig. 2.3.
Panels (b) and (d): evolution of the entanglement entropy $S_{vN}(t)$ of the left lead, see Fig. 5.1. Entanglement rate grows with the voltage. The interacting model ($U = 2$) is more entangled compared to the free case ($U = 0$) for the same parameters. It therefore requires more computational resources.

bond connecting two free leads, studied in detailed in Ref. [102]. In such situations, a quantity of interest is the entropy *rate*, defined as $\alpha = \frac{d}{dt} S_{vN}(t)$.

Since the computational cost of MPS-based methods grows exponentially with the amount of bipartite entanglement entropy in the system, this linear entropy growth severely limits the longest times we can reach in the simulations. This should be contrasted, for instance, with the slower logarithmic growth of the entropy in the case where the two leads are connected to the dot in the *absence of any bias* [81, 82]. A logarithmic growth is in fact generic for local quenches in critical one dimensional systems [30, 102, 103]. The entropy growth is also logarithmic in the case of an XXZ spin chain ($|\Delta| < 1$), with a translation invariant Hamiltonian, which is set in a current-carrying state using some domain-wall initial condition (equivalent to some non-zero bias) [104, 69, 105, 106].

The physical origin of the finite rate α is easy to understand in a noninteracting and semiclassical picture. Each incoming particle at energy ϵ has a finite probability $\mathcal{T}(\epsilon)$ to be transmitted to the other side of the dot, and a probability $\mathcal{R}(\epsilon) = 1 - \mathcal{T}(\epsilon)$ to be reflected (more details in Sec. 5.3). After such a scattering event the wave packet of the particle is split in two parts, one on each side of the dot, propagating in opposite directions. In other words, the state of this particle is a quantum superposition of two terms, one in which the particle is in the left lead, and another one where the particle is in the right lead. So, each such event contributes by an amount $\delta S = -\mathcal{T}(\epsilon) \ln \mathcal{T}(\epsilon) - \mathcal{R}(\epsilon) \ln \mathcal{R}(\epsilon)$ to the entanglement entropy between the two leads. In presence of a finite steady current there is finite charge transmitted per unit of time, and hence a linear growth of the entropy $S(t) \sim \alpha t$ (except if $\mathcal{R}(\epsilon) = 0$, as for $J = 1$). In such a picture the entanglement is directly related to

quantum fluctuations of the transmitted charge, present as soon as $\mathcal{T}(\epsilon)$ is different from 1 and from 0, and this is nothing but a manifestation of the relation between entanglement and charge fluctuations in free particle systems [107, 108, 109]. In contrast, if $U \neq 0$, the entanglement growth is *a priori* not directly related to the partial transfer of the particles. We will indeed see in Sec. 5.4 that one can be in a situation where steady current I goes to zero while the entropy rate α stays finite.

The semiclassical description at $U = 0$ can also be used to understand qualitatively the triangular shape of the entropy profile. Indeed, in the limit where the bias V is small compared to the bandwidth, the energy dispersion is linear and therefore all the relevant excitations propagate at the same group velocity $\partial\epsilon/\partial k = \pm v_F = \pm 2$. In that case, the degrees of freedom which contribute to the entanglement entropy form a "train" of left-moving wave packets with momenta centered around $-k_F$, and another train with right-moving wave packets centered at $+k_F$.[1] The important point is that each left-moving particle is entangled with one right-moving partner, located on the other side of the dot, at the same distance. When performing a partition of the chain at a given time t and at a given position R, the entanglement entropy that is predicted by the semiclassical description simply depends on the number of entangled pairs which are separated by the partition. It is then straightforward to see that this leads to a *triangular* entropy profile, with a spatial extension ranging from $R = -v_F t$ to $R = +v_F t$, and a height equal to αt, with the rate α given in the Sec. 5.3. Although this classical picture with noninteracting particles does not apply to the $U \neq 0$ case, the numerical simulations show that the triangular shape of the entropy profiles is a robust feature, at least far enough from the dot. The integrability of the IRLM implies that, in some sense, a particle picture is still applicable, even in presence of strong interactions. This property was crucial to derive the results in Refs. [2, 84, 56], and it might be related to the triangular profile obsreved here. Closer to the dot, the profile is however not triangular, and this will be analyzed in Sec. 5.2.

It should finally be noted that this linear entropy growth is what makes this type of simulation difficult, since it forces the matrix dimensions in the MPS representation of the wave function to grow exponentially with time. Some more details on this point can be found in Sec. B.

5.2 Stationary entropy profile

Several works have shown that, in Kondo-like problems, the entanglement entropy can be used to identify some spatial region of size $\xi \sim t_B^{-1}$ around the impurity (sometimes called Kondo 'cloud'). See for instance Refs. [82, 110] concerning the IRLM, and Ref. [65] for a more general review. While these studies investigated the entanglement in the ground state of the model, here we instead look at the entropy profile in some nonequilibrium steady state, in presence of a finite current.

Our results are summarized in Fig. 5.3. As discussed in Sec. 5.1, the global shape of the profile is approximately triangular, with some maximum value that grows as

[1] The average spacing λ between the packets is proportional to the inverse of their momentum width: $\lambda = 2\pi(\Delta k)^{-1}$. The momentum width is related to the energy width, $v_F \Delta k = \Delta\epsilon$, and this energy width is nothing but the bias, $\Delta\epsilon = V$. We thus have $v_F \Delta k = V$. The number of incident particles per unit of time is thus $v_F/\lambda = V/(2\pi)$, and this is consistent with the small V limit of the current given in Eq. 3.19. Note that the actual distribution is in fact Poissonian.

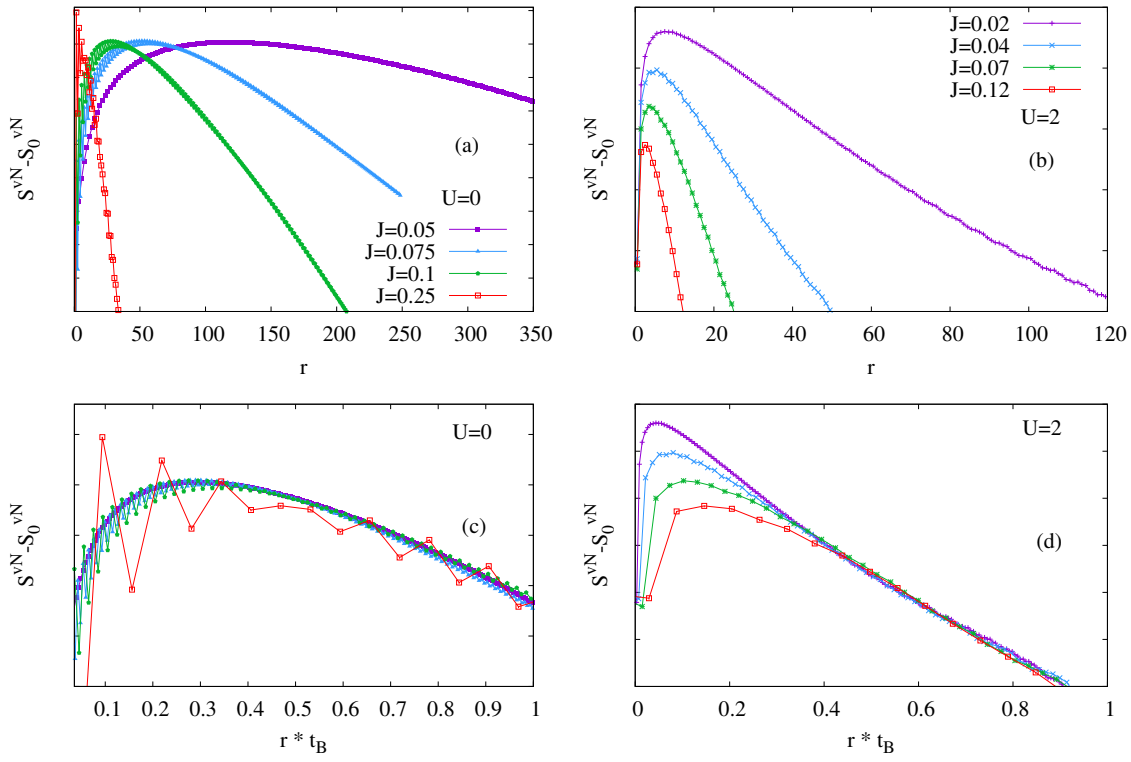

Figure 5.3: Panels (a) and (c): entanglement entropy profiles for $U = 0$, plotted as a function of the bare distance r and the rescaled distance r/ξ with $\xi = t_B^{-1}$ and $t_B = J^2$. Some constant value S_0^{vN} has been subtracted from *each* profile, to allow the data to (approximately) fall onto a single time-independent curve. We only show here the right part of the profile ($r > 0$), the other side ($r < 0$) being symmetric. In $U = 0$ cases the rescaled bias is V/t_B=8 and therefore values for $V(J)$: $V(0.25) = 0.5, V(0.1) = 0.08, V(0.075) = 0.045, V(0.05) = 0.02$ with ratio $t_B^{-1}(0.05) : t_B^{-1}(0.075) : t_B^{-1}(0.1) : t_B^{-1}(0.25) = 25 : 4 : 2.25 : 1$. This ratio means that the largest ($J = 0.05$) entropy "cloud" is 25 times greater than the smallest ($J = 0.25$), even so, rescaled clouds collapse onto a single curve. System size is $N = 6000$ and time is $t = 1200$.
Panels (b) and (d): entanglement profile for $U = 2$ plotted as a function of r and r/ξ with $t_B = J^{4/3}$ and the rescaled bias is $V/t_B = 17.1$. Values for $V(J)$: $V(0.12) = 1.0$, $V(0.07) = 0.5$, $V(0.04) = 0.25$, $V(0.02) = 0.1$ with ratio $t_B^{-1}(0.02) : t_B^{-1}(0.04) : t_B^{-1}(0.07) : t_B^{-1}(1.2) = 10 : 4 : 2 : 1$. System size is $N = 402$ and $t = 60$.

αt with a rate $\alpha \sim \mathcal{O}(t_B)$. In order to analyze more precisely the long time limit of the profiles, we subtract the value of the maximum of each profile.

When plotted as a function of the rescaled distance r/ξ, with $\xi = t_B^{-1}$, the data for $U = 0$ corresponding to different values of J (but same V/t_B) collapse onto a single curve, at least approximately. At distances from the dot which are large compared to ξ, the curve is linear. In this region the collapse is a consequence of the fact that the entropy rate α, and thus the slope of the profile, scales as t_B. However, the curve shows a nontrivial structure for distances from the dot that are of the order of ξ, with some rounded maximum. We interpret this as some signature of the more complex correlations taking place in a nonequilibrium Kondo 'cloud' of size

t_B^{-1}.

The situation at $U = 2$, displayed in Fig. 5.3(b),(d) is more intriguing. The use of the rescaled distance $r \cdot t_B$ still allows the data associated to different J (and thus different t_B) to collapse on a straight line for distances that are sufficiently large. But since the entanglement entropy is just a linear function of the distance to the dot when r is sufficiently large, this collapse only reflects the fact that the slope of the entropy profile is proportional to t_B (which we know already, since the entropy rate scales as t_B and the Fermi velocity is equal to 2). Closer to the dot, there is however no clear convergence for $r \cdot t_B \lesssim 0.4$. More precisely, the distance $r_{\max}$ at which the entropy profiles reaches a maximum clearly grows when J goes to zero, but at some rate which is slower than t_B^{-1}. So, from the present data at $U = 2$ (and $V/t_B = 17.1$), there is no clear evidence of some Kondo-like spatial structure of size $\sim t_B^{-1}$ in the stationary entropy profiles, as observed in the free case. It could however be that some longer times are required to achieve some profile collapse in this regime. Some further systematic investigations, as a function of U and V and J, would be required to elucidate this point.

5.3 Entropy rate for $U = 0$

In analogy with the Landauer approach for the current and the shot noise, the stationary entropy rate α can be obtained analytically. Since each incident particle at energy ϵ has a probability $\mathcal{T}(\epsilon)$ to be transmitted throw the quantum dot, it contributes to the entropy by an amount $\delta S = -\mathcal{T}(\epsilon)\ln\mathcal{T}(\epsilon) - \mathcal{R}(\epsilon)\ln\mathcal{R}(\epsilon)$ (its wave packet is split into a reflected part and a transmitted part) and we get:

$$\alpha = -\frac{1}{2\pi}\int_{-V/2}^{V/2} d\epsilon \left[\mathcal{T}(\epsilon)\ln\mathcal{T}(\epsilon) + \mathcal{R}(\epsilon)\ln\mathcal{R}(\epsilon)\right]. \tag{5.2}$$

The result above is checked numerically against numerical solution of dynamics for the free fermion problem in a next section.

In the scaling regime J is small, the energy ϵ is small (because the bias V is small), but the ratio ϵ/J^2 is of order one. In this limit the transmission coefficient Eq. (3.3) becomes:

$$\mathcal{T}(x) = \frac{1}{1+x^2} \tag{5.3}$$

where $x = \epsilon/(2t_B)$ and $t_B = J^2$. With a change of variable the entropy rate Eq. (5.2) can be expressed as:

$$\begin{aligned}\alpha(v) &= \frac{2t_B}{2\pi}\int_{-v/4}^{v/4} dx \left(\frac{1}{1+x^2}\ln(1+x^2)\right. \\ &\quad \left. + \frac{x^2}{1+x^2}\ln\left(\frac{1+x^2}{x^2}\right)\right),\end{aligned} \tag{5.4}$$

where $v = V/t_B$. The integral can be computed explicitly and the final result is

$$\begin{aligned}\frac{\alpha(v)}{t_B} &= \frac{2}{\pi}\left[2\left(1+\ln(v/4)\right)\arctan\left(v/4\right)\right. \\ &+\frac{1}{4}v\ln\left(v^2+16\right)-\frac{1}{2}v\ln(v) \\ &\left.-i\mathrm{Li}_2\left(-\frac{iv}{4}\right)+i\mathrm{Li}_2\left(\frac{iv}{4}\right)\right] \end{aligned} \tag{5.5}$$

where Li_2 is the the polylogarithm of index 2. This quantity *slowly* tends to a constant at large bias:

$$\frac{\alpha}{t_B}(v\to\infty) = 2. \tag{5.6}$$

And at low bias we have:

$$\frac{\pi}{t_B}\alpha(v\to 0) = \left(\frac{5}{288}-\frac{1}{48}\ln(v/4)\right)v^3+\mathcal{O}\left(v^5\right). \tag{5.7}$$

5.4 Entropy rate for arbitrary U

We estimate the steady entropy rate α, defined in Sec. 5.1, by fitting the long-time part of the entanglement entropy data $S_{vN}(t)$.[2] As for the current, we consider the rescaled entropy rate α/t_B as a function of the rescaled bias V/t_B. The results, plotted in Figs. 5.4 and 5.5, show that the data obtained for a given value U but for different values of J collapse quite well onto a single master curve. The values of t_B used to construct the Figs. 5.4 - 5.5 are the same as those used to analyze the scaling of the current. From this point of view, the quality of the collapse for the entropy rate is quite remarkable since there is *no* adjustable parameter: the scale $t_B = J^{\frac{2}{1+b(U)}}$ was extracted from the large bias behavior of current only, and for a single value of $J = 0.1$, see Fig 3.17. Note also that, to our knowledge, no exact result is known for the entropy rate when $U \neq 0$, even at the self-dual point, although full counting statistics and charge cumulants are known.

The free fermion result for the entropy rate (derived in Sec. 5.3) slowly converges to some finite constant, $\alpha/t_B \to 2$, at large rescaled bias. An important fact we learn from the Fig. 5.4 is that, in presence of interactions, α/t_B also saturates to some finite value at large V/t_B. This limiting value appears to be smaller than 2 when $U > 0$. From our data the large bias behavior of the entropy rate when $U < 0$ is not simple to guess. It may diverge as $V/t_B \to \infty$, or it may saturate to some value larger than 2.

The rescaled entanglement rate in UV limit is presented in Fig. 5.6. As it is mentioned above, most of numerics is done for a small value of hopping $0.1 \leq J \leq 0.5$, but for free fermionic case these values are not small enough to reach UV limit, this cause to some discrepancy. The entanglement rate slowly saturates in the large voltage V/t_B regime (black line of Fig 5.4), one needs to use $J \ll 0.1$ to reach deep UV, where $\alpha/t_B = 2$ for free fermionic point. It seems that perturbation in U may not allow to obtain entanglement rate near $U = 0$. Data abruptly decreases with

[2] Like for the current $I(t)$, the entropy $S_{vN}(t)$ often shows some oscillatory part, $\sim \cos(Vt/2 + \mathrm{cst})$ for small values of $J \approx 0.1$, and we include such a term in the fitting function in order to improve the precision on α.

increasing interaction strength and then slowly, almost linearly vanishes for large interactions.

For $U > 0$, while the current decreases to zero at large voltage Fig. 3.19, the entropy rate stays finite. This observation is somehow counter intuitive since a vanishingly small amount of charge is transfered per unit of time from one wire to the other, while their entanglement entropy still grows at a finite rate. In this large bias regime it is possible that the entanglement is generated by the density-density interaction U, without any actual transfer of particles from one lead to the other. This question certainly deserves some further investigations.

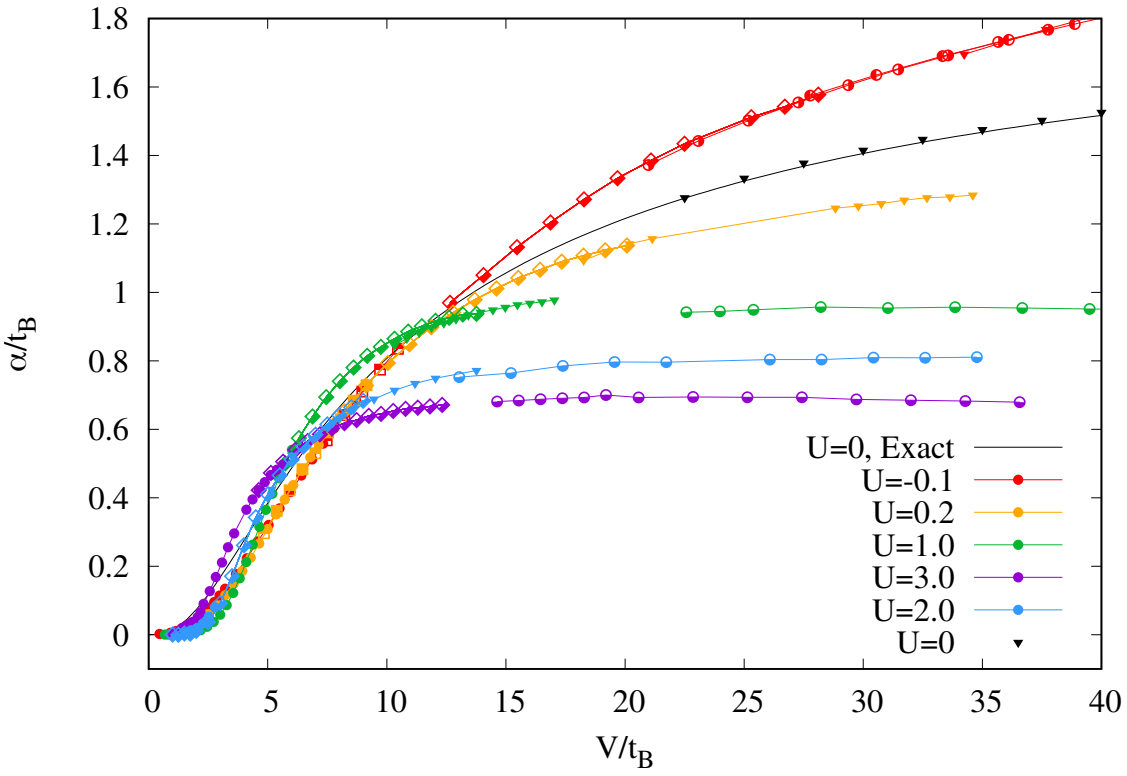

Figure 5.4: Rescaled entropy rate, α/t_B, as a function of rescaled bias V/t_B for several values of U. The colors label the values of U, while the symbol shapes encode J (see the legend of Fig. 3.20 for details). The black line is the exact free fermion result (Eq. 5.5).

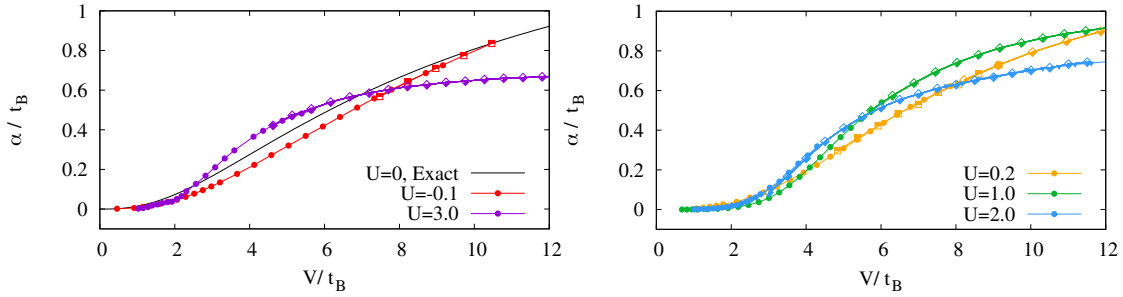

Figure 5.5: Same as Fig. 5.4, with a zoom on the low bias region. Left panel: $U = -0.1$, 0 and 3. Right panel: $U = 0.2$, 1 and 2. The colors encode the values of U, while the symbol shapes label the values of J, as indicated in the legend of Fig. 3.20. The black line (left panel) is the exact free fermion result in the limit $J \to 0$ (Eq. 5.5).

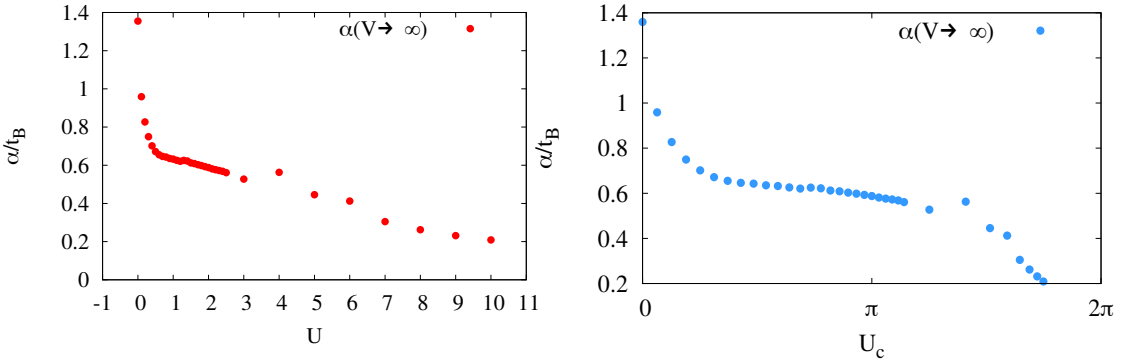

Figure 5.6: Rescated entanglement rate α/t_B in the limit $V/t_B \to \infty$ as a function of interaction strength on a lattice U(left panel) and continuum U_c(right panel). Entropy rate abruptly changes in the vicinity of free point $U = 0$, whereas near $U = U_{\rm sd}$ it is almost linear.

Chapter 6

Conclusion

The interacting resonant level model represents one of the simplest example of quantum impurity model. In spite of this apparent simplicity, the IRLM displays some rich behaviors, and pauses many questions which are still open. For instance, it is not known how to use the integrability of the model in equilibrium to construct the full out-of-equilibrium solution for arbitrary interaction strength U. In particular, exact analytical results for the charge transport characteristics in presence of a voltage bias, like the $I-V$ curves, are not known in general. At present only two exact solutions have been obtained, for values of the interaction strength U where the model possesses certain symmetries and can be mapped onto a cousin model – the boundary sine-Gordon model. Numerical methods have however shed light on the out-of-equilibrium Physics of this model.

In the present work, we have performed extensive state-of-the-art numerical simulations of the model dynamics with the time-dependent density renormalization group method (tDMRG), which is based on a matrix product state description of the wave functions. In particular, thanks to a 7-steps W^{II} approximation scheme, we could perform long and precise simulations in a wide range of parameters of the model, even though the problem is a priori quite challenging from tDMRG simulations since the entanglement entropy grows linearly with time in presence of particle current. From this point of view our data might be used to benchmark new approximations for quantum impurity models, or when developing numerical schemes which can deal with long-time evolution in interacting problems with linear entanglement entropy growth.

We have obtained and analyzed a large amount of data concerning the steady-state properties of the IRLM, in a wide range of voltage bias, interaction strength, tunneling amplitude to the dot, etc. We have obtained accurate results in the scaling limit for the current $I-V$ curves, and shot noise $S-V$ curves, for the exponent $b(U)$ and entanglement entropy rate α. We could explore all the regimes of the model, from the IR to the UV. Some particular focus has been put on extracting the emerging energy scale from the numerics, the Kondo temperature T_B, and on rescaling the current, noise and entropy data using this scale, to obtain universal curves. Indeed, for a given interaction U we could obtain some good data collapse onto a single master curve after rescaling the above transport characteristics by T_B(or t_B).

Surprisingly, the $I-V$ formulas for the BSG model turned out to provide excellent approximations to the steady current of the IRLM, after adjusting only two

parameters (exponent b and prefactor of the Kondo energy). Moreover, the $S-V$ curves of the BSG model also turned out to describe well the shot noise of the resonant model, especially for moderate values of the interaction strength ($U \lesssim 3$). The two models coincides exactly for two values of U ($U = 0$ and U_{sd}) and it is tempting to speculate that models could in fact be equivalent for arbitrary interaction U. However, a careful comparison of more subtle aspects, such as the backscattered current in low voltage V/T_B regime and the tunneling charge, showed that this cannot be the case. The remarkable agreement of their $I-V$ and $S-V$ curves in the crossover regime thus remains quite surprising.

Also quite surprising is the behavior of entropy rate in the UV. It would also be very interesting to elucidate, at least qualitatively, the mechanisms at work in the limit of large bias and $U > 0$, to understand how a finite entropy rate can coexist with a vanishingly small current. We hope that this study will trigger some further investigations using analytical techniques.

Appendix A

Matrix product state and DMRG

Strong correlation effects play a central role in many interesting and challenging areas of quantum many-body physics. The Hilbert space of quantum systems, like spin models, ultra-cold gases in optical lattices, high-temperature superconductors or frustrated magnets is huge and immense. Its dimension grows exponentially with system size. For a relatively small spin-1/2 system of size $N = 300$, the number of basis states already exceeds the number of atoms in the universe ($\sim 10^{82}$)! This strongly restricts direct numerical approaches, like exact diagonalization, to small systems. For spin systems, one can reach about 50-60 sites nowadays (see for instance [111]). It turns out that many interesting Physical states belong to some remarkable small class of wave-functions in which the entanglement entropy is relatively low, and follows a scaling property which is called the *area law* [112, 113, 114]. This is in particular the case for the ground-states and low-energy states of many Hamiltonians with short-ranged interactions. For one-dimensional systems this special part of Hilbert space can be parameterized efficiently by *matrix product states* (MPS).

A.1 Tensor representation of many-body wave-functions

To introduce the language of MPS, we consider a lattice system of N sites and its quantum many-body wave-function. Building blocks of this many-body wave-function are the states $|s_r\rangle$ of a single site at position r, where r runs from 1 to N and s_r labels a basis state of the local "s level system". As a simple example, we can choose a system of spin-1/2, with $|s =\uparrow,\downarrow\rangle$ up and down spins, or, equivalently, a system of spinless fermions, with $|s = 0, 1\rangle$, where 0 means an empty site and 1 refers to a site occupied by particle. For a system of N sites with 2 states at each site, the Hilbert space is exponentially large and its dimension is 2^N (or s^N in general).

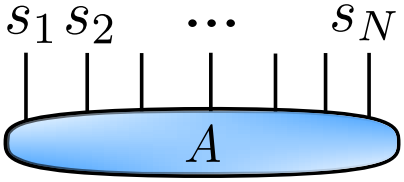

Figure A.1: Schematics of the many-body wave-function. A is a tensor of rank N. Indices s_r denote physical degrees of freedom, for instance $|s =\uparrow\rangle$ and $|s =\downarrow\rangle$.

Any wave-function for this system can be written

in terms of a sum of tensor products of the $|s_r\rangle$ as:

$$\begin{aligned} |\psi\rangle &= \sum_{s_1 s_2 \ldots s_N} A_{s_1 s_2 \ldots s_N} |s_1\rangle \otimes |s_2\rangle \otimes \cdots \otimes |s_N\rangle \\ &= \sum_{s_1 s_2 \ldots s_N} A_{s_1 s_2 \ldots s_N} |s_1 s_2 \ldots s_N\rangle \,. \end{aligned} \tag{A.1}$$

In the above equation, 2^N complex numbers $A_{i_1 i_2 \ldots i_N}$ define a state $|\psi\rangle$ and they can be interpreted as the tensor coefficients of the "N-leg" tensor A.

A.2 Breaking the wave-function into small pieces

A.2.1 Singular value decomposition

The widespread problem of manipulating and storing big volumes of information is ubiquitous in computer science and, in particular, in computational Physics. Many sophisticated methods have been developed for this kind of problems, from quantum Physics to image and sound processing. One of the most simple and efficient methods for information compressing is the so-called singular value decomposition (SVD), and it is at the root of the MPS construction. To sketch the main idea, let us consider a quantum system that is described by a state $|\psi\rangle$. The discussion below is based on Refs. [26, 115, 116].

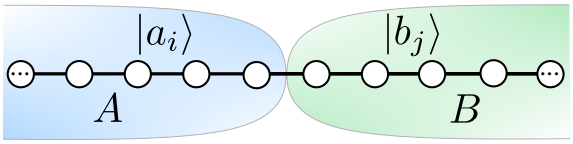

Figure A.2: One dimensional system as a union of two subsystems A and B.

Any pure state $|\psi\rangle$ on a system AB, for instance the system on Fig. A.2, can be written as

$$|\psi\rangle = \sum_{ij} M_{ij} |a_i\rangle \otimes |b_j\rangle \,, \tag{A.2}$$

were M_{ij} is a rectangular matrix of size $m \times n$, the states $|a_i\rangle$ and $|b_j\rangle$ form orthonormal bases of the Hilbert spaces of A and B, with dimension $m = \dim(\mathcal{H}_A)$ and $n = \dim(\mathcal{H}_B)$ respectively.

We carry out an SVD of matrix M. It can be rewritten [see Fig. A.3], in the following form

$$M = USV^\dagger. \tag{A.3}$$

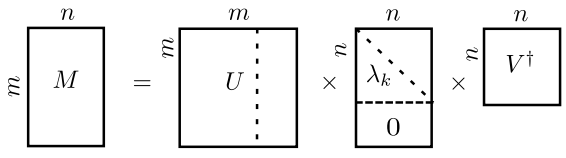

Figure A.3: Singular value decomposition of matrix M

The matrix U is of dimension $m \times m$ and it consists of orthonormal columns, so called *left singular vectors*, and therefore $U^\dagger U = I$. The matrix $V^\dagger$ is of size $n \times n$ and has orthonormal rows ($V^\dagger V = I$) called *right singular vectors*. The matrix S is diagonal with non-negative entries $\lambda_k \geq 0$. These are the so-called *singular values*, and in the following we assume that they are sorted in descending order, i.e. $\lambda_1 \geq \lambda_2 \geq \cdots \geq \lambda_n \geq 0$. Note that we have assumed here that $m \geq n$. For a typical distribution of λ_k, see Fig. A.4.

Now we write the *Schmidt* decomposition (c.f. e.g. Ref. [117, 118]) of the wave-function $|\psi\rangle$ using Eq.(A.3):

$$\begin{aligned}|\psi\rangle &= \sum_{ikj} U_{ik}\lambda_k \left(V^\dagger\right)_{kj} |a_i\rangle \otimes |b_j\rangle \\ &= \sum_k^n \lambda_k \left(\sum_i^m U_{ik} |a_i\rangle\right) \otimes \left(\sum_j^n V^*_{jk} |b_j\rangle\right) \\ &= \sum_{k=1}^n \lambda_k |u_k\rangle \otimes |v_k\rangle \,. \end{aligned} \tag{A.4}$$

The unitary transformations U and $V^\dagger$ preserve "orthonormality" in subsystems A and B, i.e. $\langle u_i|u_j\rangle = \delta_{ij} = \langle v_i|v_j\rangle$. It should be noted that a unitary evolution of the form $\mathcal{U} = e^{-it(H_A+H_B)}$ which acts independently in regions A and B does not change the Schmidt singular values, and the following decomposition is still a valid Schmidt decomposition:

$$e^{-it(H_A+H_B)} |\psi\rangle = \sum_{k=1}^n \lambda_k \left(\mathcal{U}_A |u_k\rangle\right) \otimes \left(\mathcal{U}_B |v_k\rangle\right) \tag{A.5}$$

The Schmidt decomposition is a useful way to write a quantum state in relation to some bi-partition A-B. First, it is convenient because one can read off the reduced density matrices ρ_A and ρ_B associated to the regions A and B:

$$\rho_A = \mathrm{Tr}_B |\psi\rangle \langle\psi| = \sum_{k=1}^n \lambda_k^2 |u_k\rangle \langle u_k| \tag{A.6}$$

$$\rho_B = \mathrm{Tr}_A |\psi\rangle \langle\psi| = \sum_{k=1}^n \lambda_k^2 |v_k\rangle \langle v_k| \,. \tag{A.7}$$

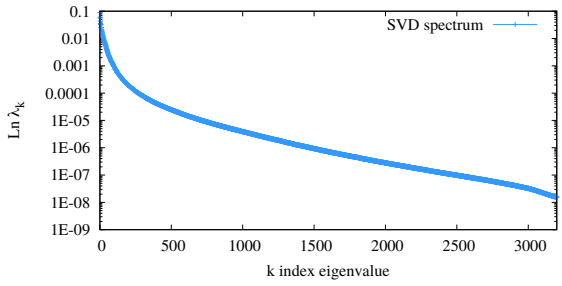

Figure A.4: A typical example of SVD spectrum from one of our simulations.

The eigenvalues of the reduced density matrices are thus simply related to the Schmidt singular values, and the von Neumann entanglement entropy can be obtained directly from the SVD:

$$S_A^{vN} = -\,\mathrm{Tr}\,\rho_A \ln \rho_A = -\sum_{k=1}^n \lambda_k^2 \ln \lambda_k^2. \tag{A.8}$$

This also shows that both reduced density matrices ρ_A and ρ_B have the same non-zero eigenvalues, and that the entanglement entropy is symmetric $S_A^{vN} = S_B^{vN} = -\,\mathrm{Tr}\,\rho_B \ln \rho_B$. Note however that the subsystems A and B do not necessarily have the same size.

The Schmidt decomposition also offers a way to approximate a state $|\psi\rangle$ by some $|\psi_r\rangle$ which would have an A-B Schmidt decomposition with at most r singular values. The latter would occupy a smaller memory space and could therefore ease

the numerical calculations. The Hilbert space 2-norm is equivalent to the Frobenius norm of the matrix M:

$$\|\psi\|_H^2 = \langle\psi|\psi\rangle = \sum_{ij} |M_{ij}|^2 = \mathrm{Tr}[MM^\dagger] = \|M\|_F^2 \,, \tag{A.9}$$

therefore the optimal approximation $|\psi_r\rangle$ is given by the optimal approximation M_r of the matrix M in Frobenius norm. The SVD of $M_r = US_rV^\dagger$ is constructed from the largest singular values of M, i.e. $S_r = \mathrm{diag}(\lambda_1, \ldots, \lambda_r, 0, \ldots, 0)$, where $r < n$. Usually, the truncation index r is chosen by the condition $\sum_{k>r} \lambda_k < \delta$, i.e. the discarded weight should not exceed δ, where the truncation parameter δ is chosen to be small enough. In our numerics we use $\delta = 10^{-7}$ or smaller, for more details see Chap. A.5. The new Schmidt decomposition of the approximated state is constructed with the first r high weighted states and reads

$$|\psi_r\rangle = \frac{1}{\mathcal{N}} \sum_{k=1}^{r} \lambda_k \, |u_k\rangle \otimes |v_k\rangle \,, \tag{A.10}$$

where $\mathcal{N} = \sqrt{\sum_{k=1}^{r} \lambda_k^2}$ restores normalization of the wave-function.

A.2.2 Matrix product state

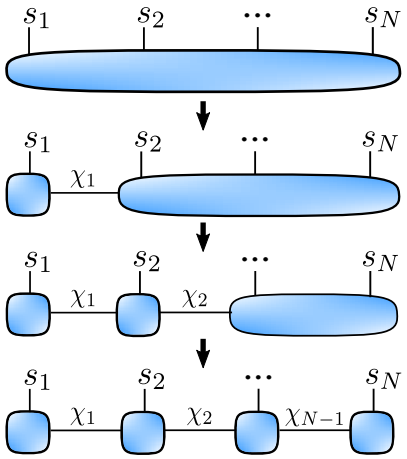

Figure A.5: Schematics for obtaining an MPS representation of a many-body wave-function in a one-dimensional system with open boundary conditions. The system consists of N lattice sites, s_r represent the Physical degrees of freedom, for instance $|s = \uparrow, \downarrow\rangle$.

The goal is to represent the many-body wave-function Eq. (A.1) of a system with N sites as an MPS, which is a one-dimensional tensor network, as depicted in Fig. A.5. We note that, in principle, MPS can be used to study d-dimensional systems (see for instance [119]), however this approach is mostly efficient in one-dimension.

Consider the many-body wave-function Eq. (A.1) of a system with N sites and a local two-dimensional space at each site r. We have a state vector with 2^N components $A_{s_1 s_2 \ldots s_N}$. To express the wave-function in terms of an MPS, we start from the left most site, and reshape the coefficient $A_{s_1 s_2 \ldots s_N}$ into a matrix M of dimension $2 \times 2^{N-1}$:

$$M_{s_1(s_2 \ldots s_N)} = A_{s_1 s_2 \ldots s_N} \tag{A.11}$$

Then we apply an SVD to the matrix M

$$\begin{aligned} A_{s_1 s_2 \ldots s_N} &= M_{s_1(s_2 \ldots s_N)} \\ &= \sum_{a_1}^{\chi_1} U_{s_1 a_1} S_{a_1 a_1} \left(V^\dagger\right)_{a_1(s_2 \ldots s_N)} \\ &\equiv \sum_{a_1}^{\chi_1} U_{s_1 a_1} R_{a_1 s_2 \ldots s_N} \,, \end{aligned} \tag{A.12}$$

where the rank of decomposition χ is called the *bond dimension* and for the first step $\chi_1 \leq 2$. The last equation is nothing but a

matrix multiplication $A = U \cdot R$. We now rewrite the matrix U as a collection of 2 row vectors M^{s_1} with entries $M^{s_1}_{a_1} = U_{s_1 a_1}$ and continue unweaving. Lets reshape $R_{a_1 s_2 \ldots s_N}$ into a matrix $M_{(a_1 s_2)(s_3 \ldots s_N)}$ of dimension $\chi_1 2 \times 2^{N-2}$ and apply an SVD one more time

$$\begin{aligned} A_{s_1 s_2 \ldots s_N} &= \sum_{a_1}^{\chi_1} \sum_{a_2}^{s_2} A^{s_1}_{a_1} U_{(a_1 s_2) a_2} S_{a_2 a_2} \left(V^\dagger\right)_{a_2 (s_3 \ldots s_N)} \\ &= \sum_{a_1}^{\chi_1} \sum_{a_2}^{s_2} A^{s_1}_{a_1} A^{s_2}_{a_1 a_2} M_{(a_2 s_3)(s_4 \ldots s_N)} \end{aligned} \tag{A.13}$$

where we have rewritten $U_{(a_1 s_2) a_2} = A^{s_2}_{a_1 a_2}$. We consistently continue to apply SVD site by site, from left to the right, until obtaining

$$A_{s_1 s_2 \ldots s_N} = \sum_{a_1 \ldots a_{N-1}} A^{s_1}_{a_1} A^{s_2}_{a_1 a_2} \ldots A^{s_{N-1}}_{a_{N-2} a_{N-1}} A^{s_N}_{a_{N-1}} \tag{A.14}$$

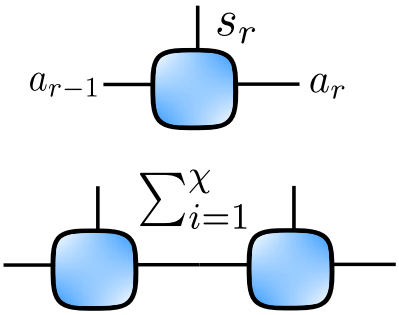

Figure A.6: An MPS building block A^{s_r} and contraction of blocks.

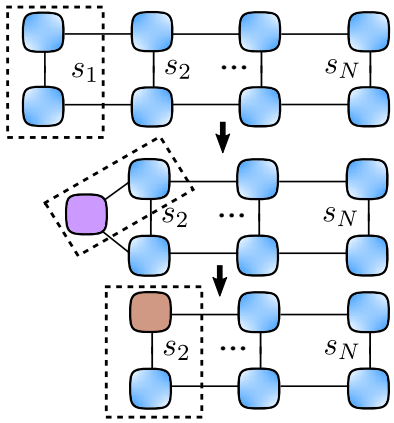

Figure A.7: Schematics of the overlap $\langle \phi | \psi \rangle$ for two states encoded as MPS.

A graphical representation helps to understand the unweaving procedure described above [see Fig. A.5]. Each matrix $A^{s_r}_{a_{r-1} a_r}$ (besides the first $A^{s_1}_{a_1}$ and the last $A^{s_N}_{a_N}$) is a 3-rank tensor. Graphically one presents it as a box with 3 legs [see Fig. A.6], they correspond to one physical index s_r and two auxiliary indices a_{r-1} and a_r. Connected legs denote tensor contraction with implicit summation.

Finally, we rewrite the amplitude $A_{s_1 s_2 \ldots s_N}$ as matrix multiplications, the *left-canonical* MPS reads [26, 120, 121]

$$A_{s_1 s_2 \ldots s_N} = A^{s_1} A^{s_2} \ldots A^{s_{N-1}} A^{s_N}. \tag{A.15}$$

Similarly, it is possible to present the wave-function in the *right-canonical* form

$$A_{s_1 s_2 \ldots s_N} = \tilde{A}^{s_1} \tilde{A}^{s_2} \ldots \tilde{A}^{s_{N-1}} \tilde{A}^{s_N}, \tag{A.16}$$

where the SVD procedure was initiated from the right most site N. We can also mix the left- and right- decompositions

$$A_{s_1 s_2 \ldots s_N} = A^{s_1} \ldots A^{s_r} S \tilde{A}^{s_{r+1}} \ldots \tilde{A}^{s_N}, \tag{A.17}$$

where S contains the Schmidt singular values (Eq. (A.4)) associated to a bi-partition across the bond $(r, r+1)$.

The MPS representation provides several important benefits:

- Any many-body quantum state can be represented exactly as an MPS. But doing so generically requires to use (exponentially) large matrices, and this would not offer any computational advantage. However it is often possible to *approximate* a given state by an MPS with tractable matrix dimensions.

- They can be searched efficiently. A family of variational algorithms (DMRG [22]) allows to find the lowest energy state among a given class of MPS.
- There is an entanglement hierarchy of MPS. Roughly speaking, states of one-dimensional systems with low entanglement entropy can be more efficiently approximated (using smaller matrices) than highly entangled states. What makes MPS useful in practice is the fact that low-energy states (and ground states in particular) of local one-dimensional Hamiltonians often exhibit an *area law* scaling [112, 114, 113] of the entanglement entropy, which makes them suitable for an MPS approximation.

A.3 Matrix product operators

A.3.1 Wave-function overlaps

To evaluate correlation functions and expectation values, one needs to understand how to express overlaps in terms of MPS. The overlap between two arbitrary states $|\phi\rangle$ and $|\psi\rangle$ has the following form

$$\begin{aligned}\langle\phi|\psi\rangle &= \sum_{s_1\dots s_N} \left(B^{s_1}B^{s_2}\dots B^{s_{N-1}}B^{s_N}\right)^\dagger A^{s_1}A^{s_2}\dots A^{s_{N-1}}A^{s_N} \\ &= \sum_{s_1\dots s_N} \left(B^{s_N\dagger}B^{s_{N-1}\dagger}\dots B^{s_2\dagger}B^{s_1\dagger}\right) A^{s_1}A^{s_2}\dots A^{s_{N-1}}A^{s_N} \\ &= \sum_{s_N} B^{s_N\dagger}\left(\dots\left(\sum_{s_2} B^{s_2\dagger}\left(\sum_{s_1} B^{s_1\dagger}A^{s_1}\right)A^{s_2}\right)\dots\right)A^{s_N} \end{aligned} \tag{A.18}$$

The nested sums look complicated, but a graphical representation of the MPS allows to understand the procedure [see Fig. A.7]. The bra- $\langle\phi|$ in a graphical notation has a similar form as ket-$|\psi\rangle$ in Fig.A.5, but corresponding physical indices $s_1\dots s_N$ are directed downwards. The contraction of $s_1\dots s_N$ is gradually carried out from the left to the right as one does with a *zipper* [see Fig. A.7].

In the section above we have unwoven $A_{s_1 s_2\dots s_N}$ up to the left-canonical form by successively applying SVD from the first site to the last, and have renamed respectively U to A^{s_r}. At each SVD step we have $U^\dagger U = I$, which means

$$\begin{aligned}\sum_{s_r}\left(A^{s_r\dagger}A^{s_r}\right)_{a_r a'_r} &= \sum_{s_r a_{r-1}}\left(A^{s_r\dagger}\right)_{a_r a_{r-1}} A^{s_r}_{a_{r-1}a'_r} \\ &= \sum_{s_r a_{r-1}} (U^\dagger)_{a_r(a_{r-1}s_r)} U_{(a_{r-1}s_r)a'_r} = \delta_{a_r a'_r}, \end{aligned} \tag{A.19}$$

or, more shortly,

$$\sum_{s_r} A^{s_r\dagger}A^{s_r} = I. \tag{A.20}$$

Similarly for the right-canonical representation

$$\sum_{s_r} \tilde{A}^{s_r} \tilde{A}^{s_r\dagger} = I. \tag{A.21}$$

The norm of the wave-function in a canonical MPS form obviously reads

$$\begin{aligned}
\langle\psi|\psi\rangle &= \sum_{s_1\dots s_N} \left(A^{s_1}A^{s_2}\dots A^{s_{N-1}}A^{s_N}\right)^\dagger A^{s_1}A^{s_2}\dots A^{s_{N-1}}A^{s_N} \\
&= \sum_{s_1\dots s_N} \left(A^{s_N\dagger}A^{s_{N-1}\dagger}\dots A^{s_2\dagger}A^{s_1\dagger}\right) A^{s_1}A^{s_2}\dots A^{s_{N-1}}A^{s_N} \\
&= \sum_{s_N} A^{s_N\dagger}\left(\dots\left(\sum_{s_2} A^{s_2\dagger}\left(\sum_{s_1} A^{s_1\dagger}A^{s_1}\right)A^{s_2}\right)\dots\right)A^{s_N} \\
= \sum_{s_N} A^{s_N\dagger}\left(\dots\left(\sum_{s_2} A^{s_2\dagger}A^{s_2}\right)\dots\right)A^{s_N} &= \dots = \sum_{s_N} A^{s_N\dagger}A^{s_N} = 1
\end{aligned} \tag{A.22}$$

A.3.2 Matrix product operators and expectation values

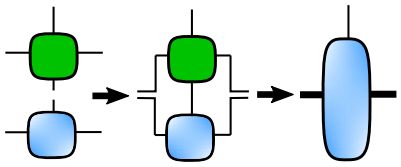

Figure A.8: Schematics of applying an MPO $\mathcal{O}_r$ to an MPS $|\psi\rangle$. The matrix dimension of the new MPO is the product of the dimensions appearing in $\mathcal{O}_r$ and $|\psi\rangle$.

By analogy to the representation of many-body quantum states using MPS, we can express every operator as a matrix-product operator (MPO)[122, 123, 124]. To do so, let us calculate the general expectation value of an observable. We consider $\langle\phi|\,\mathcal{O}_r\,|\psi\rangle$, where $\mathcal{O}_r$ is a local operator, which acts only on a site r. It can be the particle density operator $c_r^\dagger c_r$ for a fermionic system or the magnetization S_r^z for a spin-1/2 system. The matrix element of such an operator has a form

$$\mathcal{O}_r = \delta_{s_1 s_1'}\delta_{s_2 s_2'}\dots\left(\mathcal{O}^{s_r s_r'}\right)\dots\delta_{s_N s_N'} \tag{A.23}$$

and therefore

$$\mathcal{O}_r = \sum_{s_r s_r'} \mathcal{O}^{s_r s_r'}\,|s_r\rangle\,\langle s_r'| \tag{A.24}$$

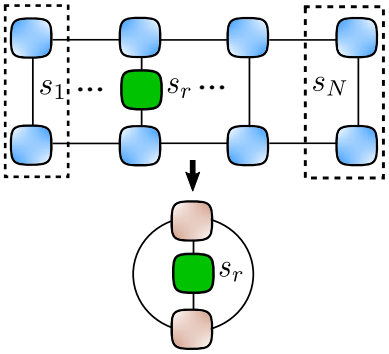

Figure A.9: Schematics of the overlap $\langle\psi|O_r|\psi\rangle$.

So, we introduce *matrix product operators* (MPO) (c.f. e.g Ref. [26]) as a straightforward generalization of the MPS notation as

$$\mathcal{O} = \sum_{\mathbf{ss'}} \mathcal{O}^{s_1 s_1'}\mathcal{O}^{s_2 s_2'}\dots\mathcal{O}^{s_N s_N'}\,|s_1\dots s_N\rangle\,\langle s_1'\dots s_N'|\,. \tag{A.25}$$

In the expression above each $\mathcal{O}^{ss'}$ is a matrix (indices not shown), and they are multiplied with each other. What happens if we apply an MPO $\mathcal{O}$ to an MPS $|\psi\rangle$? The MPS is formed by matrices of $A^{s_r'}$ and

MPO by matrices $\mathcal{O}^{s_r s'_r}$. The MPS reads

$$\begin{aligned}\mathcal{O}_r |\psi\rangle &= \sum_{s_r s'_r} \mathcal{O}^{s_r s'_r} |s_r\rangle \langle s'_r| \cdot \sum_{s''_r} A^{s''_r} |s''_r\rangle \\ &= \sum_{s_r s'_r} \mathcal{O}^{s_r s'_r} A^{s'_r} |s_r\rangle = \sum_{s_r} (\mathcal{O}A)^{s_r} |s_r\rangle \end{aligned} \tag{A.26}$$

Please, notice that the new matrix dimension of the MPS $(\mathcal{O}A)^{s_r}_{(ab)(a'b')} = \sum_{s'_r} \mathcal{O}^{s_r s'_r}_{aa'} A^{s'_r}_{bb'}$ is given by the product of the old matrix dimensions $ab \times a'b'$ [see Fig. A.8].

As the next step, we calculate an expectation value. For simplicity, we consider $\mathcal{O}_1$, which acts on the first site. The expectation value can be calculated as nested sums

$$\begin{aligned}\langle\phi|\mathcal{O}_1|\psi\rangle &= \sum_{s_1 \ldots s_N s'_1} (B^{s_1} B^{s_2} \ldots B^{s_{N-1}} B^{s_N})^\dagger \mathcal{O}^{s_1 s'_1} A^{s'_1} A^{s_2} \ldots A^{s_{N-1}} A^{s_N} \\ &= \sum_{s_N} B^{s_N \dagger} \left(\ldots \left(\sum_{s_2} B^{s_2 \dagger} \left(\sum_{s_1 s'_1} O^{s_1 s'_1} B^{s_1 \dagger} A^{s'_1} \right) A^{s_2} \right) \ldots \right) A^{s_N} \end{aligned} \tag{A.27}$$

Due to orthonormality of the matrix blocks Eq. (A.20), the expectation value of the operator $\mathcal{O}_r$ in a state $|\psi\rangle$ can be simply written as

$$\langle\psi|\mathcal{O}_1|\psi\rangle = \sum_{s_1 s'_1} \mathcal{O}^{s_1 s'_1} \operatorname{Tr}\left(A^{s_1 \dagger} A^{s'_1}\right) \tag{A.28}$$

The generalization of the above expression to $\langle\phi|\mathcal{O}|\psi\rangle$ is clear again, using the matrix elements $\mathcal{O}^{s_1 s'_1} \mathcal{O}^{s_2 s'_2} \ldots \mathcal{O}^{s_N s'_N}$ of Eq.(A.25). The expectation value reads

$$\begin{aligned}\langle\phi|\mathcal{O}|\psi\rangle &= \sum_{\mathbf{s}\mathbf{s}'} (B^{s_1} \ldots B^{s_N})^\dagger \mathcal{O}^{s_1 s'_1} \ldots \mathcal{O}^{s_N s'_N} A^{s'_1} \ldots A^{s'_N} \\ &= \sum_{s_N s'_N} O^{s_N s'_N} B^{s_N \dagger} \left(\ldots \left(\sum_{s_2 s'_2} O^{s_2 s'_2} B^{s_2 \dagger} \left(\sum_{s_1 s'_1} O^{s_1 s'_1} B^{s_1 \dagger} A^{s'_1} \right) A^{s'_2} \right) \ldots \right) A^{s'_N} \end{aligned} \tag{A.29}$$

A.4 Ground state and DMRG

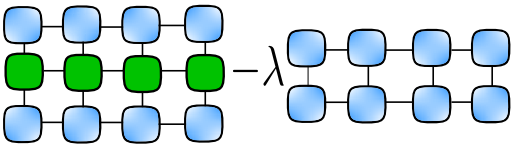

Figure A.10: Schematics of the variational problem $\min\left(\langle\psi|H|\psi\rangle - \lambda\langle\psi|\psi\rangle\right)$.

Independently of analytical properties and helpful pictorial representations, MPS are useful because they can be used as numerical ansatz for approximating interesting quantum many-body wave-functions, for instance the ground state of local Hamiltonians. How do we fill in the coefficients of the matrices A^{s_r} of an MPS? Lets explain the basic ideas behind one the most popular method to find ground states with MPS, namely the variational optimization, which is nothing but the famous Density Matrix Renormalization Group algorithm (DMRG) in the language of MPS [22, 23, 24].

One way to find a ground state is to solve a variational problem. We should look for the states $|\psi\rangle$ which minimize energy

$$E = \langle\psi|H|\psi\rangle, \tag{A.30}$$

and obey to normalization condition

$$\langle\psi|\psi\rangle = 1. \tag{A.31}$$

To find such states, we use the method of Lagrangian multipliers. The problem of minimizing Eq. (A.30) with the condition Eq. (A.31) can be reformulated as a minimization problem of the following functional

$$\mathcal{L} = \langle\psi|H|\psi\rangle - \lambda\left(\langle\psi|\psi\rangle - 1\right), \tag{A.32}$$

where λ is called the Lagrangian multiplier.

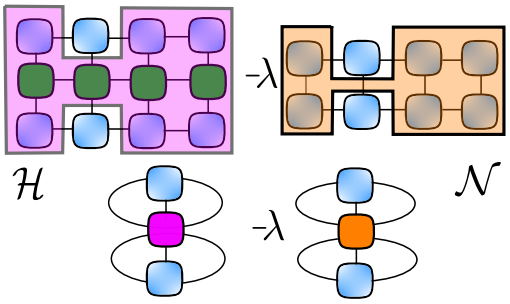

Figure A.11: Schematics of the variational problem $\min_A \left(A^\dagger \mathcal{H} A - \lambda A^\dagger \mathcal{N} A\right)$

The solution of the problem will be the ground state $|\psi\rangle$ and the desired ground state energy is λ.The MPS representation of the variational problem is shown in Fig. A.10.

Ideally, the above minimization should be done simultaneously over all the free parameters of the MPS, hence over all the elements for all sites. However, it is quite difficult to implement and not practically efficient. Instead of this, one can apply the following time-proven strategy [115]. We start with a guess for the MPS or, simply, generate a random MPS $A^{s_1}A^{s_2}\dots A^{s_{N-1}}A^{s_N}$. Then, imagine that we fix all the matrices in the MPS $A^{s_1}\dots A^{s_{r-1}}A^{s_{r-1}}\dots A^{s_N}$, except one of them which we call A^{s_r}. It could be for instance the first tensor A^{s_1}.

The coefficients of A^{s_r} are now our variational parameters, for brevity we write A without physical indices s_r. The optimization problem reads

$$\min_\psi \left(\langle\psi|H|\psi\rangle - \lambda\langle\psi|\psi\rangle\right) = \min_A \left(A^\dagger \mathcal{H}_{eff} A - \lambda A^\dagger \mathcal{N} A\right), \tag{A.33}$$

where $\mathcal{H}$ is an effective Hamiltonian and $\mathcal{N}$ is a normalization matrix [see Fig. A.11]. They encodes $\langle\psi|H|\psi\rangle$ and $\langle\psi|\psi\rangle$ but without $A^\dagger$ and A. If the MPS has open boundary conditions, it is always possible to choose an appropriate mixed canonical form for the tensors where $\mathcal{N} = I$, which is our case. The minimization problem reduces to

$$\frac{\partial}{\partial A^\dagger}\left(A^\dagger \mathcal{H}_{eff} A - \lambda A^\dagger A\right) = 0. \tag{A.34}$$

which leads to the eigenvalue problem

$$\mathcal{H}_{eff} A - \lambda A = 0, \tag{A.35}$$

Once $\mathcal{H}_{eff}$ (and $\mathcal{N}$) is known this generalized eigenvalue problem can be solved numerically by using standard linear algebra packages. Then, one should pick the next tensor A^{s_r}, repeat the optimization procedure described above until all tensors are optimized. In practice, in computer simulations one sweeps over all the tensors several times until the desired convergence in expectation values is attained [125]. We also mention that some DMRG algorithms optimize the matrices two by two (on pairs of neighboring sites).

A.5 Time evolution

The calculation of time-evolved states $|\psi(t)\rangle$ is of central interest in out-of-equilibrium quantum many-body problem. A direct exponentiation of the Hamiltonian H would lead to an MPO with huge bond dimension, and this cannot be used. A possible solution to this problem is the following. One tries to implement the finite-time evolution operator, like $U(t) = e^{-itH}$ (or $e^{\beta H}$), as a sequence of operators with *infinitesimally* small time steps δ [126, 127, 128], where $\sum \delta = t$. At each time step the evolution operator can be approximated by $U(\delta) \approx 1 - i\delta H$. Based on this basic Trotter idea, some recent advances [129] provided a new numerical algorithm to simulate the time evolution of an MPS in a very efficient way, which is noted as W^{II}. It has the advantage of being quite general. It can in particular deal with long-range interactions.

We consider a unitary time evolution operator

$$U(\tau) = e^{\tau H} = 1 + \tau H + \frac{\tau^2}{2!}\sum_{xy} H_x H_y + \frac{\tau}{3!}\sum_{xyz} H_x H_y H_z + ... \tag{A.36}$$

associated to the Hamiltonian $H = \sum_x H_x$. A construction of an approximation to U in an MPO form with small bond dimension, noted W^{II}, was proposed in Ref. [129]. Importantly, the error associated to this MPO approximation to evolution operator does not grow with the system size, which mean that it can be used on large systems. As explained in this previous work, one can combine several W^{II} to get a smaller error:

$$W^{\mathrm{II}}(\tau_1)W^{\mathrm{II}}(\tau_2)\cdots W^{\mathrm{II}}(\tau_n) = \exp(H\tau) + \mathcal{O}(\tau^p) \tag{A.37}$$

The simplest case is to use $n = 2$ steps to reduce the error to $\mathcal{O}(\tau^3)$. We expand Eq. (A.37) order by order

$$\begin{aligned} W^{\mathrm{II}}(\tau_1)W^{\mathrm{II}}(\tau_2) &= e^{\tau_1 H} e^{\tau_2 H} \\ &= \left(1 + \tau_1 H + \frac{\tau_1^2}{2!}A + \dots\right)\left(1 + \tau_2 H + \frac{\tau_2^2}{2!}A + \dots\right) \\ &= 1 + (\tau_1 + \tau_2)\, H + \tau_1\tau_2 H^2 + \frac{\tau_1^2 + \tau_2^2}{2!}A + \dots \end{aligned} \tag{A.38}$$

and find constraints

$$\tau_1 + \tau_2 = \tau, \quad \tau_1\tau_2 = \frac{1}{2!}\tau^2, \quad \frac{\tau_1^2 + \tau_2^2}{2!} = 0. \tag{A.39}$$

One solution is:

$$\begin{aligned} \tau_1 &= \frac{1+i}{2}\tau \\ \tau_2 &= \frac{1-i}{2}\tau. \end{aligned} \tag{A.40}$$

We have computed two other solutions, corresponding to $p = 4$ and $p = 5$. These were mentioned in Ref. [129], but not given explicitly. The first one requires $n = 4$

and is given by

$$\begin{aligned}
\tau_1 &= \frac{1}{4}\left(-\frac{1+i}{\sqrt{3}}+1-i\right)\tau \\
\tau_2 &= i\tau_1 \\
\tau_3 &= -i\bar{\tau}_1 \\
\tau_4 &= \bar{\tau}_1.
\end{aligned} \tag{A.41}$$

The next one, with an error scaling as $\mathcal{O}(\tau^{p=5})$ requires $n = 7$ steps. It was obtained numerically using Mathematica:

$$\begin{aligned}
\tau_1/\tau &= 0.2588533986109182 + 0.0447561340111419i \\
\tau_2/\tau &= -0.0315468581488038 + 0.2491190542755632i \\
\tau_3/\tau &= 0.1908290521106672 - 0.2318537492321061i \\
\tau_4/\tau &= 0.1637288148544367 \\
\tau_5 &= \bar{\tau}_3 \\
\tau_6 &= \bar{\tau}_2 \\
\tau_7 &= \bar{\tau}_1.
\end{aligned} \tag{A.42}$$

It should be noted that these solutions are not unique (~ 890 solutions), but we have selected the ones where the error terms, of the order $\mathcal{O}(\tau^p)$, have the smallest prefactors. We have checked the precision of these 3 different Trotter schemes on a small free-fermion system with 6 sites, and compared the results for the current at time $t = 100$ against the exact free-fermion solution. The results are shown in Fig. A.12. As expected, the total error scales as τ^{p-1}, due to the fact that the total number of steps is t/τ and each step contributes an amount of order $\mathcal{O}(\tau^p)$ to the error.

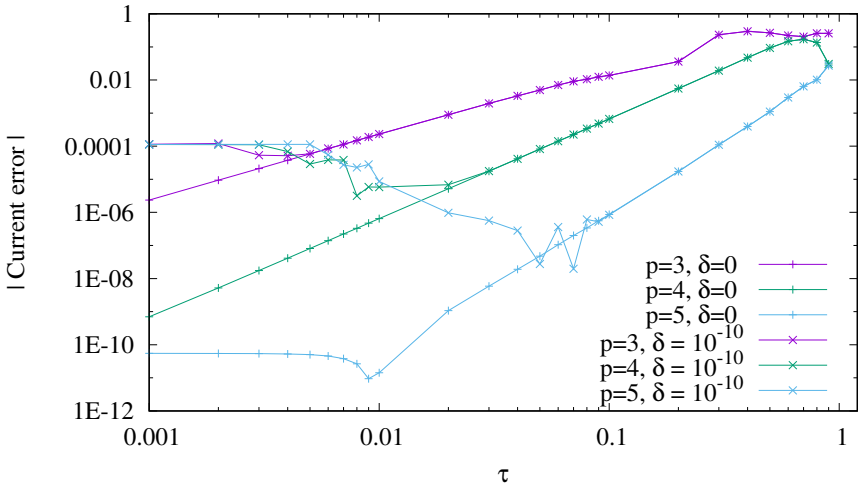

Figure A.12: Absolute value of the error for the expectation value of the current flowing through the quantum impurity at total time $t = 100$, for system $H = \frac{1}{2}\sum_1^6 c_{i+1}^\dagger c_i + H.c$, with initial particle bias $V = 1$ (for more details see Chapter 3). The error is computed by comparing the MPS simulations with an exact free-fermion calculation. For small τ the main source of error is no longer the finite τ, but the successive truncations in the Schmidt decompositions (SVD). This can be seen by comparing the data with cut-off parameter $\delta = 10^{-10}$ to those without any truncation ($\delta = 0$). When the error becomes extremely small, of the order of 10^{-10}, it stops decreasing with τ. This is due to the finite floating point precision of the machine.

Appendix B

Details about the numerical simulations

B.1 Parameters of simulations and matrix truncation

The simulations are performed using a tDMRG algorithm [130, 131] implemented using the C++ iTensor library [125]. We approximate the evolution operator by a matrix-product operator (MPO) [129] with a 4-th order [8] Trotter scheme. The largest time for our numerics is typically $t \simeq 40$ with time step $\tau = 0.2$, while the system size is $N = 257$ sites (128 sites in each lead).

The convergence of the data with respect to the maximum discarded weight δ and Trotter time step τ is illustrated in Fig. B.1. It appears that values between 0.1 and 0.2 for τ, and $\delta \sim 10^{-7}$ or below give good results in the time window we considered. As for the bottom panel also shows that an estimate of the steady value of the current can be obtained by fitting $I(t)$ to a constant plus exponentially decaying oscillations (at frequency $f = V/(4\pi)$ [132, 64]).

B.2 Scaling regime

We are interested in the scaling regime where, in principle, $J \ll \Gamma = 1$. However, if J becomes very small the time to reach a (quasi-) steady state becomes very large, which is difficult to handle in the simulations. In practice we use J from 0.1 up to 0.5 and $V \lesssim 1.6$ (to be compared with the bandwidth $W = 4$). A large range of V/T_B can then be scanned by varying V and J in the intervals above. To check that the model remains sufficiently close to the scaling regime, one verifies that rescaled quantities, like I/T_B, do not significantly depend on J once they are plotted as a function of the rescaled bias V/T_B. As a comparison, we mention that the functional RG method has the advantage of being able to work with very small values of J, and can therefore go *deeply* into the scaling limit of the lattice IRLM [86, 98]. But contrary to the present tDMRG calculations, the functional RG is controlled only when the interaction strength U is small.

But to be more precise we investigate below, at $U = 2$, the values of V and J beyond which deviations from the scaling regime become visible in the numerics. The Fig. B.2 shows the current computed for V up to 4, and fixed $J = 0.1$. The

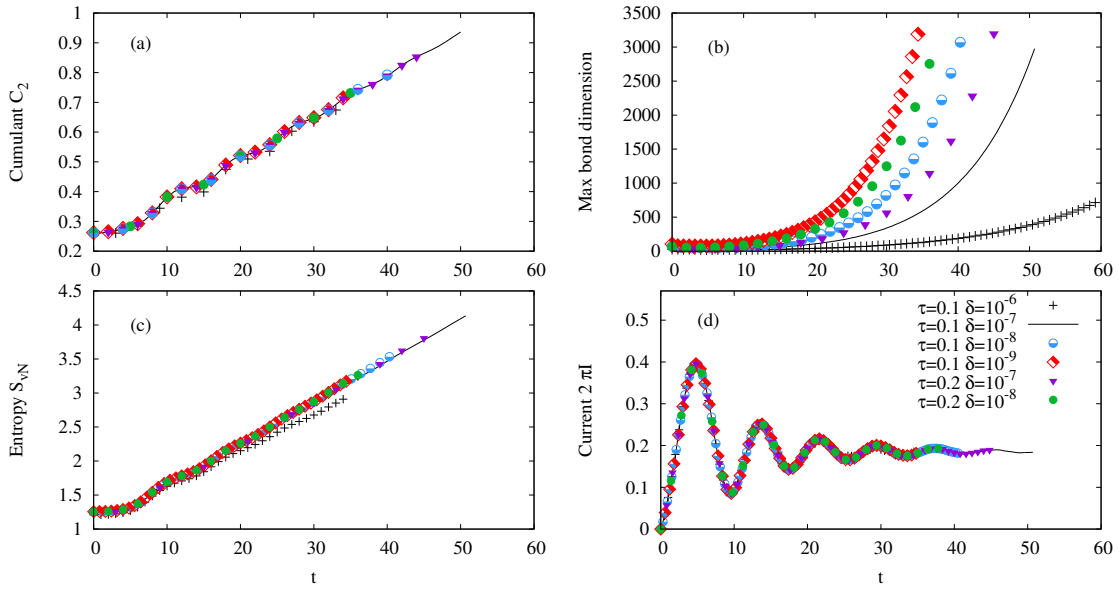

Figure B.1: Panel (a): second charge cumulant C_2 as a function of time and for different values of the Trotter step τ and truncation parameter δ (see bottom panel for the legend). Panel (b): MPS bond dimension M (link between the site $r = -1$ of the left lead and the dot at $r = 0$). In most calculations, the simulation is stopped when M reaches 4000. Panel (c): von Neumann entanglement entropy $S_{\rm vN}$ between the left and the right leads. Panel (d): Current $2\pi I$ as a function of t. Parameters of the model: $N = 257, U = 6(B), J = 0.3$ and $V = 1.6$. As far as the current or the entanglement entropy are concerned, all the simulations agree relatively well, apart from the less accurate one, with $\delta = 10^{-6}$ (crosses).

tDMRG result is compared with the exact result in the scaling regime (red curve). As expected, the agreement is very good at low bias, but it persists up to (almost) $V \sim 2$. Above this the lattice effects begin to affect the current. For this reason we typically work with V of the order of unity, avoiding too small values which would cause slow oscillations and difficulties to estimate the asymptotic steady values.

A similar analysis, shown Fig. B.2, can be done concerning J. Here again we compare the lattice calculations, at $U = 2$, with the exact continuum result. Both the steady current I and the backscattered current $I_{\rm BS} = V - 2\pi I$ are plotted in Fig. B.2. Looking at the current (upper panel), one may say that we have a good agreement for all the values of J, up to the largest one (here $J = 1$). But this is misleading: increasing J at fixed V makes the rescaled bias V/T_B smaller, and we thus go into the IR regime. In this regime of small rescaled bias and almost perfect transmission the current is essentially given by $I \simeq V/(2\pi)$, even in presence of strong lattice effects. So, to check that the nontrivial features of the continuum limit of the IRLM model are captured in the simulations, one should look at the deviations from $I \simeq V/(2\pi)$, that is one should analyze the backscattered current. This is represented in the bottom panel of Fig. B.2, and deviations from the scaling regime clearly appear only beyond $J \simeq 0.5$. This justifies the fact that in the present study we use J up to 0.4 or 0.5, while keeping very small the deviations from the scaling regime.

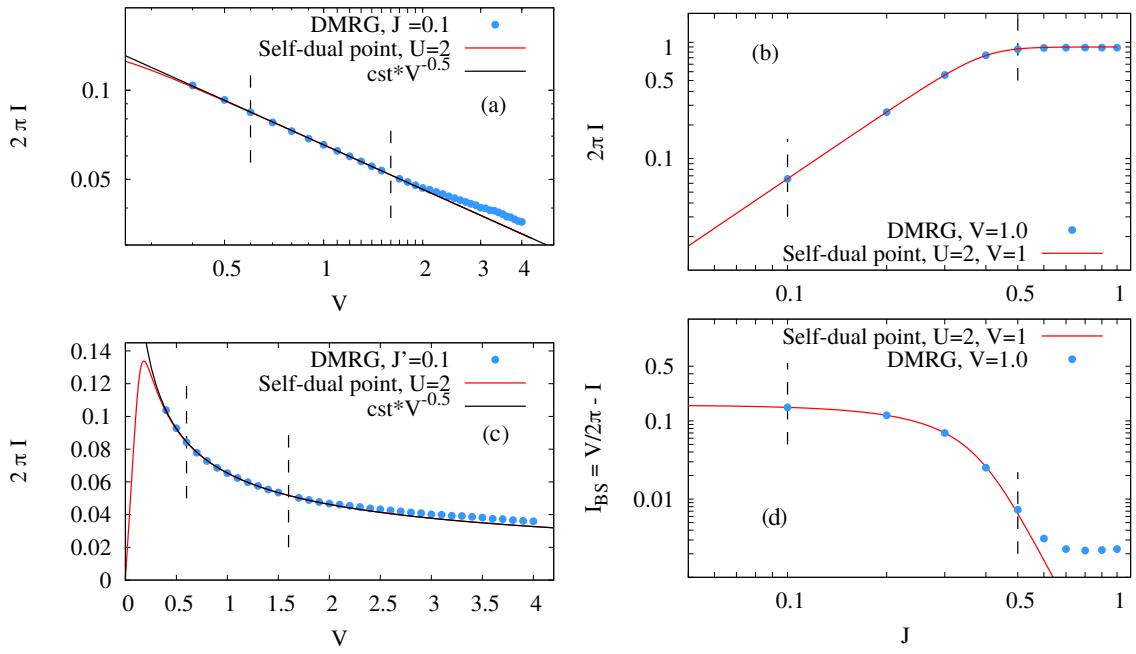

Figure B.2: Panel (a,c): Steady current I at $U = 2$ plotted as a function of the (bare) bias V. The blue dots are tDMRG results at $J = 0.1$ while the red line is the exact result in the continuum (scaling regime). Top (a): log scale showing that the current of the lattice model obeys the same power law behavior ($I \sim V^{-\frac{1}{2}}$) as the continuum limit up to $V \lesssim 2$. The vertical dashed lines indicate the bias range used in the present work. Bottom (b): same data in linear scale.
Panel (b): Steady current I at $U = 2$ plotted as a function of the hopping J and fixed $V = 1$ in a log scale. The vertical dashed lines indicate the range of J used in the present work. Panel (d): backscattered current $I_{\mathrm{BS}} = V/2\pi - I$ for the same parameters. The comparison with the exact result in the scaling regime (red curve) shows the lattice model is reasonably well described by the continuum limit up to $J \simeq 0.5$.

Appendix C

Comparison of the two protocols

As described in Sec. 2.2, two initial states are considered in this study. In the protocol (A) the initial state is constructed as the ground-state of a free fermion Hamiltonian with homogeneous hopping ($J_0 = \Gamma = 1$), and a chemical potential bias between the left and the right halves of the chain. As for protocol (B), the initial state is constructed as the ground-state of the IRLM Hamiltonian [Eq. (2.1), with $J_0 = J < \Gamma$ and $U_0 = U \neq 0$], to which the bias term [Eq. (2.9)] is added.

In the protocol (A) the initial state is built from an Hamiltonian which is spatially homogeneous, apart from the slowly varying H_{bias}. For this reason, it produces a relatively smooth spatial variation of the fermion density in the vicinity of the dot, by reducing possible Friedel-like oscillations. This also produces some smooth variation of the particle density in each lead as a function of the bias, minimizing discretization effects that are present if starting from disconnected (or almost disconnected) finite-size leads [1].

But since U is switched on at $t = 0$ in (A), the system has some excess energy of order $\mathcal{O}(U)$ that is localized in the vicinity of the dot at $t = 0^+$. This is simply because $\frac{1}{2}\langle S^z_{-1}S^z_0 + S^z_1 S^z_0\rangle$ is lower in the ground state of a model with $U > 0$ than in the ground state of a model with $U = 0$. Although this energy is expected to get gradually diluted across the system along the time evolution, we observe that for $U \gtrsim 3 - 4$ it can modify the observables in the vicinity of the dot [2]. This is illustrated in Fig. C.3, where the evolution of $E(t) = \frac{1}{2}\langle S^z_{-1}S^z_0 + S^z_1 S^z_0\rangle$ is displayed as a function of time in the protocols (A) and (B) and a few values of U from 1 to 6. For $U = 1$ or $U = 3$, after some transient regime $E(t)$ appears to have essentially the same limit in the two protocols. The value of the steady current is then also the same (Fig. C.3). But the situation is different for large values of U. For $U = 4$ the interaction energy in the protocol (A) takes a relatively long time to reach that of the protocol (B). In fact, at $t = 25$ the protocol (A) still shows some slight excess of interaction energy compared to the case (B). The situation is then quite dramatic for $U = 6$, since the up to $t = 24$ the interaction energy in (A) is much higher than that of (B), without any visible tendency to decay to a lower value. In such a situation it is not surprising that the transport through the dot is significantly different in (A) and (B), as can be seen in the bottom panel of Fig. C.3, where the protocol (A) cannot be used to estimate the steady current. Here we expect that much longer times would be needed before the interaction energy that is localized

[1] These discretization effects are present in the protocol (B) when J is small.

[2] We thank Peter Schmitterckert for pointing out this effect to us.

in the vicinity of the dot can "dissipate" in the leads in the form of kinetic energy.

Finally, we note that the protocol (B) also leads to a smaller entanglement entropy (see Fig. C.2), and for a given maximum bond dimension the simulations can be pushed to longer times. For these reasons, at large U, the protocol (B) where the U term is already present when constructing $|\psi(t=0)\rangle$ should be preferred. On the other hand, for $U=0$ and $U=2$, where exact results are available, the protocol (A) appears to give some slightly better results (see Fig. 4.1).

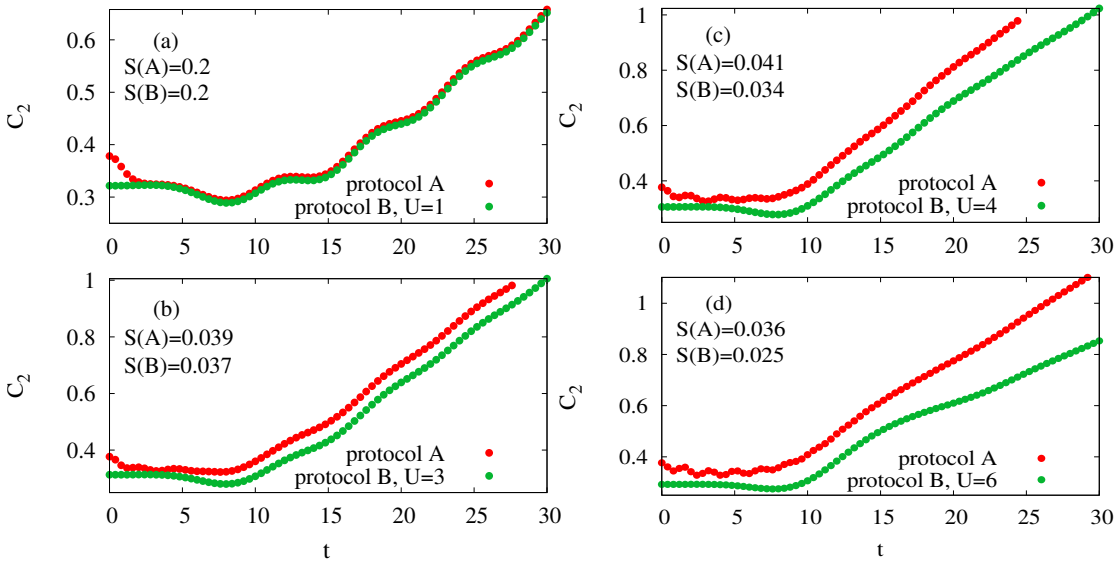

Figure C.1: Charge cumulant C_2 using the protocols (A) and (B). In each case, the estimate of the shot noise S is given in the legend. For $U \gtrsim 3$ the two protocols give markedly different results and in such cases the protocol (B) the most accurate one. Same parameters as in Fig. C.3.

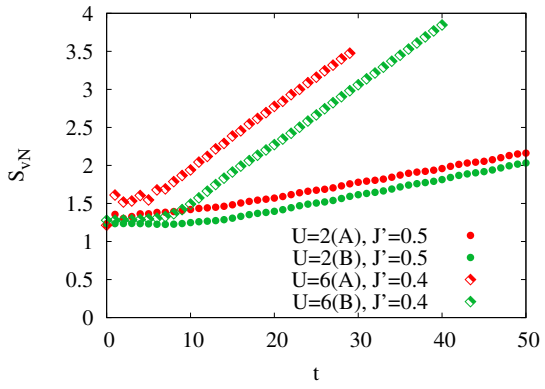

Figure C.2: Entanglement entropy S_{vN} as a function of time t for $U=2$ and $U=6$ with $V=1.0$. The entanglement entropy is lower with protocol (B) than with (A), especially when U is large. The estimate of the asymptotic entropy rate $\alpha = dS_{\mathrm{vN}}/dt$ [8] is relatively similar for the two protocols: $\alpha_A(U=6)=0.08$, $\alpha_B(U=6)=0.0788$, $\alpha_A(U=2)=0.0196$, $\alpha_B(U=2)=0.021$.

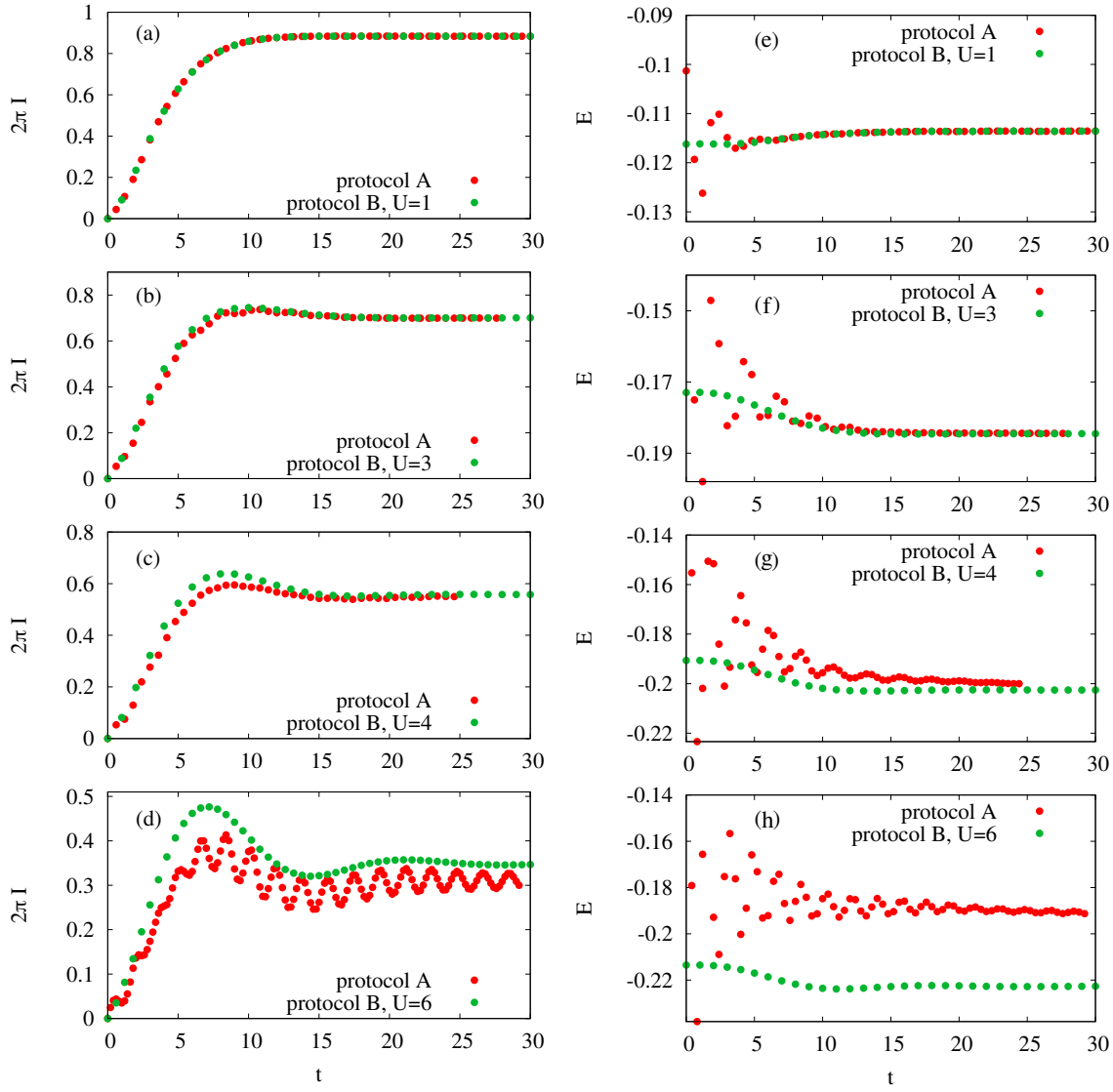

Figure C.3: Panels (a)-(d): Comparison of the current evolution using the protocols (A) and (B). Parameters of the model: $N = 257, J = 0.4$ and $V = 1$.
Panels (e)-(h): Comparison of the average interaction energy on the dot $E = 0.5\langle S^z_{-1}S^z_0 + S^z_1 S^z_0\rangle$ evolution using the protocols (A) and (B).

Bibliography

[1] P. B. Wiegmann and A. M. Finkel'shtein, *Resonant-level model in the kondo problem*, Sov. Phys. JETP **48**(1), 102 (1978).

[2] E. Boulat, H. Saleur and P. Schmitteckert, *Twofold Advance in the Theoretical Understanding of Far-From-Equilibrium Properties of Interacting Nanostructures*, Phys. Rev. Lett. **101**(14), 140601 (2008), doi:10.1103/PhysRevLett.101.140601.

[3] V. M. Filyov and P. B. Wiegmann, *A method for solving the Kondo problem*, Phys. Lett. A **76**(3), 283 (1980), doi:10.1016/0375-9601(80)90494-6.

[4] A. Branschädel, E. Boulat, H. Saleur and P. Schmitteckert, *Numerical evaluation of shot noise using real-time simulations*, Phys. Rev. B **82**(20), 205414 (2010), doi:10.1103/PhysRevB.82.205414.

[5] R. Landauer, *Spatial Variation of Currents and Fields Due to Localized Scatterers in Metallic Conduction*, IBM J. Res. Dev. **1**(3), 223 (1957), doi:10.1147/rd.13.0223.

[6] Y. Imry and R. Landauer, *Conductance viewed as transmission*, Rev. Mod. Phys. **71**(2), S306 (1999), doi:10.1103/RevModPhys.71.S306.

[7] Y. V. Nazarov and Y. Blanter, *Quantum transport - Introduction to Nanoscience*, Cambridge University Press (2009).

[8] K. Bidzhiev and G. Misguich, *Out-of-equilibrium dynamics in a quantum impurity model: Numerics for particle transport and entanglement entropy*, Phys. Rev. B **96**(19), 195117 (2017), doi:10.1103/PhysRevB.96.195117.

[9] L. Freton and E. Boulat, *Out-of-equilibrium properties and nonlinear effects for interacting quantum impurity systems in the strong-coupling regime*, Phys. Rev. Lett. **112**, 216802 (2014), doi:10.1103/PhysRevLett.112.216802.

[10] K. Bidzhiev, G. Misguich and H. Saleur, *Out-of-equilibrium transport in the interacting resonant level model: Surprising relevance of the boundary sine-Gordon model*, Phys. Rev. B **100**(7), 075157 (2019), doi:10.1103/PhysRevB.100.075157.

[11] J. A. Minahan and K. Zarembo, *The Bethe-ansatz for script N = 4 super Yang-Mills*, Journal of High Energy Physics **2003**(03), 013 (2003), doi:10.1088/1126-6708/2003/03/013.

[12] M. Franz and M. Rozali, *Mimicking black hole event horizons in atomic and solid-state systems*, Nature Reviews Materials **3**(12), 491 (2018), doi:10.1038/s41578-018-0058-z.

[13] B. Swingle, *Entanglement renormalization and holography*, Phys. Rev. D **86**, 065007 (2012), doi:10.1103/PhysRevD.86.065007.

[14] N. Bao, C. Cao, S. M. Carroll, A. Chatwin-Davies, N. Hunter-Jones, J. Pollack and G. N. Remmen, *Consistency conditions for an ads multiscale entanglement renormalization ansatz correspondence*, Phys. Rev. D **91**, 125036 (2015), doi:10.1103/PhysRevD.91.125036.

[15] M. Gaudin, *La fonction d'onde de Bethe*, MASSON (1983).

[16] V. E. Korepin, N. M. Bogoliubov and A. G. Izergin, *Quantum Inverse Scattering Method and Correlation Functions*, Cambridge Monographs on Mathematical Physics. Cambridge University Press, doi:10.1017/CBO9780511628832 (1993).

[17] K. G. Wilson, *The renormalization group: Critical phenomena and the kondo problem*, Rev. Mod. Phys. **47**, 773 (1975), doi:10.1103/RevModPhys.47.773.

[18] M. Salmhofer, *Renormalization in condensed matter: Fermionic systems – from mathematics to materials*, Nucl. Phys. B **941**, 868 (2019), doi:https://doi.org/10.1016/j.nuclphysb.2018.07.004.

[19] F. D. M. Haldane, *'luttinger liquid theory' of one-dimensional quantum fluids. i. properties of the luttinger model and their extension to the general 1d interacting spinless fermi gas*, Journal of Physics C: Solid State Physics **14**(19), 2585 (1981), doi:10.1088/0022-3719/14/19/010.

[20] J. von Delft and H. Schoeller, *Bosonization for beginners — refermionization for experts*, Annalen der Physik **7**(4), 225 (1998), doi:10.1002/(SICI)1521-3889(199811)7:4<225::AID-ANDP225>3.0.CO;2-L.

[21] D. Sénéchal, *An Introduction to Bosonization*, pp. 139–186, Springer New York, New York, NY, ISBN 978-0-387-21717-8, doi:10.1007/0-387-21717-7_4 (2004).

[22] S. R. White, *Density matrix formulation for quantum renormalization groups*, Phys. Rev. Lett. **69**, 2863 (1992), doi:10.1103/PhysRevLett.69.2863.

[23] S. R. White, *Density-matrix algorithms for quantum renormalization groups*, Phys. Rev. B **48**, 10345 (1993), doi:10.1103/PhysRevB.48.10345.

[24] U. Schollwöck, *The density-matrix renormalization group*, Rev. Mod. Phys. **77**, 259 (2005), doi:10.1103/RevModPhys.77.259.

[25] K. A. Hallberg, *New trends in density matrix renormalization*, Advances in Physics **55**(5-6), 477 (2006), doi:10.1080/00018730600766432, https://doi.org/10.1080/00018730600766432.

[26] U. Schollwöck, *The density-matrix renormalization group in the age of matrix product states*, Ann. Phys.ics **326**(1), 96 (2011), doi:10.1016/j.aop.2010.09.012.

[27] P. Di Francesco, P. Mathieu and D. Senechal, *Conformal Field Theory*, Graduate Texts in Contemporary Physics. Springer-Verlag, New York, ISBN 9780387947853, 9781461274759, doi:10.1007/978-1-4612-2256-9 (1997).

[28] J. Eisert, M. Friesdorf and C. Gogolin, *Quantum many-body systems out of equilibrium*, Nature Physics **11**(2), 124 (2015), doi:10.1038/nphys3215.

[29] A. Polkovnikov, K. Sengupta, A. Silva and M. Vengalatorre, *Colloquium: Nonequilibrium dynamics of closed interacting quantum systems*, Rev. Mod. Phys. **83**, 863 (2011), doi:10.1103/RevModPhys.83.863.

[30] P. Calabrese and J. Cardy, *Entanglement and correlation functions following a local quench: a conformal field theory approach*, J. Stat. Mech. **2007**(10), P10004 (2007), doi:10.1088/1742-5468/2007/10/P10004.

[31] M. Greiner, O. Mandel, T. W. Hänsch and I. Bloch, *Collapse and revival of the matter wave field of a bose-einstein condensate*, Nature **419**(6902), 51 (2002), doi:10.1038/nature00968.

[32] A. Polkovnikov, K. Sengupta, A. Silva and M. Vengalattore, *Colloquium : Nonequilibrium dynamics of closed interacting quantum systems*, Rev. Mod. Phys. **83**, 863 (2011), doi:10.1103/RevModPhys.83.863.

[33] P. Calabrese and J. Cardy, *Time dependence of correlation functions following a quantum quench*, Phys. Rev. Lett. **96**, 136801 (2006), doi:10.1103/PhysRevLett.96.136801.

[34] T. Giamarchi, *Quantum Physics in One Dimension*, Clarendon Press, ISBN 978-0-19-852500-4, doi:10.1093/acprof:oso/9780198525004.001.0001 (2004).

[35] G. Misguich, K. Mallick and P. L. Krapivsky, *Dynamics of the spin-1/2 heisenberg chain initialized in a domain-wall state*, Phys. Rev. B **96**, 195151 (2017), doi:10.1103/PhysRevB.96.195151.

[36] O. A. Castro-Alvaredo, B. Doyon and T. Yoshimura, *Emergent hydrodynamics in integrable quantum systems out of equilibrium*, Phys. Rev. X **6**, 041065 (2016), doi:10.1103/PhysRevX.6.041065.

[37] B. Bertini, M. Collura, J. De Nardis and M. Fagotti, *Transport in out-of-equilibrium xxz chains: Exact profiles of charges and currents*, Phys. Rev. Lett. **117**, 207201 (2016), doi:10.1103/PhysRevLett.117.207201.

[38] D. Goldhaber-Gordon, H. Shtrikman, D. Mahalu, D. Abusch-Magder, U. Meirav and M. A. Kastner, *Kondo effect in a single-electron transistor*, Nature **391**(6663), 156 (1998), doi:10.1038/34373.

[39] A. C. Hewson, *The Kondo Problem to Heavy Fermions*, Cambridge University Press (1993).

[40] L. Kouwenhoven and L. Glazman, *Revival of the Kondo effect*, Phys. World **14**(1), 33 (2001), doi:10.1088/2058-7058/14/1/28.

[41] P. W. Anderson and G. Yuval, *Exact results in the kondo problem: Equivalence to a classical one-dimensional coulomb gas*, Phys. Rev. Lett. **23**, 89 (1969), doi:10.1103/PhysRevLett.23.89.

[42] G. Yuval and P. W. Anderson, *Exact results for the kondo problem: One-body theory and extension to finite temperature*, Phys. Rev. B **1**, 1522 (1970), doi:10.1103/PhysRevB.1.1522.

[43] P. W. Anderson, G. Yuval and D. R. Hamann, *Exact results in the kondo problem. ii. scaling theory, qualitatively correct solution, and some new results on one-dimensional classical statistical models*, Phys. Rev. B **1**, 4464 (1970), doi:10.1103/PhysRevB.1.4464.

[44] K. Ohtaka and Y. Tanabe, *Theory of the soft-x-ray edge problem in simple metals: historical survey and recent developments*, Rev. Mod. Phys. **62**, 929 (1990), doi:10.1103/RevModPhys.62.929.

[45] P. Nozières and C. T. De Dominicis, *Singularities in the x-ray absorption and emission of metals. iii. one-body theory exact solution*, Phys. Rev. **178**, 1097 (1969), doi:10.1103/PhysRev.178.1097.

[46] A. B. Zamolodchikov, *Exact two-particle s-matrix of quantum sine-gordon solitons*, Communications in Mathematical Physics **55**(2), 183 (1977), doi:10.1007/bf01626520.

[47] S. Ghoshal and A. B. Zamolodchikov, *Boundary s matrix and boundary state in two-dimensional integrable quantum field theory*, Int. J. Mod. Phys. **A9**, 3841 (1994), doi:10.1142/S0217751X94001552, [Erratum: Int. J. Mod. Phys. **A9**,4353(1994)].

[48] H. Saleur, S. Skorik and N. Warner, *The boundary sine-gordon theory: Classical and semi-classical analysis*, Nucl. Phys. B **441**(3), 421 (1995), doi:https://doi.org/10.1016/0550-3213(95)00021-J.

[49] L. Borda, K. Vladár and A. Zawadowski, *Theory of a resonant level coupled to several conduction-electron channels in equilibrium and out of equilibrium*, Phys. Rev. B **75**, 125107 (2007), doi:10.1103/PhysRevB.75.125107.

[50] L. Borda, A. Schiller and A. Zawadowski, *Applicability of bosonization and the anderson-yuval methods at the strong-coupling limit of quantum impurity problems*, Phys. Rev. B **78**, 201301 (2008), doi:10.1103/PhysRevB.78.201301.

[51] I. V. Lerner, V. I. Yudson and I. V. Yurkevich, *Quantum wire hybridized with a single-level impurity*, Phys. Rev. Lett. **100**, 256805 (2008), doi:10.1103/PhysRevLett.100.256805.

[52] M. Goldstein, Y. Weiss and R. Berkovits, *Interacting resonant level coupled to a luttinger liquid: Universality of thermodynamic properties*, EPL (Europhysics Letters) **86**(6), 67012 (2009), doi:10.1209/0295-5075/86/67012.

[53] M. Goldstein, Y. Weiss and R. Berkovits, *Interacting resonant level coupled to a luttinger liquid: Population vs. density of states*, Physica E: Low-dimensional Systems and Nanostructures **42**(3), 610 (2010), doi:https://doi.org/10.1016/j.physe.2009.06.064, Proceedings of the international conference Frontiers of Quantum and Mesoscopic Thermodynamics FQMT '08.

[54] C. Rylands and N. Andrei, *Quantum dot at a luttinger liquid edge*, Phys. Rev. B **96**, 115424 (2017), doi:10.1103/PhysRevB.96.115424.

[55] V. Filyov and P. Wiegmann, *A method for solving the kondo problem*, Physics Letters A **76**(3), 283 (1980), doi:https://doi.org/10.1016/0375-9601(80)90494-6.

[56] P. Fendley, A. W. W. Ludwig and H. Saleur, *Exact nonequilibrium transport through point contacts in quantum wires and fractional quantum Hall devices*, Phys. Rev. B **52**(12), 8934 (1995), doi:10.1103/PhysRevB.52.8934.

[57] A. Branschädel, E. Boulat, H. Saleur and P. Schmitteckert, *Shot noise in the self-dual interacting resonant level model*, Phys. Rev. Lett. **105**, 146805 (2010), doi:10.1103/PhysRevLett.105.146805.

[58] S. T. Carr, D. A. Bagrets and P. Schmitteckert, *Full counting statistics in the self-dual interacting resonant level model*, Phys. Rev. Lett. **107**, 206801 (2011), doi:10.1103/PhysRevLett.107.206801.

[59] B. Doyon, *New method for studying steady states in quantum impurity problems: The interacting resonant level model*, Phys. Rev. Lett. **99**, 076806 (2007), doi:10.1103/PhysRevLett.99.076806.

[60] R. Bulla, T. A. Costi and T. Pruschke, *Numerical renormalization group method for quantum impurity systems*, Rev. Mod. Phys. **80**(2), 395 (2008), doi:10.1103/RevModPhys.80.395.

[61] F. B. Anders and A. Schiller, *Real-time dynamics in quantum-impurity systems: A time-dependent numerical renormalization-group approach*, Phys. Rev. Lett. **95**, 196801 (2005), doi:10.1103/PhysRevLett.95.196801.

[62] P. Schmitteckert, *Nonequilibrium electron transport using the density matrix renormalization group method*, Phys. Rev. B **70**(12), 121302 (2004), doi:10.1103/PhysRevB.70.121302.

[63] G. Schneider and P. Schmitteckert, *Conductance in strongly correlated 1d systems: Real-Time Dynamics in DMRG*, arXiv:cond-mat/0601389 (2006).

[64] A. Branschädel, G. Schneider and P. Schmitteckert, *Conductance of inhomogeneous systems: Real-time dynamics*, Ann. Phys. **522**(9), 657 (2010), doi:10.1002/andp.201000017.

[65] N. Laflorencie, *Quantum entanglement in condensed matter systems*, Phys. Rep. **646**, 1 (2016), doi:10.1016/j.physrep.2016.06.008.

[66] G. Toulouse, *Expression exacte de l'énergie de l'état de base de l'hamiltonien de Kondo pour une valeur particulière de Jz*, Comptes Rendus de l'Académie des sciences Paris **268**, page 1200 (1969), doi:https://gallica.bnf.fr/ark:/12148/bpt6k480289h/f1214.image.

[67] T. Antal, P. L. Krapivsky and A. Rákos, *Logarithmic current fluctuations in nonequilibrium quantum spin chains*, Phys. Rev. E **78**(6), 061115 (2008), doi:10.1103/PhysRevE.78.061115.

[68] J. Viti, J.-M. Stéphan, J. Dubail and M. Haque, *Inhomogeneous quenches in a free fermionic chain: Exact results*, EPL **115**(4), 40011 (2016), doi:10.1209/0295-5075/115/40011.

[69] T. Sabetta and G. Misguich, *Nonequilibrium steady states in the quantum XXZ spin chain*, Phys. Rev. B **88**(24), 245114 (2013), doi:10.1103/PhysRevB.88.245114.

[70] L. D. Landau and L. M. Lifshitz, *Quantum Mechanics Non-Relativistic Theory, Third Edition: Volume 3*, Butterworth-Heinemann, 3 edn., ISBN 0750635398 (1981).

[71] Y. M. Blanter and M. Büttiker, *Shot noise in mesoscopic conductors*, Physics Reports **336**(1), 1 (2000), doi:10.1016/S0370-1573(99)00123-4.

[72] A. O. Gogolin, A. A. Nersesian and A. M. Tsvelik, *Bosonization and strongly correlated systems* (2004).

[73] K. Schotte and U. Schotte, *Interpretation of kondo experiments in a magnetic field*, Physics Letters A **55**(1), 38 (1975), doi:https://doi.org/10.1016/0375-9601(75)90386-2.

[74] Y. Vinkler-Aviv, A. Schiller and F. B. Anders, *From thermal equilibrium to nonequilibrium quench dynamics: A conserving approximation for the interacting resonant level*, Phys. Rev. B **90**(15), 155110 (2014), doi:10.1103/PhysRevB.90.155110.

[75] V. V. Ponomarenko, *Resonant tunneling and low-energy impurity behavior in a resonant-level model*, Phys. Rev. B **48**, 5265 (1993), doi:10.1103/PhysRevB.48.5265.

[76] G. Camacho, *Exact results in the Interacting Resonant Level Model*, Ph.D. thesis, University of Kent, (2017).

[77] G. Zaránd, T. Costi, A. Jerez and N. Andrei, *Thermodynamics of the anisotropic two-channel kondo problem*, Phys. Rev. B **65**, 134416 (2002), doi:10.1103/PhysRevB.65.134416.

[78] G. Camacho, P. Schmitteckert and S. T. Carr, *Exact equilibrium results in the interacting resonant level model*, Phys. Rev. B **99**(8), 085122 (2019), doi:10.1103/PhysRevB.99.085122.

[79] E. Boulat and H. Saleur, *Exact low-temperature results for transport properties of the interacting resonant level model*, Phys. Rev. B **77**, 033409 (2008), doi:10.1103/PhysRevB.77.033409.

[80] P. Schlottmann, *The kondo problem. i. transformation of the model and its renormalization*, Phys. Rev. B **25**, 4815 (1982), doi:10.1103/PhysRevB.25.4815.

[81] D. M. Kennes, V. Meden and R. Vasseur, *Universal quench dynamics of interacting quantum impurity systems*, Phys. Rev. B **90**(11), 115101 (2014), doi:10.1103/PhysRevB.90.115101.

[82] R. Vasseur and H. Saleur, *Universal entanglement dynamics following a local quench*, SciPost Physics **3**(1), 001 (2017), doi:10.21468/SciPostPhys.3.1.001.

[83] A. Schiller and N. Andrei, *Strong-to-weak-coupling duality in the nonequilibrium interacting resonant-level model* (2007), arXiv:0710.0249.

[84] P. Fendley, A. W. W. Ludwig and H. Saleur, *Exact conductance through point contacts in the fractional quantum hall effect*, Phys. Rev. Lett. **74**(15), 3005 (1995), doi:10.1103/PhysRevLett.74.3005.

[85] P. Fendley and H. Saleur, *Hyperelliptic curves for multichannel quantum wires and the multichannel kondo problem*, Phys. Rev. B **60**, 11432 (1999), doi:10.1103/PhysRevB.60.11432.

[86] C. Karrasch, M. Pletyukhov, L. Borda and V. Meden, *Functional renormalization group study of the interacting resonant level model in and out of equilibrium*, Phys. Rev. B **81**(12), 125122 (2010), doi:10.1103/PhysRevB.81.125122.

[87] I. Affleck and A. W. W. Ludwig, *Universal noninteger "ground-state degeneracy" in critical quantum systems*, Phys. Rev. Lett. **67**, 161 (1991), doi:10.1103/PhysRevLett.67.161.

[88] P. Fendley, H. Saleur and N. Warner, *Exact solution of a massless scalar field with a relevant boundary interaction*, Nucl. Phys. B **430**(3), 577 (1994), doi:https://doi.org/10.1016/0550-3213(94)90160-0.

[89] L. S. Levitov, H. Lee and G. B. Lesovik, *Electron counting statistics and coherent states of electric current*, J. Math. Phys. **37**(10), 4845 (1996), doi:10.1063/1.531672.

[90] P. Fendley and H. Saleur, *Self-duality in quantum impurity problems*, Phys. Rev. Lett. **81**, 2518 (1998), doi:10.1103/PhysRevLett.81.2518.

[91] F. Schwarz, I. Weymann, J. von Delft and A. Weichselbaum, *Nonequilibrium steady-state transport in quantum impurity models: A thermofield and quantum quench approach using matrix product states*, Phys. Rev. Lett. **121**, 137702 (2018), doi:10.1103/PhysRevLett.121.137702.

[92] A. Kumar, L. Saminadayar, D. C. Glattli, Y. Jin and B. Etienne, *Experimental Test of the Quantum Shot Noise Reduction Theory*, Phys. Rev. Lett. **76**(15), 2778 (1996), doi:10.1103/PhysRevLett.76.2778.

[93] A. Branschädel, E. Boulat, H. Saleur and P. Schmitteckert, *Shot Noise in the Self-Dual Interacting Resonant Level Model*, Phys. Rev. Lett. **105**(14), 146805 (2010), doi:10.1103/PhysRevLett.105.146805.

[94] S. T. Carr, D. A. Bagrets and P. Schmitteckert, *Full Counting Statistics in the Self-Dual Interacting Resonant Level Model*, Phys. Rev. Lett. **107**(20), 206801 (2011), doi:10.1103/PhysRevLett.107.206801.

[95] S. T. Carr, P. Schmitteckert and H. Saleur, *Full counting statistics in the not-so-long-time limit*, Phys. Scr. **2015**(T165), 014009 (2015), doi:10.1088/0031-8949/2015/T165/014009.

[96] W. Metzner, M. Salmhofer, C. Honerkamp, V. Meden and K. Schönhammer, *Functional renormalization group approach to correlated fermion systems*, Rev. Mod. Phys. **84**(1), 299 (2012), doi:10.1103/RevModPhys.84.299.

[97] T. J. Suzuki, D. M. Kennes and V. Meden, *Current noise of the interacting resonant level model*, Phys. Rev. B **93**(8), 085306 (2016), doi:10.1103/PhysRevB.93.085306.

[98] D. M. Kennes, S. G. Jakobs, C. Karrasch and V. Meden, *Renormalization group approach to time-dependent transport through correlated quantum dots*, Phys. Rev. B **85**, 085113 (2012), doi:10.1103/PhysRevB.85.085113.

[99] D. M. Kennes and V. Meden, *Interacting resonant-level model in nonequilibrium: Finite-temperature effects*, Phys. Rev. B **87**, 075130 (2013), doi:10.1103/PhysRevB.87.075130.

[100] F. Lesage and H. Saleur, *Strong-coupling resistivity in the kondo model*, Phys. Rev. Lett. **82**, 4540 (1999), doi:10.1103/PhysRevLett.82.4540.

[101] F. Lesage and H. Saleur, *Perturbation of infra-red fixed points and duality in quantum impurity problems*, Nucl. Phys. B **546**(3), 585 (1999), doi:https://doi.org/10.1016/S0550-3213(99)00076-0.

[102] V. Eisler and I. Peschel, *On entanglement evolution across defects in critical chains*, EPL **99**(2), 20001 (2012), doi:10.1209/0295-5075/99/20001.

[103] J.-M. Stéphan and J. Dubail, *Local quantum quenches in critical one-dimensional systems: entanglement, the Loschmidt echo, and light-cone effects*, J. Stat. Mech. **2011**(08), P08019 (2011), doi:10.1088/1742-5468/2011/08/P08019.

[104] D. Gobert, C. Kollath, U. Schollwöck and G. Schütz, *Real-time dynamics in spin-1/2 chains with adaptive time-dependent density matrix renormalization group*, Phys. Rev. E **71**(3), 036102 (2005), doi:10.1103/PhysRevE.71.036102.

[105] V. Eisler and I. Peschel, *Surface and bulk entanglement in free-fermion chains*, J. Stat. Mech. **2014**(4), P04005 (2014), doi:10.1088/1742-5468/2014/04/P04005.

[106] J. Dubail, J.-M. Stéphan, J. Viti and P. Calabrese, *Conformal field theory for inhomogeneous one-dimensional quantum systems: the example of non-interacting Fermi gases*, SciPost Physics **2**(1), 002 (2017), doi:10.21468/SciPostPhys.2.1.002.

[107] I. Klich and L. Levitov, *Quantum Noise as an Entanglement Meter*, Phys. Rev. Lett. **102**(10), 100502 (2009), doi:10.1103/PhysRevLett.102.100502.

[108] H. F. Song, S. Rachel, C. Flindt, I. Klich, N. Laflorencie and K. Le Hur, *Bipartite fluctuations as a probe of many-body entanglement*, Phys. Rev. B **85**(3), 035409 (2012), doi:10.1103/PhysRevB.85.035409.

[109] H. F. Song, C. Flindt, S. Rachel, I. Klich and K. Le Hur, *Entanglement entropy from charge statistics: Exact relations for noninteracting many-body systems*, Phys. Rev. B **83**(16), 161408 (2011), doi:10.1103/PhysRevB.83.161408.

[110] L. Freton, E. Boulat and H. Saleur, *Infrared expansion of entanglement entropy in the interacting resonant level model*, Nucl. Phys. B **874**(1), 279 (2013), doi:10.1016/j.nuclphysb.2013.05.015.

[111] A. Wietek and A. M. Läuchli, *Sublattice coding algorithm and distributed memory parallelization for large-scale exact diagonalizations of quantum many-body systems*, Physical Review E **98**(3) (2018), doi:10.1103/physreve.98.033309.

[112] M. M. Wolf, F. Verstraete, M. B. Hastings and J. I. Cirac, *Area laws in quantum systems: Mutual information and correlations*, Phys. Rev. Lett. **100**(7), 070502 (2008), doi:10.1103/PhysRevLett.100.070502.

[113] M. B. Hastings, *An area law for one-dimensional quantum systems*, J. Stat. Mech. **2007**(08), P08024 (2007), doi:10.1088/1742-5468/2007/08/P08024.

[114] J. Eisert, M. Cramer and M. B. Plenio, *Colloquium: Area laws for the entanglement entropy*, Rev. Mod. Phys. **82**(1), 277 (2010), doi:10.1103/RevModPhys.82.277.

[115] R. Orús, *A practical introduction to tensor networks: Matrix product states and projected entangled pair states*, Annals of Physics **349**, 117 (2014), doi:https://doi.org/10.1016/j.aop.2014.06.013.

[116] S. Paeckel, T. Köhler, A. Swoboda, S. R. Manmana, U. Schollwöck and C. Hubig, *Time-evolution methods for matrix-product states* (2019), arXiv:1901.05824.

[117] A. Ekert and P. L. Knight, *Entangled quantum systems and the schmidt decomposition*, American Journal of Physics **63**(5), 415 (1995), doi:10.1119/1.17904.

[118] S. Sciara, R. Lo Franco and G. Compagno, *Universality of schmidt decomposition and particle identity*, Scientific Reports **7**, 44675 EP (2017), Article.

[119] E. Stoudenmire and S. R. White, *Studying two-dimensional systems with the density matrix renormalization group*, Annu. Rev. Condens. Matter Phys. **3**(1), 111 (2012), doi:10.1146/annurev-conmatphys-020911-125018.

[120] G. Vidal, *Classical simulation of infinite-size quantum lattice systems in one spatial dimension*, Physical Review Letters **98**(7) (2007), doi:10.1103/physrevlett.98.070201.

[121] R. Orús and G. Vidal, *Infinite time-evolving block decimation algorithm beyond unitary evolution*, Physical Review B **78**(15) (2008), doi:10.1103/physrevb.78.155117.

[122] G. K.-L. Chan, A. Keselman, N. Nakatani, Z. Li and S. R. White, *Matrix product operators, matrix product states, and ab initio density matrix renormalization group algorithms*, The Journal of Chemical Physics **145**(1), 014102 (2016), doi:10.1063/1.4955108.

[123] C. Hubig, I. P. McCulloch and U. Schollwöck, *Generic construction of efficient matrix product operators*, Physical Review B **95**(3) (2017), doi:10.1103/physrevb.95.035129.

[124] S. Paeckel, T. Köhler and S. R. Manmana, *Automated construction of U(1)-invariant matrix-product operators from graph representations*, SciPost Physics **3**(5) (2017), doi:10.21468/scipostphys.3.5.035.

[125] ITensor Library, http://itensor.org (version 2.0).

[126] G. Vidal, *Efficient simulation of one-dimensional quantum many-body systems*, Physical Review Letters **93**(4) (2004), doi:10.1103/physrevlett.93.040502.

[127] M. Zwolak and G. Vidal, *Mixed-state dynamics in one-dimensional quantum lattice systems: A time-dependent superoperator renormalization algorithm*, Physical Review Letters **93**(20) (2004), doi:10.1103/physrevlett.93.207205.

[128] F. Verstraete, J. J. García-Ripoll and J. I. Cirac, *Matrix product density operators: Simulation of finite-temperature and dissipative systems*, Physical Review Letters **93**(20) (2004), doi:10.1103/physrevlett.93.207204.

[129] M. P. Zaletel, R. S. K. Mong, C. Karrasch, J. E. Moore and F. Pollmann, *Time-evolving a matrix product state with long-ranged interactions*, Phys. Rev. B **91**(16), 165112 (2015), doi:10.1103/PhysRevB.91.165112.

[130] S. R. White and A. E. Feiguin, *Real-Time Evolution Using the Density Matrix Renormalization Group*, Phys. Rev. Lett. **93**(7), 076401 (2004), doi:10.1103/PhysRevLett.93.076401.

[131] A. J. Daley, C. Kollath, U. Schollwöck and G. Vidal, *Time-dependent density-matrix renormalization-group using adaptive effective Hilbert spaces*, J. Stat. Mech. **2004**(04), P04005 (2004), doi:10.1088/1742-5468/2004/04/P04005.

[132] N. S. Wingreen, A.-P. Jauho and Y. Meir, *Time-dependent transport through a mesoscopic structure*, Phys. Rev. B **48**(11), 8487 (1993), doi:10.1103/PhysRevB.48.8487.

université PARIS-SACLAY
ÉCOLE DOCTORALE
Physique en île-de-France (EDPIF)

Titre : Dynamique hors d'équilibre dans un modèle d'impureté quantique

Mots clés : Théorie de la matière condensée, problèmes à N corps quantiques, modèles de spins sur réseau, physique hors d'équilibre, impuretés quantiques, simulations numériques

Résumé : Le domaine des problèmes quantiques à N-corps à l'équilibre et hors d'équilibre sont des sujets majeurs de la Physique et de la Physique de la matière condensée en particulier.
Les propriétés d'équilibre de nombreux systèmes unidimensionnels en interaction sont bien comprises d'un point de vue théorique, des chaînes de spins aux théories quantiques des champs dans le continue. Ces progrès ont été rendus possibles par le développement de nombreuses techniques puissantes, comme, par exemple, l'ansatz de Bethe, le groupe de renormalisation, la bosonisation, les états produits de matrices ou la théorie des champs invariante conforme.
Même si les propriétés à l'équilibre de nombreux modèles soient connues, ceci n'est en général pas suffisant pour décrire leurs comportements hors d'équilibre, et ces derniers restent moins explorés et beaucoup moins bien compris.
Les modèles d'impuretés quantiques représentent certains des modèles à N-corps les plus simples. Mais malgré leur apparente simplicité ils peuvent capturer plusieurs phénomènes expérimentaux importants, de l'effet Kondo dans les métaux aux propriétés de transports dans les nanostructures, comme les points quantiques.
Dans ce travail nous considérons un modèle d'impureté appelé "modèle de niveau résonnant en interaction" (IRLM). Ce modèle décrit des fermions sans spin se propageant dans deux fils semi-infinis qui sont couplés à un niveau résonant – appelé point ou impureté quantique – via un terme de saut et une répulsion Coulombienne.
Nous nous intéressons aux situations hors d'équilibre où un courant de particules s'écoule à travers le point quantique, et étudions les propriétés de transport telles que le courant stationnaire (en fonction du voltage), la conductance différentielle, le courant réfléchi, le bruit du courant ou encore l'entropie d'intrication. Nous réalisons des simulations numériques de la dynamique du modèle avec la méthode du groupe de renormalisation de la matrice densité dépendent du temps (tDMRG), qui est basée sur une description des fonctions d'onde en terme d'états produits de matrices. Nous obtenons des résultats de grande précision concernant les courbes courant-voltage ou bruit-voltage de l'IRLM, dans un grand domaine de paramètres du modèle (voltage, force de l'interaction, amplitude de saut vers le dot, etc.).
Ces résultats numériques sont analysés à la lumière de résultats exacts de théorie des champs hors d'équilibre qui ont été obtenus pour un modèle similaire à l'IRLM, le modèle de Sine-Gordon avec bord (BSG). Cette analyse est en particulier basée sur l'identification d'une échelle d'énergie Kondo et d'exposants décrivant les régimes de petit et grand voltage. Aux deux points particuliers où les modèles sont connus comme étant équivalents, nos résultats sont en accord parfait avec la solution exacte. En dehors de ces deux points particuliers nous trouvons que les courbes de transport de l'IRLM et du modèle BSG demeurent très proches, ce qui était inattendu et qui reste dans une certaine mesure inexpliqué.

Title : Out-of-equilibrium dynamics in a quantum impurity model

Keywords : Condensed matter theory, quantum many-body problems, lattice spin models, out-of-equilibrium physics, quantum impurities, numerical simulations

Abstract : The fields of in- and out-of-equilibrium quantum many-body systems are major topics in Physics, and in condensed-matter Physics in particular.
The equilibrium properties of one-dimensional problems are well studied and understood theoretically for a vast amount of interacting models, from lattice spin chains to quantum fields in a continuum. These progresses were allowed by the development diverse powerful techniques, for instance, Bethe ansatz, renormalization group, bosonization, matrix product states and conformal field theory.
Although the equilibrium characteristics of many models are known, this is in general not enough to describe their non-equilibrium behaviors, the latter often remain less explored and much less understood.
Quantum impurity models represent some of the simplest many-body problems. But despite their apparent simplicity, they can capture several important experimental phenomena, from the Kondo effect in metals to transport in nanostructures such as point contacts or quantum dots.
In this thesis consider a classic impurity model - the interacting resonant level model (IRLM). The model describes spinless fermions in two semi-infinite leads that are coupled to a resonant level – called quantum dot or impurity – via weak tunneling and Coulomb repulsion.
We are interested in out-of-equilibrium situations where some particle current flows trough the dot, and study transport characteristics like steady current (versus voltage), differential conductance, backscattered current, current noise or the entanglement entropy. We perform extensive state-of-the-art computer simulations of model dynamics with the time-dependent density renormalization group method (tDMRG) which is based on a matrix product state description of the wave functions. We obtain highly accurate results concerning the current-voltage and noise-voltage curves of the IRLM in a wide range parameter of the model (voltage bias, interaction strength, tunneling amplitude to the dot, etc.).
These numerical results are analyzed in the light of some exact out-of-equilibrium field-theory results that have been obtained for a model similar to the IRLM, the boundary sine-Gordon model (BSG). This analysis is in particular based on identifying an emerging Kondo energy scale and relevant exponents describing the high- and low- voltage regimes. At the two specific points where the models are known to be equivalent our results agree perfectly with the exact solution. Away from these two points we find that, within the precision of our simulations, the transport curves of the IRLM and BSG remain very similar, which was not expected and which remains somewhat unexplained.

Université Paris-Saclay
Espace Technologique / Immeuble Discovery
Route de l'Orme aux Merisiers RD 128 / 91190 Saint-Aubin, France